SLAC-R-496
UC-414

STUDIES OF MULTIPARTICLE PRODUCTION IN HADRONIC Z^0 DECAYS*

Jingchen Zhou

Stanford Linear Accelerator Center
Stanford University
Stanford, CA 94309

December 1996

Prepared for the Department of Energy
under contract number DE-AC03-76SF00515

Printed in the United States of America. Available from the National Technical Information Service, U.S. Department of Commerce, 5285 Port Royal Road, Springfield, VA 22161.

*Ph.D. thesis, University of Oregon

To my grandparents Zhou Bisheng and Chen Dezhen

Abstract

Hadronic decays of Z^0 bosons produced in e^+e^- annihilation are ideal for testing QCD. This thesis presents a measurement of the charged-particle multiplicity distribution and the first experimental study of the ratio of cumulant to factorial moments, using hadronic Z^0 decays collected by the SLD experiment at SLAC. We find that this ratio, as a function of the moment-rank q, decreases sharply to a negative minimum at $q = 5$, which is followed by quasi-oscillations. These features are in qualitative agreement with expectations from higher-order perturbative QCD. We also present an analysis of the intermittency in rapidity phase space using the method of scaled factorial moments. We find that both parton cascade and hard-gluon radiations contribute to the growth of the moments by studying the event-shape and jet-topology dependencies. All aspects of the data appear to be reproduced reasonably well by the QCD-based Monte Carlo model.

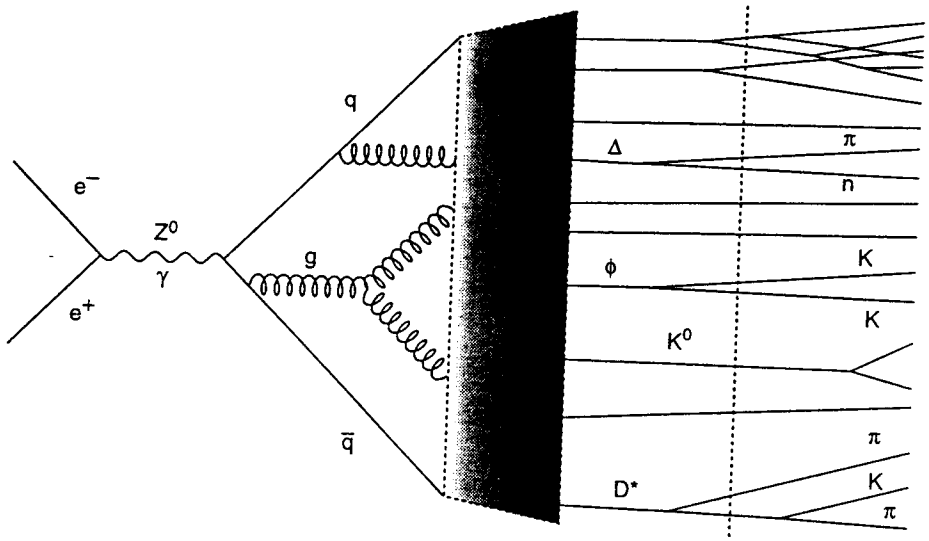
e⁻
e⁺
Z⁰
γ
q
g
q̄
Δ
π
n
φ
K
K
K⁰
π
D*
K
π

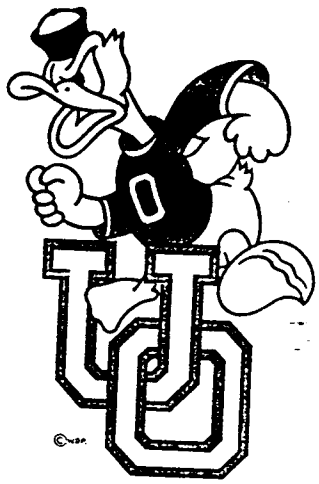

Acknowledgments

Behind this thesis are the contributions from many people I have had the fortune of working with. I own a deep debt of gratitude to each one.

Foremost, I would like to thank my advisor, Ray Frey, for his confidence six years ago in a foreign student, and his constant support and patience ever since. I have been very fortunate to be his student. His wisdom and faith has largely shaped my philosophy of life beyond physics, which I will benefit for ever.

I own much gratitude to Jim Brau for his encouragement and kindness toward me over the years. I am proud to be part of the UO HEP group headed by Jim, where I have spent the most pleasant and valuable years in my life. I would also like to thank David Strom for his help from time to time. Matt Langston has been an ideal officemate for the many years I have spent at SLAC as a student. His insistence on excellence and willingness to help has been becoming a model with which I will follow. It has been a sincere pleasure to work with and learn from Hwanbae Park, Kevin Pitts, Jenny Huber, Nikolai Sinev, Anatoli Arodzero, Xiaoqing Yang, David Mason and Hyun Hwang.

All members in SLD have been excellent contributers to my development as a physicist. Special thanks go to Phil Burrows and Dave Muller who have been leading QCD crews to many glories. It is their inspiration and guidance that kept us in the right track toward accomplishment. I have benefited from and enjoyed a wonderful team work with Hiro Masuda, Ken Bird, Tom Pavel, Gary Bower, Eric Church, Homer Neal, Tom Junk, Mike Hildreth, Takashi Maruyama and Takashi Akagi, who are always on standby and ready to give me hand. In particular, I want to thanks David Jackson, Ken Bird, Erez Etzion, Paul Dervan and Dave Muller who took their time to read and comment on my thesis. Significant contributions from Leon Rochester, Su Dong, Bruce Schumm, Tracy Usher, Mourad Daoudi, Richard Dubois, Joe Perl are essential to my analyses.

I would like to mention with gratitude the ideas in both theoretical physics and ideal society I have received over the years from Prof. Igor Dremin (Moscow) and Prof. Paul Tsai (Stanford). Both have been my good friends, and have been instrumental

in introducing me to the finer things of life. While Prof. X Cai (Wuhan) inspired my interest to search for QGP initially, it was Prof. R. Hwa (Oregon) who paved me a route to the U.S where I had an opportunity to turn my interest into a joy in the domain of high energy physics. Along my harsh journey to the U.S from China was the critical aid from Prof. G Orlova (Moscow) and Prof. E R Ganssauge (Marburg).

The support from parents and all family members back home are especially deserving of thanks. Their wish and hope always strengthen me in the face of constant adversity. Also, special thanks goes to Family Le in Portland where I had a place to celebrate Christmas Eves.

Lastly, I would like to thank the United States of America, a great country, where my dream came to be true. This work was supported by the U.S. Department of Energy grant DE-FG06-85ER40224.

This thesis is dedicated to my grandfather, a man I respected most, who passed away when I was about to start the last chapter. His spirit will accompany me and lighten the way to my goal as always.

Contents

List of Tables

List of Figures

Chapter 1

Introduction

"It is fun to speculate about the way quarks would behave if they were real particles".
-Murray Gell-Mann (1964).

In 1964 quarks made their appearance in particle physics: Gell-Mann and Zweig developed a group theoretical scheme to order hadrons (mesons and baryons) into supermultiplets of $SU(3)$. It is this scheme that resolved the dilemma of the large variety of hadrons which at one time were believed to be truly elementary particles. Thus, hadrons are not 'elementary' constituents of matter, but are made from more fundamental particles: the quarks. Quarks have a spin quantum number of $1/2$, with fractional charges. For each type of quark q there is an antiquark $\overline{q}$, of the same mass but opposite charge. Quarks and antiquarks can combine to form hadrons, for instance, baryons (such as nucleons) are made of three quarks while mesons are quark-antiquark bound states. In 1964 the known hadrons could all be explained by combinations of three kinds (or flavors) of quarks, called *up*, *down*, and *strange*. Since then further hadrons have been discovered, requiring new flavors such as *charm*, *top* and *bottom*.

At that time the general belief was that of quarks as fictitious mathematic objects rather than as real physical states. However, this changed as experimentalists were discovering more new particles which agreed with the predicted $SU(3)$ supermultiplets. Most importantly, the deep inelastic nucleon scattering provided evidence

for the composite nature of nucleons. The constituents of nucleons were found to behave as point-like particles with spin 1/2 when probed with leptons. A study of electromagnetic and weak cross sections revealed that these constituents must have fractional charges. So, the constituents were identified as the quarks introduced by Gell-Mann and Zweig.

To explain hadrons as dynamically bound states, gluons were introduced. They play the role of glue that holds the quarks together. The fact that only 50% of total nucleon momentum could be seen by deep inelastic lepton-nucleon scattering experiments offered the first, albeit somewhat indirect, evidence of the existence of gluons which are responsible for interactions between quarks in hadrons.

The existence of the Δ^{++}, a baryon with three quarks of the same flavor, all in the same angular momentum and isospin state, called for the introduction of the concept of color to avoid violation of the Pauli exclusion principle, by allowing the quarks to have three degrees of 'color' freedom. Later measurements of the ratio

$$R = \frac{\sigma(e^+e^- \to Hadrons)}{\sigma(e^+e^- \to \mu^+\mu^-)} = N_c \sum_f Q_f^2,$$

which in the lowest order is equal to the sum of the squared charges of the contributing quarks flavors times $N_c(= 3)$ the color degrees of freedom, confirmed that the number of colors is indeed three.

Five different flavors of quarks and antiquarks had been identified in experiments. To complete the pattern a 6th flavor known as *top*, was required: this has been discovered recently by the CDF and D0 experiments at Fermilab [1]. As a summary, these quarks with their properties, are shown in Table 1.1 [2]. The corresponding charges for the antiquarks are the same in magnitude but opposite in sign.

Until 1972 there was no real theory of the interactions between quarks (the strong interaction); there were several models such as the parton model, which were able to describe a certain part of the experimental data, but none of the models was able to give a consistent and overall description of the experimental results. The situation changed significantly with the discovery of the asymptotic freedom (Gross 1973, Politzer 1973). The couplings between quarks and gluons were described with a non-Abelian theory, which in turn allowed to perform quantitative calculations and

quark	symbol	charge	spin	mass
up	u	2/3	1/2	$2 \sim 8$ MeV
down	d	$-1/3$	1/2	$5 \sim 15$ MeV
charm	c	2/3	1/2	$1.0 \sim 1.6$ GeV
strange	s	$-1/3$	1/2	$100 \sim 300$ MeV
top	t	2/3	1/2	$164 \sim 184$ GeV
bottom	b	$-1/3$	1/2	$4.1 \sim 4.5$ GeV

Table 1.1: Quark charge and mass

to predict certain features of strong interactions(Fritzsch 1973). The theory of the the strong interactions, Quantum Chromodynamics (QCD), was born! Nowadays, QCD can explain - at least qualitatively - most of strong interaction phenomena, ranging from bound states of quarks (baryons and mesons), to asymptotic freedom at short distances. However, the precision of QCD tests is limited to typically 10% for the following reasons: perturbative calculations are difficult due to the large number of diagrams involved, and the convergence of the series expansion in strong coupling constant α_s is poor due to the large value of the strong coupling constant. It is important to push the accuracy of QCD tests as far as possible, and to expand the tests to many processes.

Major contributions to the establishment of QCD have come from the study of deep inelastic lepton-nucleon scattering, hadron-hadron collisions, and in particular from the study of hadronic productions in e^+e^- annihilation. In e^+e^- collisions the initial state is simple and known, therefore allowing for clean tests of QCD. The SLAC linear collider (SLC) is the first e^+e^- linear collider successfully operated at the peak of the Z^0 resonance, offering an ideal laboratory for many tests of QCD.

This thesis attempts to investigate some properties of the transition from color triplet quarks to color singlet hadrons, a process governed by the strong interaction which is described by QCD. The analyses in this thesis are based on a total of 86679 well measured hadronic events collected by the SLC Large Detector (SLD).

The thesis is organized as follows. In Chapter 2, the basic theory of QCD is reviewed, with special emphasis on the process of hadronic production in e^+e^- interactions. Chapter 3 describes our SLC/SLD facilities that made the production/measurement of $e^+e^- \rightarrow$ hadrons at the Z^0 resonance possible. Special attention is focused on the tracking system which is the most relevant to this analysis. The hadronic event selection is described in Chapter 4. Studies of the detector tracking efficiency is presented in Chapter 5. The subsequent chapters are dedicated to the experimental analyses of multiparticle production and comparison with QCD: a measurement of the charged-particle multiplicity distribution is presented in Chapter 6; an analysis of the ratio of cumulant to factorial moments is presented in Chapter 7; an investigation of intermittency is presented in Chapter 8. Finally, our summary and conclusion are given in Chapter 9.

Chapter 2

Theory

2.1 Basics of QCD

Quantum Chromodynamics (QCD) [3, 4] is commonly accepted as the fundamental theory of the strong interaction. QCD consistently predicts and describes many aspects of strong interaction phenomena [5], while depending only upon a few free parameters which are not determined by theory: the strong coupling constant α_s (or QCD coupling constant) and the quark masses. However, the precision of QCD tests is limited to about 10% for the following reasons: perturbative calculations are difficult due to the large number of diagrams involved, and the convergence of the series expansion in α_s is poor due to the large value of the strong coupling constant. In addition, non-perturbative effects such as hadronization have to be taken into account, which today must be modeled. Thus, due to these limitations, the quantitative tests of QCD can only be made at the parton level. By far, experimental tests of this theory are not as precise as Quantum Electrodynamics (QED), the standard model of electromagnetic interactions. The basic ideas and features of QCD are schematically given in Table 2.1, with a comparison with QED.

QCD describes the interaction of colored spin 1/2 quarks with colored spin 1 gluons, which are the intermediate bosons of the strong interaction. The force couples to the color charge of the quarks and gluons. Since gluons themselves carry color charge, they exhibit the features of gluon self-coupling as shown in Fig. 2.1, in contrast

	QED	QCD
fermions	leptons (e, μ, τ)	quarks (u, d, s, c, b, t)
force couples to	electric charge	3 color charges
exchange quantum	photon (γ)	gluons (g)
coupling constant	$\alpha(Q^2 = 0) = 1/137$	$\alpha_s(Q^2 = M_Z^2) \approx 0.12$
free particles	leptons (e, μ, τ)	hadrons (color singlet)
theory	up to $O(\alpha^4)$	up to $O(\alpha_s^2)$
precision	$10^{-6}...10^{-7}$	5%...20%

Table 2.1: Comparison of the basic properties and features of QED and QCD.

Figure 2.1: Three fundamental vertices in QCD. The coupling strengths of all three vertices are described by the same constant, g_s, which is related to the QCD coupling constant by $\alpha_s = g_s^2/4\pi$.

to photons of QED which do not couple to themselves. As a direct consequence, the QCD coupling constant, α_s, has a strong dependence on the energy scale μ of interaction [6], as expressed by the renormalization group equation

$$\mu^2 \partial \alpha_s / \partial \mu^2 = -(\beta_0 \alpha_s^2 + \beta_1 \alpha_s^3 + \beta_2 \alpha_s^4 + \cdots). \tag{2.1}$$

The coefficients have been calculated [7, 8]:

$$\beta_0 = (11 - \frac{2}{3} N_F)/4\pi = 0.610, \tag{2.2}$$

$$\beta_1 = (102 - \frac{38}{3}N_F)/(4\pi)^2 = 0.245, \tag{2.3}$$

and

$$\beta_2 = (\frac{2857}{2} - \frac{5033}{18}N_F + \frac{325}{54}N_F^2)/(4\pi)^3 = 0.091, \tag{2.4}$$

where N_F is the number of quark flavors with mass less than the energy scale μ. The numerical values were computed assuming five active flavors ($N_F = 5$). The lowest order coefficients of the beta functions, in particular β_0, are positive, which leads to a decrease of the coupling with increasing energy μ. This is different from QED, where the beta function has the other sign, causing α to increase with μ.

The solution to Eq. 2.1 in lowest order,

$$\mu^2 \partial\alpha_s/\partial\mu^2 \equiv \partial\alpha_s/\partial \ln \mu^2 = -\beta_0\alpha_s^2 \tag{2.5}$$

can be written as

$$\alpha_s(\mu) = \alpha_s(\mu_0)/[1 + \beta_0\alpha_s(\mu_0)\ln(\mu^2/\mu_0^2)], \tag{2.6}$$

where μ_0 is a reference scale. Defining

$$\Lambda = \mu_0 \exp[-1/2\beta_0\alpha_s(\mu_0)] \tag{2.7}$$

leads to the equivalent expression

$$\alpha_s(\mu) = \frac{1}{\beta_0 \ln(\mu^2/\Lambda^2)}. \tag{2.8}$$

There is one free parameter, which can be either chosen as $\alpha_s(\mu_0)$ for a given scale μ_0, or as Λ. The parameter Λ indicates the boundary between non-perturbative and perturbative energy ranges. It depends through β_0 on the number of flavors N_F.

It can be seen in Eq. 2.8 that α_s is a function of the energy scale. α_s is the fundamental parameter of QCD, and must be deduced from experiment. The μ dependence of α_s also depends on the choices of the α_s formula. The most commonly used formula is

$$\frac{\alpha_s(\mu)}{4\pi} = \frac{1}{\beta_0 \ln(\mu^2/\Lambda^2)}\left(1 - \frac{\beta_1}{\beta_0^2}\frac{\ln\ln(\mu^2/\Lambda^2)}{\ln(\mu^2/\Lambda^2)}\right), \tag{2.9}$$

which is the solution to the Eq. 2.1 in next-to-leading order [9].

Customarily, Λ has been used as the fundamental parameter in QCD due to a lack of a natural scale $\mu_0 \gg \Lambda$. Today we have a convenient reference scale $\mu_0 = m_Z$, the mass of Z boson, thus the QCD coupling constant can be expressed in terms of $\alpha_s(m_Z)$. Figure 2.2 shows the characteristic energy dependence of α_s, which is often referred to

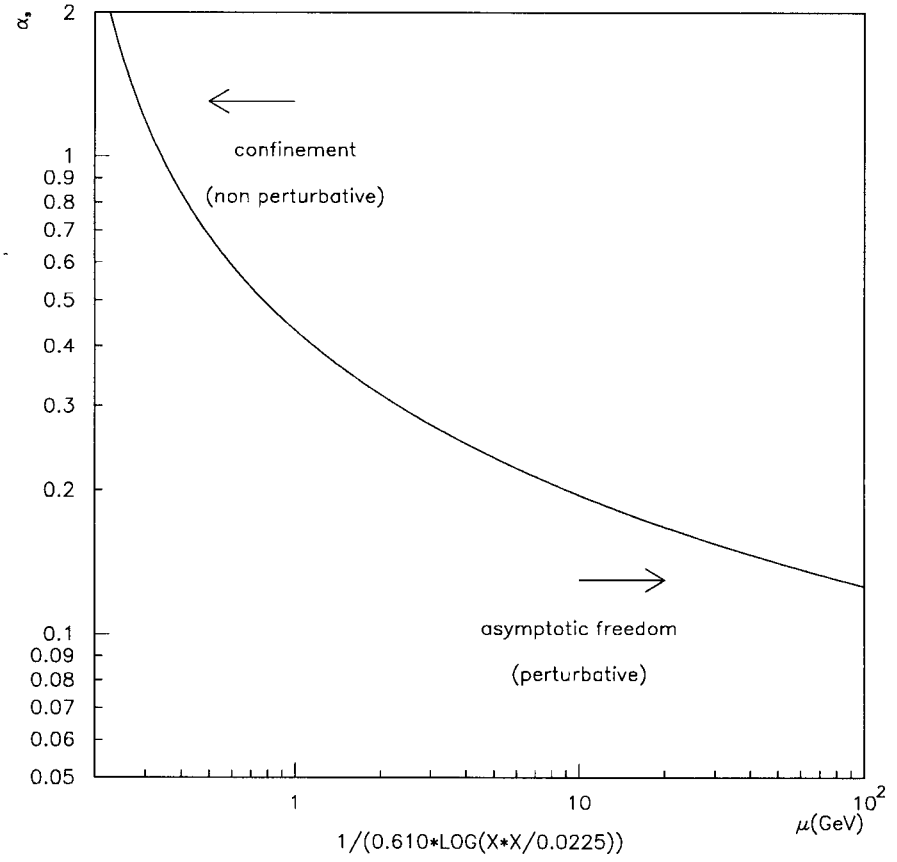

Figure 2.2: Illustration of the behavior of the QCD coupling constant α_s as a function of the energy scale, μ. The coupling is large at small μ (i.e., large distance) where confinement occurs, but decrease to zero at large μ (asymptotic freedom).

as the 'running coupling constant'. With increasing energy (or equivalently decreasing distance) the coupling strength vanishes logarithmically, an effect which is also called

'asymptotic freedom'. In the regions (say above 1 GeV) where α_s is sufficiently small, QCD can be solved by perturbative methods. At large distance or small energy scale, however, α_s becomes very large, such that perturbative calculations no longer apply. In this regime (also called 'confinement'), nonperturbative methods such as calculations on a lattice must be used to describe the strong interaction between quarks and gluons. Such methods, however, have not yet reached the same level of predictive power as perturbative theory does in the region of large μ. Thus, the dynamics of QCD at large distances may be regarded as rather unsolved. Some phenomenological models were therefore developed to describe the confinement, for instance by modeling the process of 'hadronization' — the transformation of quarks and gluons into hadrons — to the extent that connection between measurements of hadrons and the dynamics of quarks and gluons predicted by perturbative QCD could be made.

Hadronization is thus a non-perturbative process which typically happens at energy scales smaller than, or of the order of, a few GeV, at the scale of hadron masses. The average transverse momentum of hadrons with respect to the direction of the quark or gluon motion should be independent of the energy of the parton. It is therefore expected that at large enough energies, hadrons appear as jets of particles, more or less collimated around the direction of the quark and gluon. The physics of hadronic production is thus an important tool for tests of QCD.

2.2 Hadronic Production in e^+e^-

Hadronic final states of highly energetic e^+e^- annihilations have proven to be an ideal laboratory to perform precise tests of QCD for three reasons: (a) the initial state is well defined; (b) the high momentum quarks and gluons form jets (tight bundles of hadrons), which preserve the energy and direction of the primary partons to a good approximation; (c) suppressed backgrounds. The process of $e^+e^- \rightarrow$ *hadrons* as shown schematically in Fig. 2.3 can be generally distinguished in terms of four phases:

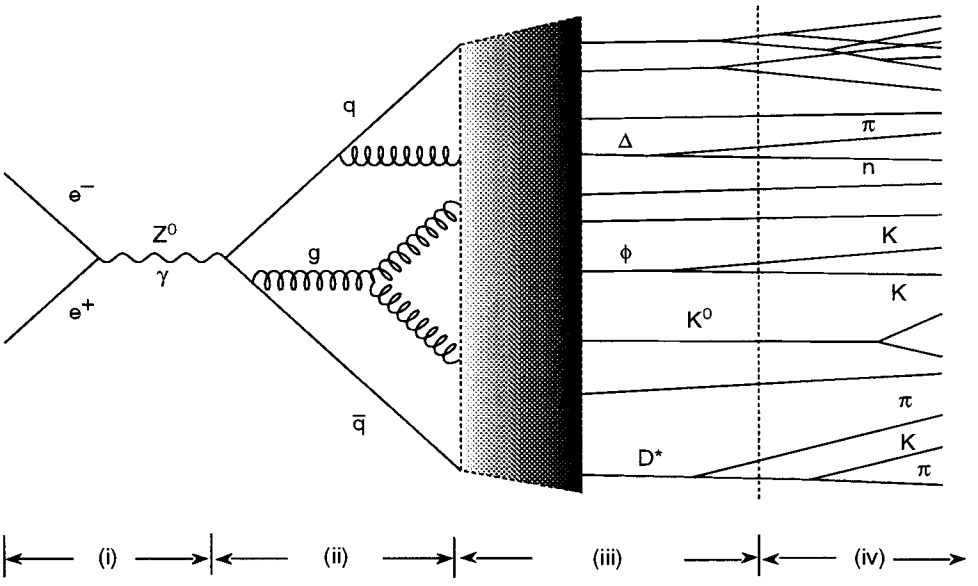

Figure 2.3: The phases in the process of hadronic production in e^+e^- annihilation.

(i) Production of a $q\overline{q}$ pair. This phase is described by the electroweak theory. Electroweak corrections, the most important of which is initial state bremsstrahlung, are not included in the figure.

(ii) The initial quarks may radiate gluons, which in turn may radiate $q\overline{q}$ pairs or gluons, thus leading to a parton shower. This phase is described by perturbative QCD.

(iii) The colored partons produced in phase (ii) fragment into colorless hadrons. This phase is explained by phenomenological models, since perturbative QCD can no longer be used here due to the large value of α_s.

(iv) The unstable hadrons produced in phase (iii) decay into the experimentally observed hadrons. Again, QCD can't be used here and the experimentally determined branching ratios are used to predict the outcome. For weak decays, one can attempt to use electroweak theory, but in practice one resorts to a phenomenological description here as well.

In the following sections the four phases will be described in more detail.

2.2.1 Fermion pair production $e^+e^- \to f\overline{f}$

The Feynman diagrams of the process $e^+e^- \to f\overline{f}$ at the lowest order are shown in Fig. 2.4. The fermion f can be either a lepton (e, μ, τ), a neutrino $(\nu_e, \nu_\mu, \nu_\tau)$ or a quark (u, d, s, c, b). There are two basic interactions which contribute to this process: the exchange of a virtual photon, which is a pure electromagnetic interaction; and the exchange of a vector boson Z^0, which is a pure weak interaction. Thus, the cross section of the process $e^+e^- \to f\overline{f}$ is proportional to the square of the sum of matrix elements of two diagrams: $|M_\gamma + M_Z|^2$. In the lowest order approximation, the total cross section at the center of mass energy, $\sqrt{s} \gg m_f$, is given by [9]

$$\sigma(e^+e^- \to f\overline{f}) = N_c \cdot \frac{4\pi}{3}(\alpha^2/s)[Q_e^2 Q_f^2 + (V_e^2 + A_e^2)(V_f^2 + A_f^2)|\chi|^2 + 2Q_e Q_f V_e V_f Re(\chi)], \tag{2.10}$$

where α is the electromagnetic fine structure constant, Q_f is the electric charge of the fermion f, and V_f and A_f denote the vector and axial vector couplings to fermions. N_c is the number of colors of the fermion: 1 for leptons, 3 for quarks. The function χ describes the Breit-Wigner form of the Z^0 resonance:

$$\chi = \frac{1}{4\sin^2(\theta_W)\cos^2(\theta_W)} \cdot \frac{s}{s - m_Z^2 + i m_Z \Gamma_Z}, \tag{2.11}$$

with m_Z and Γ_Z being the mass and total decay width of the Z^0 boson, and θ_W the weak mixing angle. The first term in Eq. 2.10 describes the photon s-channel process as shown in Fig. 2.4(a), the second term describes the Z^0 exchange as shown in Fig. 2.4(b) and the third term represents the contribution from the $\gamma - Z$ interference. At $\sqrt{s} \approx m_Z$, the Z^0 exchange term is dominant $\sigma_Z/\sigma_\gamma \sim 1100$, and the interference term vanishes, forming a resonance near $\sqrt{s} \approx m_Z$ with a width Γ_Z. The branching ratios of Z^0 to fermion pairs are listed in Table 2.2.

As is mentioned above, the total cross section in Eq. 2.10 is the lowest order approximation. Further corrections should be applied for initial state radiation of photons and final state radiation of gluons and photons [10] in order to compare with experimentally observed cross sections.

The effect of initial state radiation in the process $e^+e^- \to$ hadrons has a strong dependence on $\sqrt{s}$. Due to the radiation of photons with energy E_γ from the incident

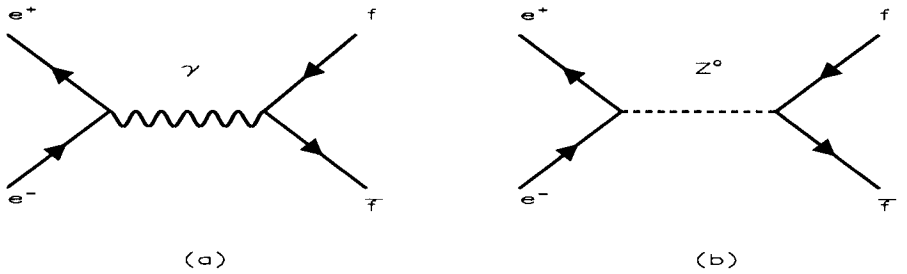

Figure 2.4: Fermion pair production $e^+e^- \rightarrow f\overline{f}$ in lowest order.

M_Z	91.187 ± 0.007 GeV/c^2
Γ_Z	2.490 ± 0.007 GeV
branching ratio (%)	
e^+e^-	3.366 ± 0.008
$\mu^+\mu^-$	3.367 ± 0.013
$\tau^+\tau^-$	3.360 ± 0.015
$\nu\overline{\nu}$	20.01 ± 0.16
$q\overline{q}$	69.90 ± 0.15

Table 2.2: Z^0 properties.

electrons, the hadronic system is boosted and the energy in its rest frame is reduced:

$$s'/s = 1 - 2E_\gamma/\sqrt{s}. \tag{2.12}$$

The probability for photon radiation increases with the ratio $\sigma(s')/\sigma(s)$. Therefore initial state radiation is negligibly small at Z^0 resonance [11]. In addition, the interference between initial and final state radiation is very small near the Z^0 [10].

2.2.2 Parton Production

It is in this phase where perturbative QCD plays an important role. The primary quarks produced in phase (i) of the diagram in Fig. 2.4 can radiate gluons. A parton cascade may be developed by subsequent branching of these gluons into quarks or gluons. The parton configurations can be calculated approximately within QCD by using two approaches: Matrix Element (ME) and Parton Shower (PS). In the ME approach, the Feynman diagrams are calculated exactly order by order. The PS approach is based on the framework of the leading logarithm approximation (LLA). Both methods are complementary: ME offers a more accurate description of hadronic events on the jet level, while PS is better suited to describe the structure of the jets.

Matrix Elements

In principle, the parton configurations can be calculated exactly order by order using the ME approach. However, the calculations of the Feynman diagrams for higher orders becomes increasingly difficult, so that only calculations up to second order, $O(\alpha_s^2)$, exist. Thus, the final state in this approach consists of at most 4 partons which are allowed to hadronize according to one of the fragmentation models described below. Figure 2.5 shows the Feynman diagrams for the matrix element calculation up to $O(\alpha_s^2)$.

The first order QCD correction to the process $e^+e^- \rightarrow q\overline{q}$ takes into account the gluon radiation from q or $\overline{q}$: this yields $e^+e^- \rightarrow q\overline{q}g$. The cross section for this configuration (3 partons) is calculated [12] for massless quarks as

$$\frac{d\sigma}{dx_1 dx_2} = \sigma_0 \frac{2\alpha_s}{3\pi} \frac{x_1^2 + x_2^2}{(1-x_1)(1-x_2)}, \quad 0 \leq x_i \leq 1, \quad i = 1,2,3 \tag{2.13}$$

where σ_0 corresponds to the cross section for $e^+e^- \rightarrow q\overline{q}$, and x_i is the scaled energy variable in the CM frame

$$x_i = 2E_i/\sqrt{s}, \quad i = q, \overline{q}, g, \tag{2.14}$$

satisfying $\sum_i x_i = 2$. The cross section in Eq. 2.13 is divergent for $x_1 \rightarrow 1$ or $x_2 \rightarrow 1$. However, these singularities are canceled by corresponding poles in the first order

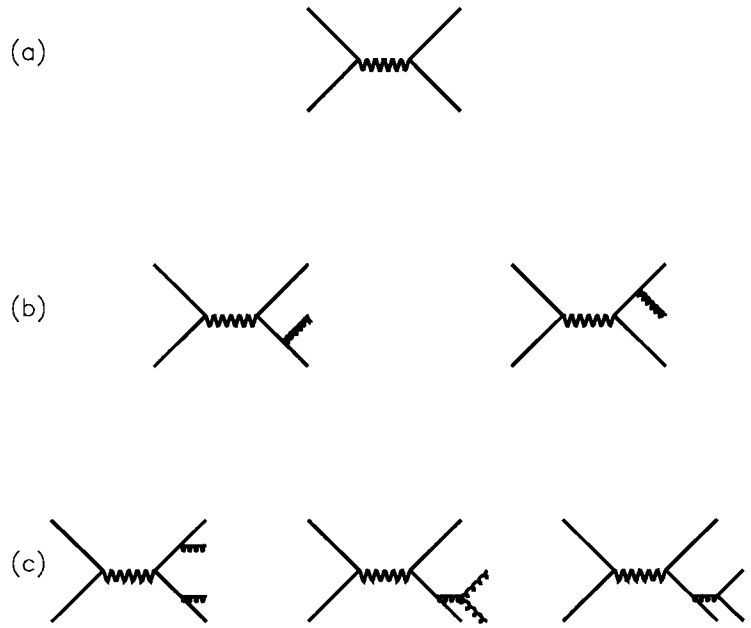

Figure 2.5: Feynman diagrams for matrix element calculation up to $O(\alpha_s^2)$.

vertex and propagator correction, therefore the total cross section is finite. In second order $O(\alpha_s^2)$, two further parton configurations are added to the first order: $e^+e^- \rightarrow q\bar{q}gg$ and $e^+e^- \rightarrow q\bar{q}q'\bar{q}'$. The cross section for 4 parton configurations has been calculated [13]. In ME Monte Carlo models the configurations with two, three and four partons are generated. In order to separate these topologies a parton resolution criterion has to be used, for example the smallest invariant mass m_{ij} of any two partons. The quarks and gluons are then transformed into hadrons using a fragmentation model.

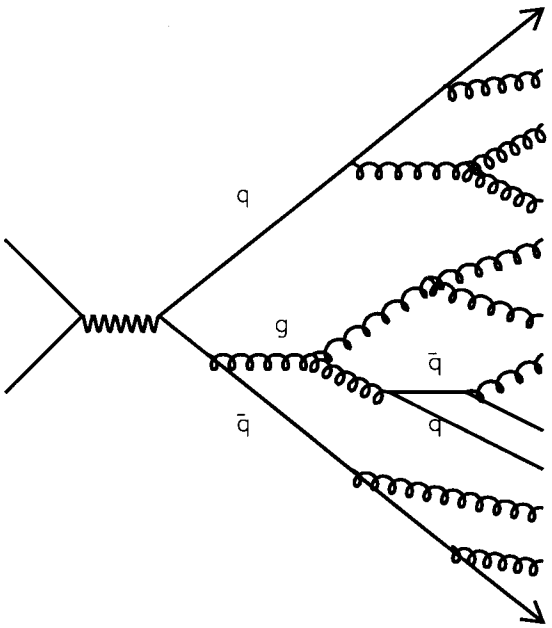

Figure 2.6: Schematic illustration of a parton shower.

Parton Shower

When extended to multi-parton configurations, the calculation for the cross section in the ME approach becomes unrealistic due to the vast number of Feynman diagrams contributed. PS [14] offers an alternative approach to these excessive calculations. This approach is based on the framework of the leading logarithmic approximation [15], where only the leading term in the perturbative QCD expansion is retained. The production of partons can be viewed as the successive branching of $a \rightarrow bc$. Here, a is the mother parton and b and c are the daughters. Each daughter is allowed to branch further, so that a tree-like structure is developed as sketched in Fig. 2.6. The

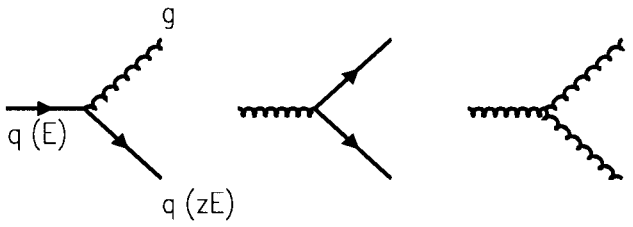

Figure 2.7: Branching processes.

allowed branching processes in QCD are: $q \rightarrow qg$, $g \rightarrow q\overline{q}$ and $g \rightarrow gg$, as shown in Fig. 2.7. The probabilities for these branching processes are given by Altarelli-Parisi splitting kernels [16]

$$P_{q\rightarrow qg}(z) = C_F(\frac{1+z^2}{1-z}), \tag{2.15}$$

$$P_{g\rightarrow gg}(z) = 2C_G\frac{(1-z(1-z))^2}{z(1-z)}, \tag{2.16}$$

and

$$P_{g\rightarrow q\overline{q}}(z) = \frac{N_f}{2}(z^2+(1-z)^2), \tag{2.17}$$

where z specifies the energy fraction taken by the daughters in the process $a \rightarrow bc$, with b taking z and c taking $1-z$. C_F and C_G are color factors for quarks (3/4) and gluons (3) respectively, and N_f is the number of active quark flavors.

The probability P for a branching to occur during a small change dt of the evolution parameter t is given by the Altarelli-Parisi equations [16]

$$\frac{dP_{a\rightarrow bc}}{dt} = \int dz\frac{\alpha_s(Q^2)}{2\pi}P_{a\rightarrow bc}(z), \tag{2.18}$$

with evolution parameter t

$$t = \ln(Q^2/\Lambda^2). \tag{2.19}$$

Thus, the iterative use of the Altarelli-Parisi equations in PS models generates a sequence of parton branchings: the parton shower. When Q approaches Λ, perturbative QCD is no longer applicable and therefore a cutoff parameter $Q_0 = O(1GeV)$, corresponding to an effective gluon mass, is introduced to terminate the showering.

The higher order corrections to the leading logarithm approximation (LLA) are taken into account [17], such as MLLA (M for modified), DLA (D for double), or NLLA (N for next-to-). The PS models based on these frameworks are expected to describe the coherent effects of soft gluons inside a jet and the particle flow in between jets.

2.2.3 Hadronization

Once the initial parton configurations are determined from the perturative QCD calculations either with the Matrix Element approach or the Parton Shower approach, they must be converted into color-singlet hadrons due to color confinement. The process of this conversion (phase (iii) of Fig. 2.3) is called hadronization or fragmentation. This process takes place in the non-perturbative region as shown in Fig. 2.2, since the running of the coupling constant makes α_s too large for perturbative QCD to be applied. Therefore, the hadronization must be implemented by a model.

How big is the task of the hadronization model, depends on the initial parton configuration. In the case of $O(\alpha_s^2)$ ME, at most four partons at an energy scale (invariant mass of two partons) exceeding 10 GeV are created at the Z^0 resonance. This implies that the hadronization model has to bridge a big gap from the parton to hadron level which is governed by multiplicities of 15-20 (before decays) and mass scales of 1 GeV or less. In contrast, the situation is much better in the case of PS, where parton energy scales Q_0 can go down to about 1 GeV (virtuality of gluons). The average parton multiplicity of 9 at the Z^0 resonance is much closer to the number of hadrons produced than in the ME case. This means that the task hadronization model has to accomplish is relatively smaller for the PS. Consequently the hadronization model dependence is much reduced in comparison with the ME program. One should note that hadronization refers both to non-perturbative effects and to missing higher order terms in the perturbative calculation.

There exists three major models for hadronization:

- Independent fragmentation;
- String fragmentation;
- Cluster fragmentation.

The independent fragmentation was proposed in the 1970's [18] and has been gradually phased out. In the following sections I will describe the string fragmentation model and cluster fragmentation model which are used extensively and have been demonstrated to reproduce data quite successfully. A very detailed review of these and other hadronization models can be found in [19].

String fragmentation

The string fragmentation model is based on a QCD-inspired idea that a color flux tube (also called 'string') is stretched between two partons moving away from each other [20]. If the color field along the tube is assumed to be uniform, this automatically leads to a confinement picture with a linearly rising potential, $E(r) \sim kr$, where r is the separation between partons and k is a string constant (the energy per unit length).

Consider a simple $q\overline{q}$ system: as q and $\overline{q}$ move apart, the potential energy stored in the string increases and the string may break up via the spontaneous formation of a $q'\overline{q}'$ pair in the color field. Thus the string splits into two segments (or two color singlet systems) $q\overline{q}'$ and $q'\overline{q}$. If the invariant mass of either of the these segments is large enough, further breaks may occur, and so on until only ordinary hadrons remain. Typically, a break occurs when the q and the $\overline{q}$ of a color singlet system are 1-5 fm apart in the $q\overline{q}$ rest frame. Each hadron is then formed from the quark from one break and the antiquark from an adjacent break. A schematic view of string fragmentation is shown in Fig. 2.8.

In a color field a massless $q'\overline{q}'$ pair can classically be created at one point and then pulled apart by the field. If the quarks have mass or transverse momentum, however, they must classically be produced at a certain distance so that the field energy

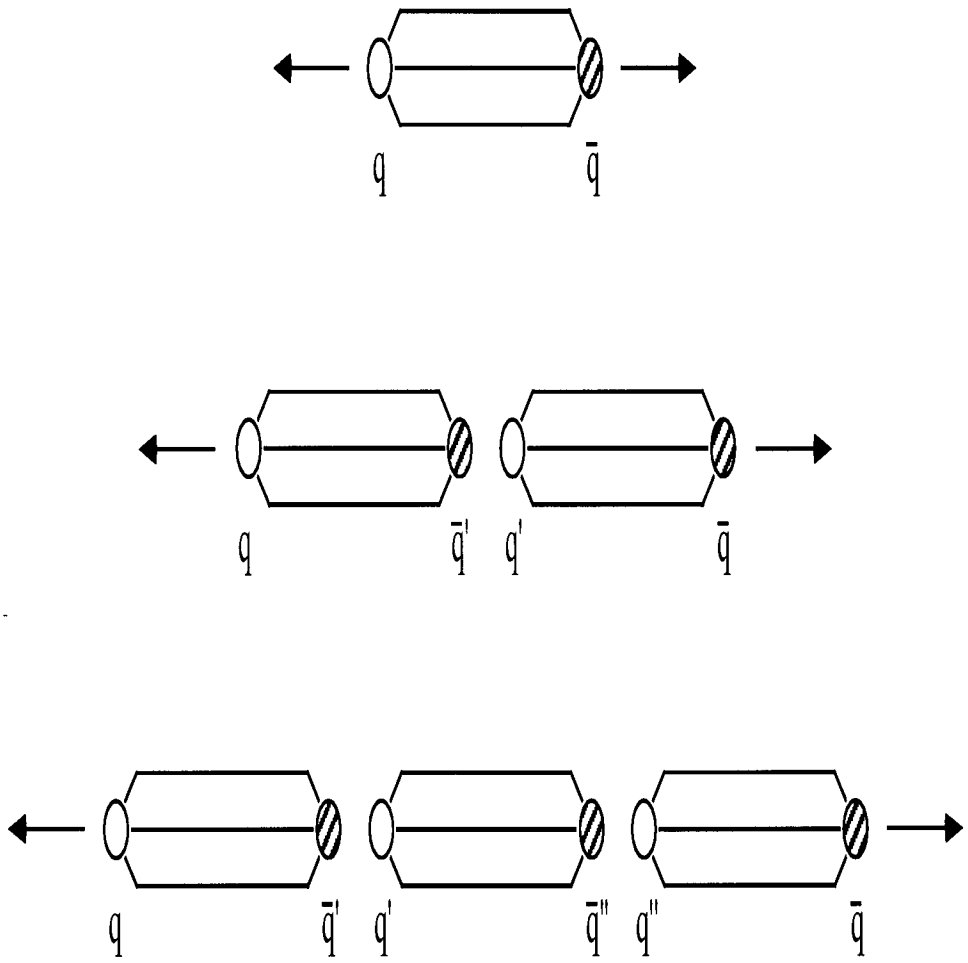

Figure 2.8: A schematic representation of string fragmentation.

between them can be transformed into the transverse mass m_T. Quantum mechanically, the quarks may be created in one point and then tunnel out to the classically allowed region. The massive quark production probability for this tunneling process is proportional to [21]:

$$\exp(-\pi m_T^2/k) = \exp(-\pi m^2/k)\exp(-\pi p_T^2/k). \tag{2.20}$$

This formulation leads to the transverse momentum spectrum of hadrons with respect to the original quark direction and explains the limited p_T distribution of particles in the jet. It also implies a suppression of heavy quark production $u : d : s : c \approx 1 :$

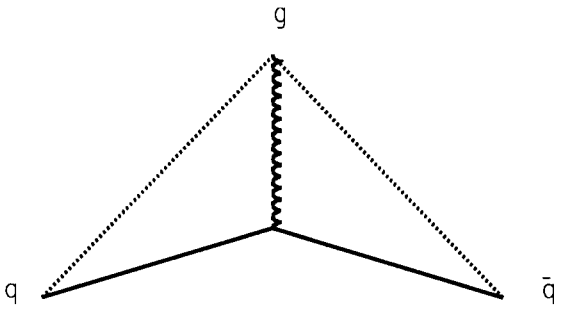

Figure 2.9: The string scheme in a $q\overline{q}g$.

$1 : 0.3 : 10^{-11}$. Charm and heavier quarks are hence not expected to be produced in hadronization.

The simplest scheme for baryon production is that in addition to quark-antiquark pairs, diquark-antidiquark pairs are also produced occasionally in the color field [22]. The production of different hadron species can be steered by parameters defining the strange quark content, the spin probabilities (for pseudoscalar and vector mesons), the number of diquarks created, etc.

The picture of string fragmentation above is simplified for a $q\overline{q}$ system. If several partons are moving apart from a common origin, the details of the string drawing become more complicated. For a $q\overline{q}g$ system, the gluon is treated as a 'kink' in the string that is stretched between the two quarks as showed in Fig. 2.9. One consequence of this scheme leads to a 'string effect': i.e that less particles are produced in between the quark and antiquark jets in comparison to the other two inter-jet regions, as observed experimentally.

The JETSET Monte Carlo Model [23] implemented with the PS plus string fragmention reproduces data quite successfully and is used as the basis of analysis in this thesis.

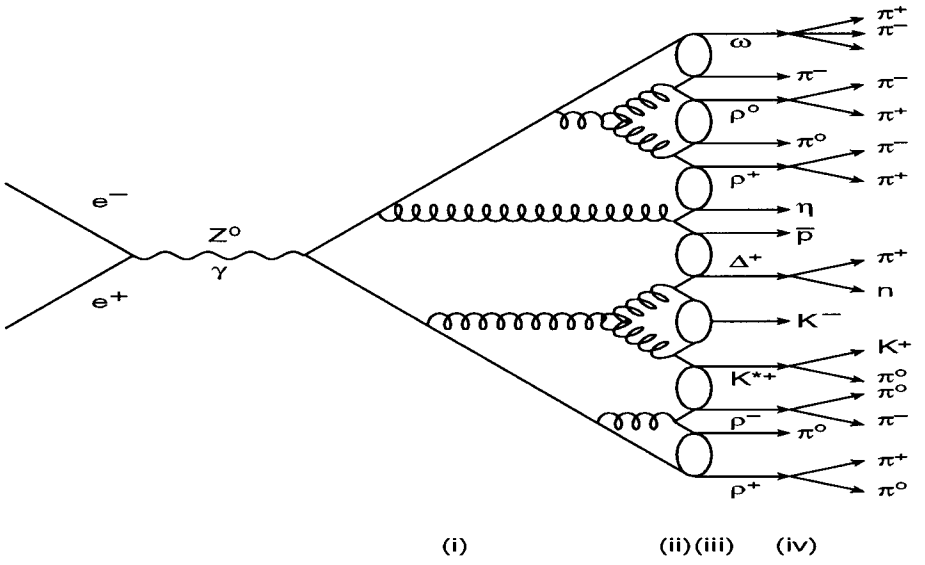

Figure 2.10: Schematic illustration of cluster fragmentation

Cluster fragmentation

The concept of cluster fragmentation offers the great promise of a simple description of hadronization [24]. The cluster fragmentation model as implemented in the HERWIG Monte Carlo program [25] should be used only for developed parton configurations as obtained in PS. A generic cluster scheme contains three components:

- breakup of $g \rightarrow q\overline{q}$ at the end of PS, and formation of colorless clusters from adjacent quarks and antiquarks,
- fragmentation of large (or heavy) clusters into smaller ones; and
- decay of clusters into hadrons.

This process is illustrated in Fig. 2.10

These clusters do not have any internal structure, and are characterized only by their mass and color content. They are assumed to be the basic units from which hadrons are produced. The fragmentation is assumed to be isotropic in the rest frame of the cluster. This simple model reproduced some features of the data, but as time went by and more data was accumulated, its shortcomings became apparent.

2.2.4 Decays

In the last phase of hadronic production in e^+e^- annihilation, the unstable particles decay into stable particles. For light hadrons their masses, decay modes, lifetimes and branching ratios have been well measured, and are built into the Monte Carlo [26]. For heavier particles, in particular charm and bottom, not all exclusive braching ratios have been measured. Therefore statistical models have to be invoked. For weak decays of heavy quark mesons the known matrix elements are taken.

2.2.5 Summary

In summary, one can say that the hadronic production in e^+e^- annihilation, particularly at the Z^0 resonance offers an ideal laboratory for QCD studies. The important advantages in comparison with e^+e^- annihilation at lower energies are

- large cross section and negligible background,
- relatively small fragmentation effects,
- suppressed initial state photon radiation.

Increasing the center of mass energy beyond the Z^0 resonance leads to a further reduction of hadronization effects, however the advantage of a large cross section is lost and initial state radiation becomes important. In the next chapter, I will describe the SLC/SLD facility that made the production and measurement of $e^+e^- \rightarrow$ hadrons at the Z^0 resonance possible.

Chapter 3

Experimental Apparatus: SLC and SLD

The data used in this thesis was acquired at the SLC/SLD facility at the Stanford Linear Accelerator Center (SLAC) located in Stanford, California. The SLAC Linear Collider (SLC) is a unique e^+e^- linear collider designed to produce the Z^0 boson. The produced Z^0 bosons are recorded by the SLC Large Detector (SLD), a state-of-the-art 4π coverage multi-purpose detector. This chapter will describe in some detail the SLC/SLD facility that made this work possible.

3.1 The SLAC Linear Collider

SLC is the world's only electron-positron linear collider, and it is designed to operate at the center-of-mass energy at the Z^0 resonance. The overall layout of the SLC is shown in Fig. 3.1. The SLC is operated at a machine cycle of 120 Hz. At the start of each cycle, two electron bunches are produced at the electron source; each bunch contains approximately 6×10^{10} electrons. The positron bunch produced in the previous cycle and one of the electron bunches are accelerated to 1.2 GeV, and stored in the south and north damping rings respectively. The second electron bunch is accelerated to about 30 GeV two thirds down the linac and diverted to hit a target to produce the positrons. The positrons are then transported back to the beginning

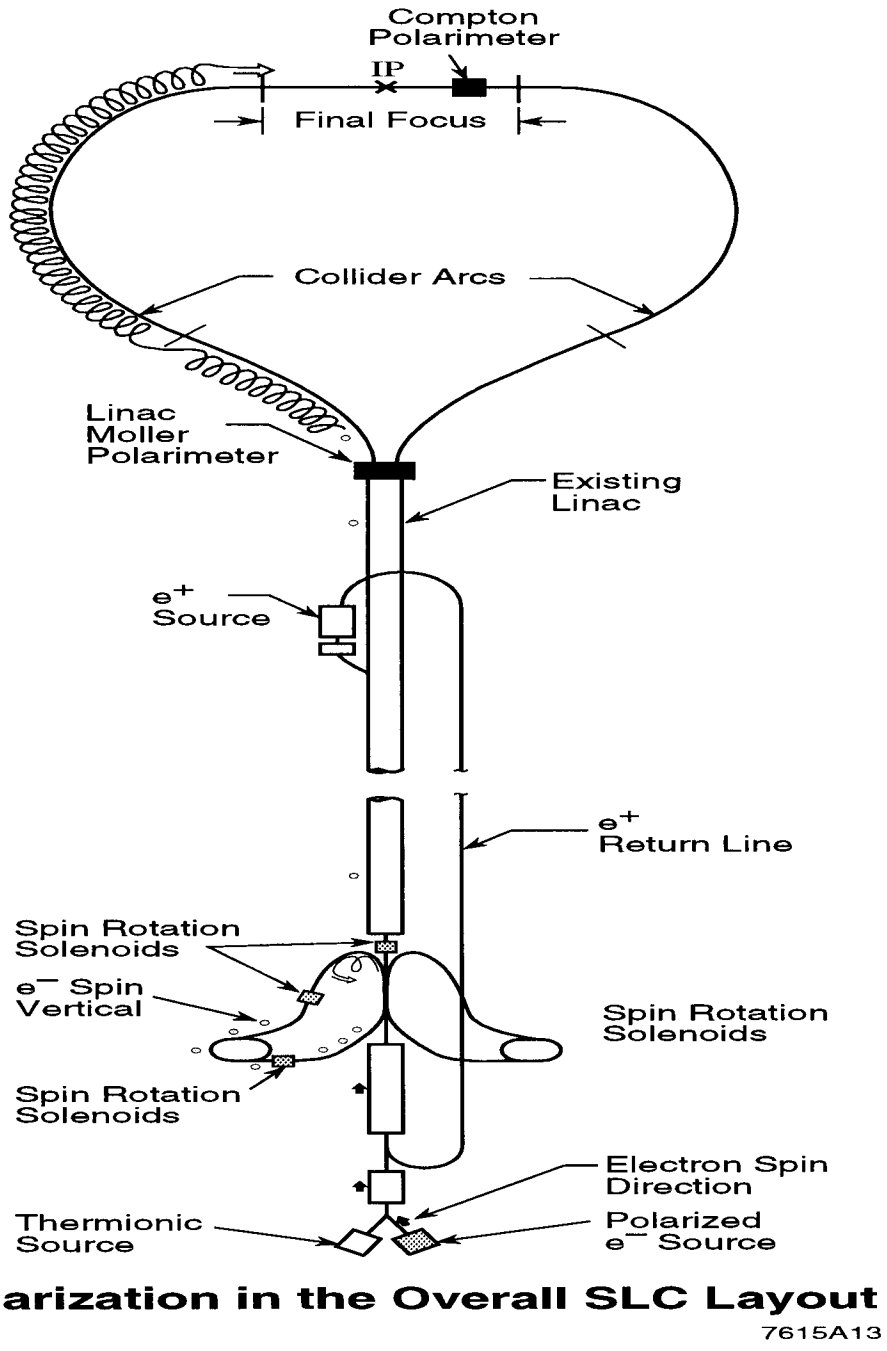

Figure 3.1: The layout of the SLAC Linear Collider.

of the the linac for the next cycle.

Sets of quadrupole magnets in the damping rings are used to compress the bunches and remove any energy fluctuation. The electron and positron bunches are then extracted from the damping rings, and accelerated up to 46.7 GeV along the 2 mile long linac. At the end of the linac, the electron and positron bunches are separated by a dipole magnet and directed into two arcs. Due to the synchrotron radiation in the transportation along the arcs, the energy of electrons and positrons is reduced to about 45.8 GeV. Before the collision, a set of superconducting focusing quadrupole magnets (SCFF) are used to compress the bunches to a diameter of $2\mu m$ on average. The electron and positron bunches are brought into head-on collision at the c.o.m energy of the Z^0 resonance, producing the Z^0 bosons. After collision, both bunches are extracted from beam line and dumped.

The luminosity for a linear collider can be expressed as

$$L = f_c \cdot \frac{n_1 n_2}{4\pi\sigma_x\sigma_y}, \tag{3.1}$$

where the n_1 and n_2 are the number of particles per bunch, f_c is the collision rate which is 120 Hz for the SLC, and $4\pi\sigma_x\sigma_y$ is the effective beam-beam crossing area. Typical SLC luminosity during the 1993 run was $L = 2.5 \cdot 10^{29} cm^{-2} s^{-1}$. The history of the integrated luminosity for the 1991 through 1995 runs of the SLD experiment is shown in Fig. 3.2.

The beam energies are measured by a pair of spectrometers that are placed just before the beam dumps. The actual energy measurement is performed by deflecting each beam horizontally, then vertically through a calibrated bend magnet, then horizontally again. The horizontal bends produce two synchrotron radiation stripes whose positions are measured by the Wire Imagine Synchrotron Radiation Detector (WISRD) [27]. The vertical distance between the two strips is inversely proportional to the energy of the beam. A schematic view of the WISRD spectrometer is shown in Fig. 3.3. The energy is measured for every beam crossing. The luminosity-weighted average center of mass energy for 1993 run was 91.26 ± 0.02 GeV.

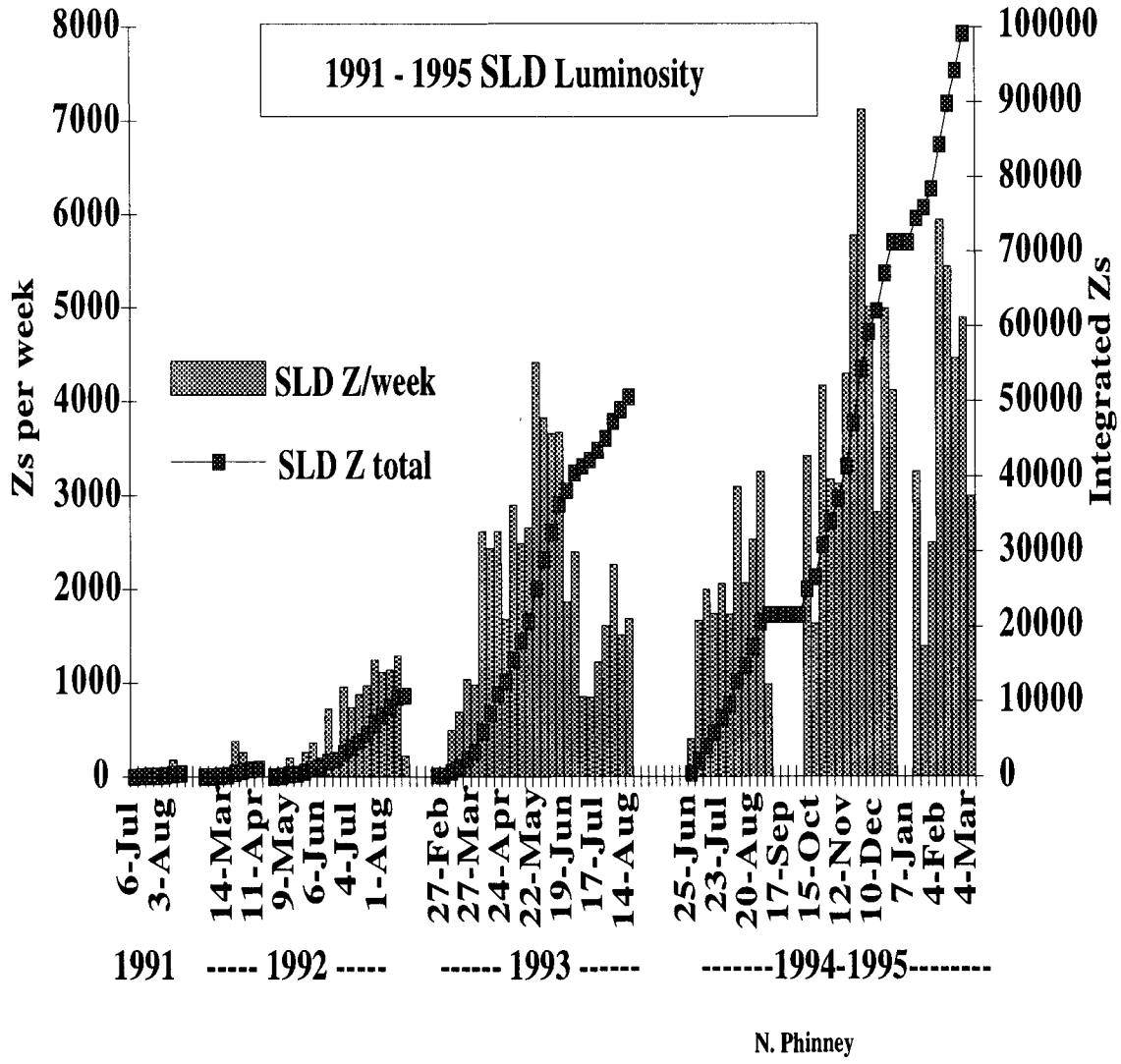

Figure 3.2: The history of the integrated luminosity for the 1991 through 1995 runs of the SLD experiment.

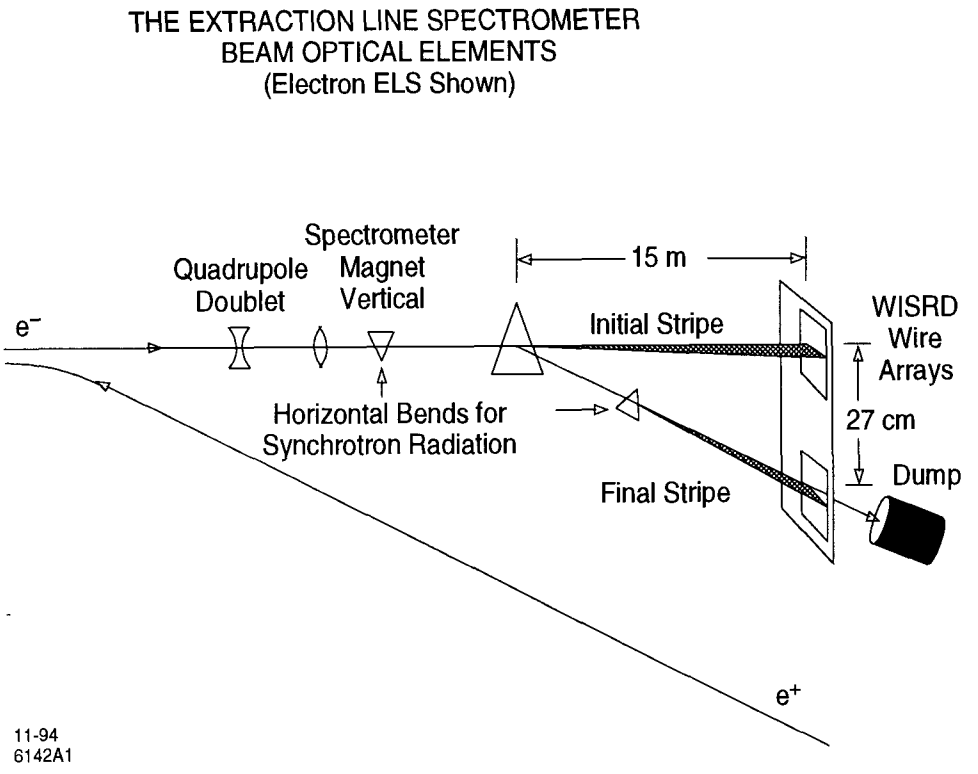

Figure 3.3: A schematic view of the WISRD spectrometer

3.2 The SLC Large Detector

The SLC Large Detector (SLD) is a multi-purpose detector with nearly 4π coverage, designed to study the e^+e^- physics at the Z^0 mass energy scale [28]. A quadrant view of the SLD detector is shown in Fig. 3.4, showing the overall dimensions of the components. The components, starting from center and working outwards, are

- The Vertex Detector
- The Luminosity Monitor
- The Drift Chamber System
- The Cherenkov Ring Imagine Detector
- The Liquid Argon Calorimeter

- The Solenoidal Coil
- The Warm Iron Calorimeter.

Charged-particle tracking is conducted by a CCD-based vertex detector (VXD) and a central drift chamber (CDC), along with a set of endcap drift chambers (EDC) covering the forward and backward regions. The magnetic solenoid uses a conventional aluminum coil to produce a 0.6 Tesla field, which causes the charged tracks to bend in the tracking system and allows their momentum to be measured. The energy of particles are measured by three calorimeters: a Liquid Argon Calorimeter (LAC), measuring both electromagnetic and hadronic energy; a Warm Iron Calorimeter (WIC), measuring the residual hadronic energy which has leaked out of the LAC and tracking the escaping muons; and a Luminosity Monitor (LUM), measuring the energies deposited in the extreme forward and backward directions. Charged particle identification is provided by a Cherenkov Ring Imaging Detector (CRID). Each of these detector components will be described briefly in the following sections. Special attention will be focused on the CDC, since it is the most relevant subsystem for this analysis.

3.2.1 The Vertex Detector

The closest detector component to the beam-pipe is the vertex detector (VXD) [29], as shown in Fig. 3.5. The VXD uses silicon chips called Charged-Coupled Devices (CCDs) as the medium for detecting the deposition of ionization from through-going charged particles. Each CCD is approximately 1 cm^2 in size and contains 375×578 pixels; and each pixel is $22\mu m^2$ in size, yielding an intrinsic resolution of $\sim 3.5\mu m$ in two dimensions [29].

The VXD is constructed of 480 such CCDs, mounted on 60 ladders each of which is 9.2 cm long. The CCDs are arranged in an overlapping fashion into four layers of concentric 8-CCD ladder elements, so that the tracks passing through the VXD will acquire at least two hits. An end view of the VXD is shown in Fig. 3.6. Some tracks can hit more than two CCD's, the average number of VXD hits per track is 2.3. The

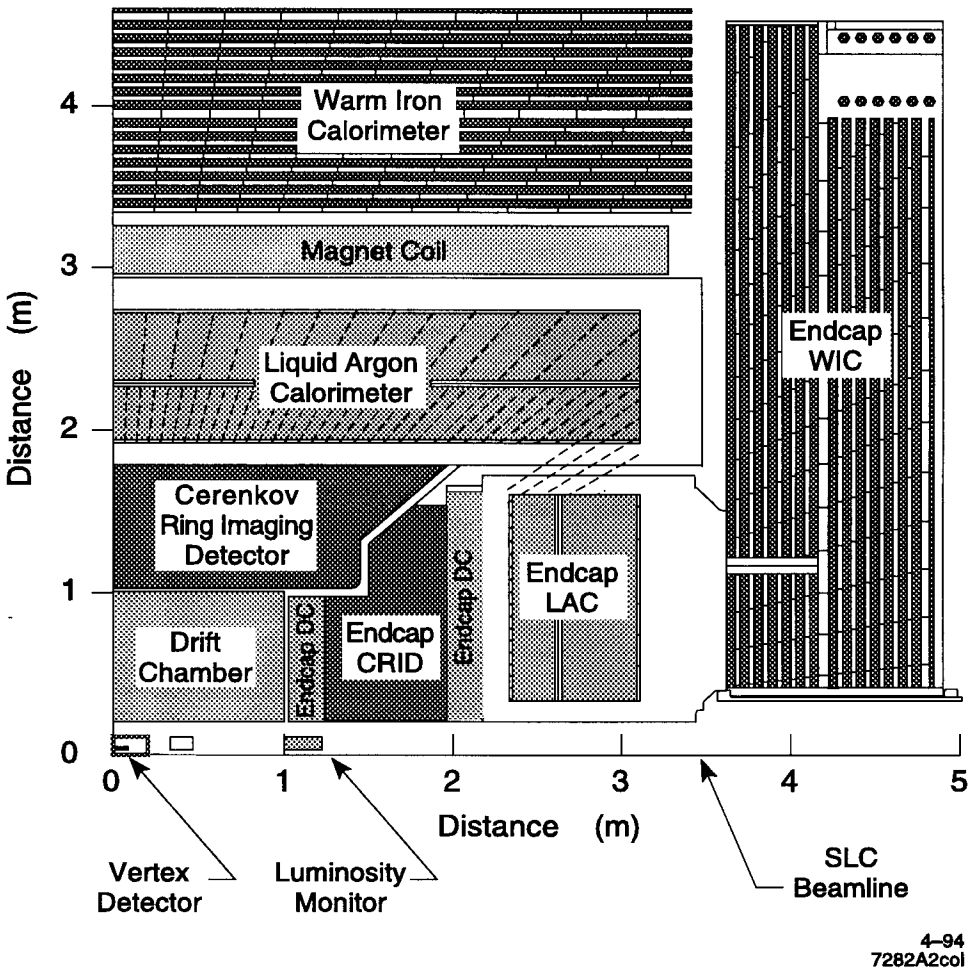

Figure 3.4: A quadrant view of the SLD.

beam-pipe has a radius of 2.55 cm; the first VXD layer is at a radius of 2.95 cm and last layer is at 4.15 cm.

The VXD is a powerful device for distinguishing secondary vertex tracks, produced by the decay in flight of heavy flavor hadrons, from tracks produced at the primary event vertex. In addition, by combining the VXD with the CDC tracking, the overall momentum measurement is improved, yielding a momentum resolution

$$\sigma(p_t)/p_t^2 = \sqrt{0.0026^2 + (0.0095/p_t)^2}, \tag{3.2}$$

where p_t is the momentum of the particle perpendicular to the beam, measured in GeV/c.

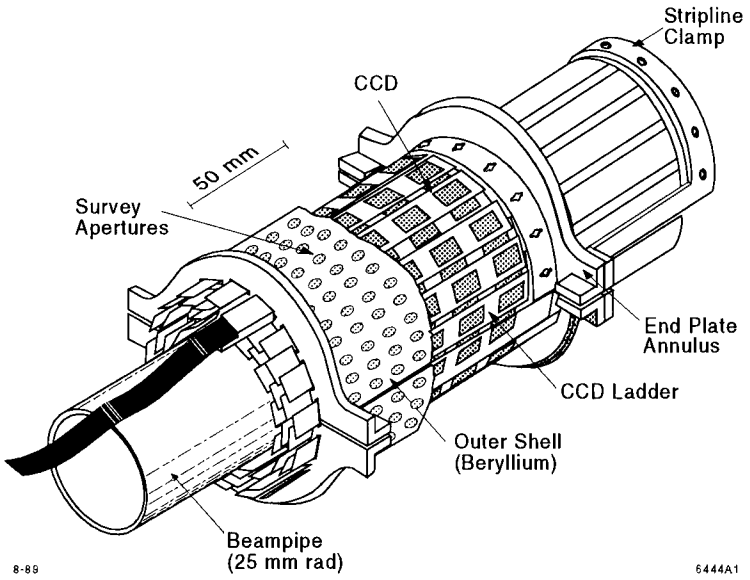

Figure 3.5: The SLD vertex detector.

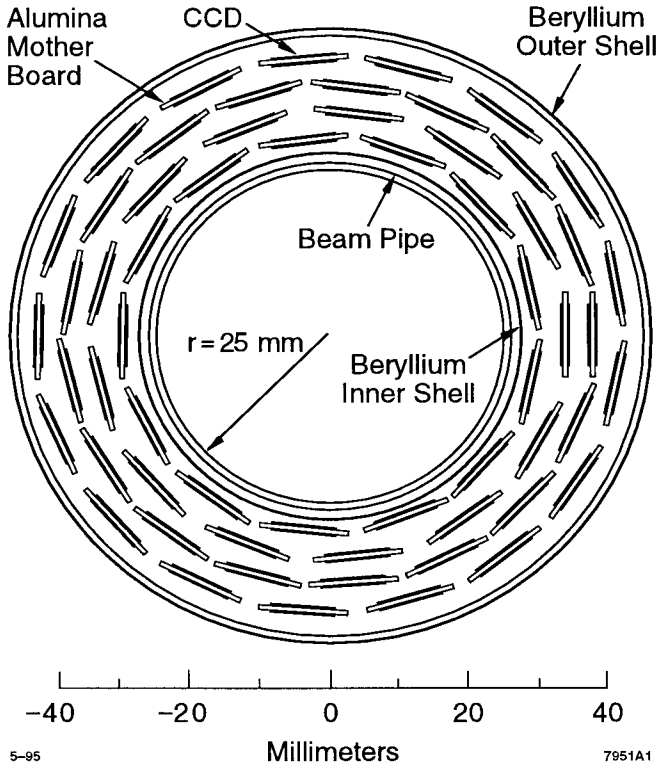

Figure 3.6: An end view of the VXD

3.2.2 The Luminosity Monitor

The Luminosity Monitor and Small-Angle Tagger (LMSAT) and Medium-Angle Silicon Calorimeter (MASC) are designed to determine the integrated luminosity delivered to SLD [33] by measuring the rate of small angle Bhabha scattering ($e^+e^- \rightarrow e^+e^-$). The cross section for this process is well known as $d\sigma/d\theta \sim 1/\theta^3$, and is essentially free from interference with Z^0 for $\theta \leq 50$ mrad.

A side view of the LMSAT/MASC assembly is shown in Fig. 3.7. The LMSAT is located approximately 1 meter from the SLD interaction point (one on each side) and covers the angular region between 28-68 mrad, while the MASC is about 31 cm from the interaction point and covers the 68-190 mrad region. Both are silicon-tungsten sampling calorimeters which are finely segmented as shown in Fig. 3.8. The LMSAT employs 23 layers of $0.86X_0$ sampling, while the MASC has 10 layers of $1.74X_0$ sampling. The energy resolution has been measured to essentially agree with the design of 3% at 50 GeV [35]. The LMSAT was built at the University of Oregon.

3.2.3 The Drift Chamber System

Central Drift Chamber

The central drift chamber (CDC) is a cylindrical annulus with a length of 2.0 m, an inner radius of 0.2 m and an outer radius of 1.0 m. As shown in Fig. 3.9, the chamber contains 80 layers of sense wires arranged in 10 superlayers of 8 sense wires each. Six of the superlayers have a 41-mrad stereo angle with respect to the beam axis to allow a measurement of the z position of the track hit.

Each superlayer is made of independent cells approximately 6 cm wide by 5 cm high. Figure 3.10 shows the detail of one such cell. The field-shaping wires and the guard wires are made of 150 μm gold-coated aluminum, while the sense wires are 25 μm gold-coated tungsten. Eight senses wires are aligned radially. The voltage of each guard wire is set to be about 3 kV, while a set of high voltages are provided on the field wires with the mean value around 5.3 kV.

The gas filling the chamber is chosen to be a mixture with 75% CO_2, 21% Argon, 4% Isobutane, and 0.2% H_2O to provide the most precise measurement of the drift

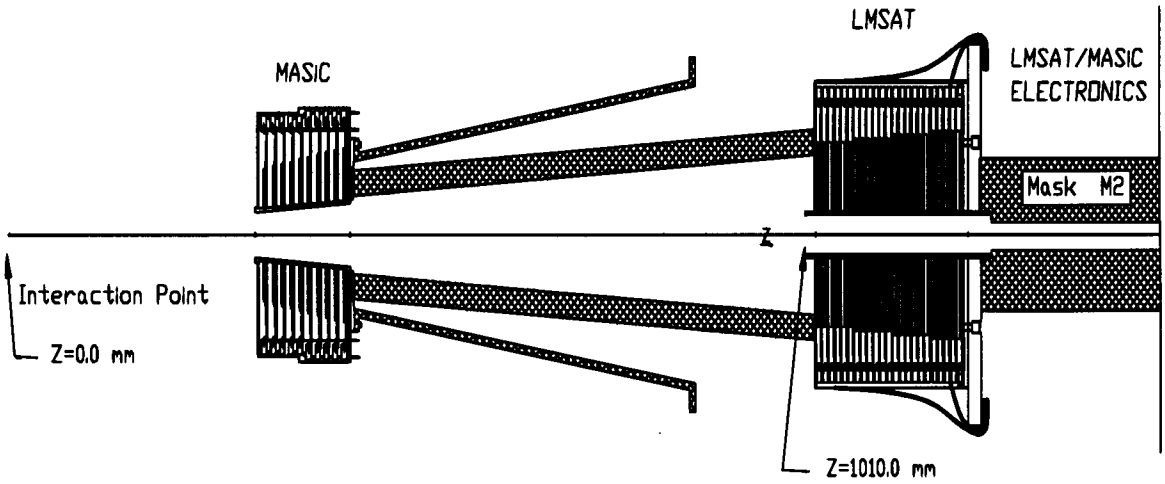

Figure 1. Luminosity Monitors for SLD

Figure 3.7: A side view of the LMSAT/MASC assembly.

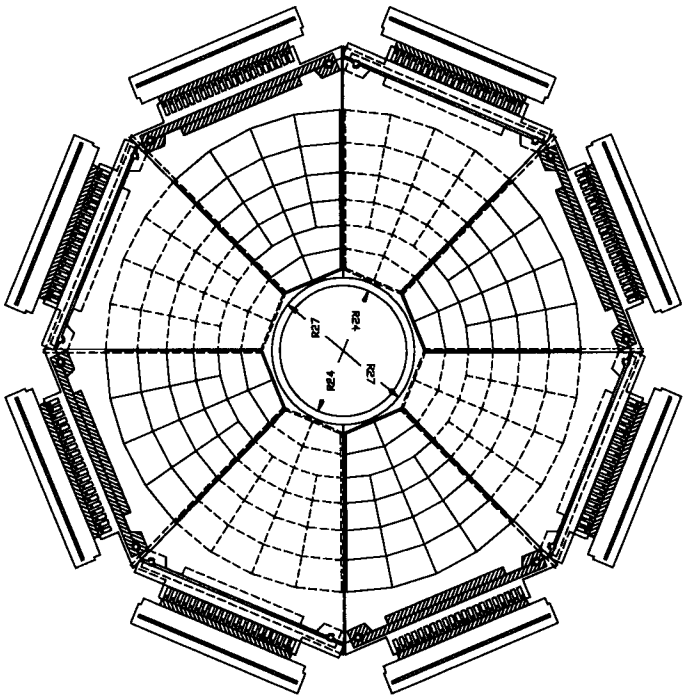

Figure 3.8: A face view of the LMSAT showing the segmentation.

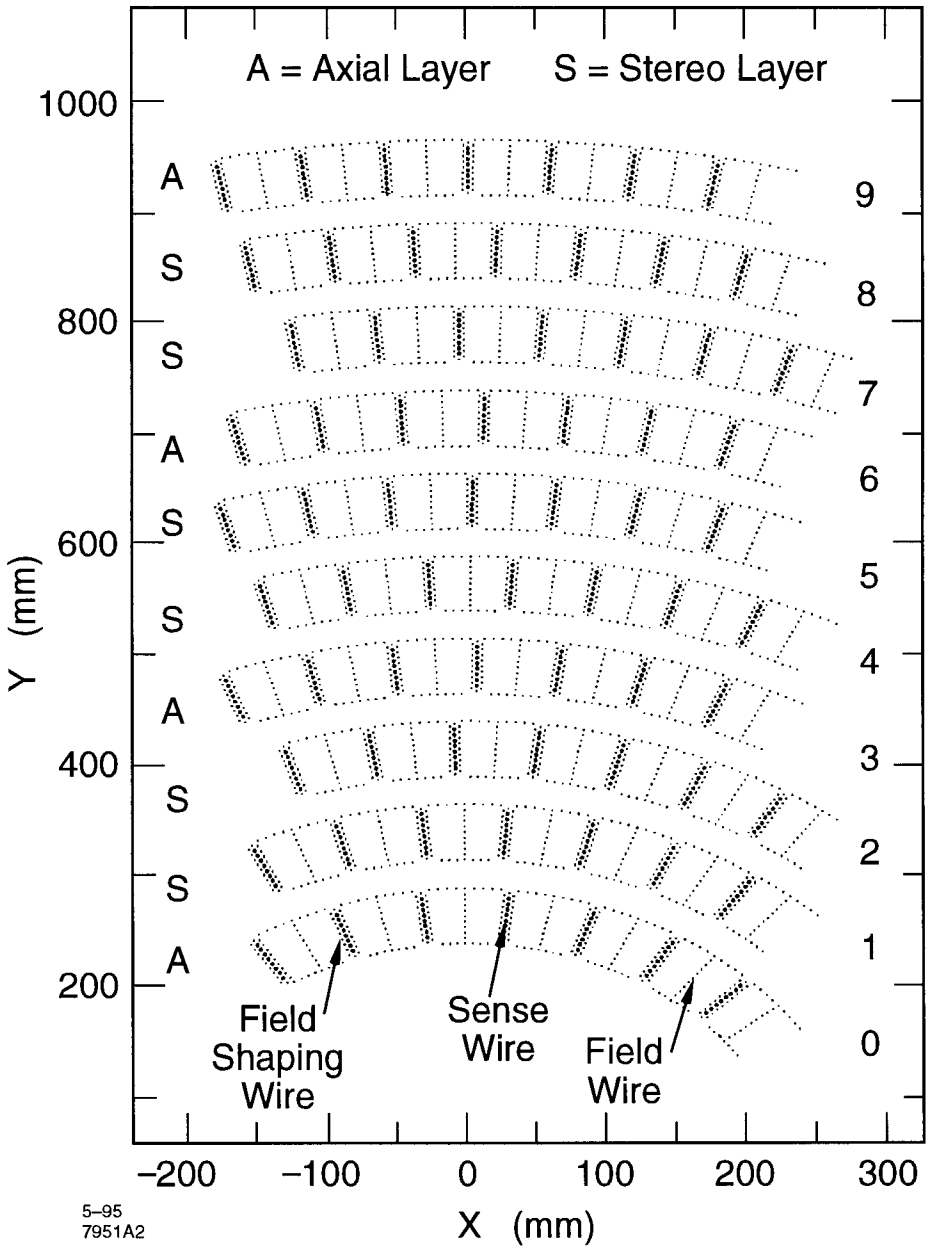

Figure 3.9: A section of the CDC. Axial layers are labeled 'A' (parallel to the beam axis), while the stereo layers are labeled 'S' (with ± 41 mrad alternately).

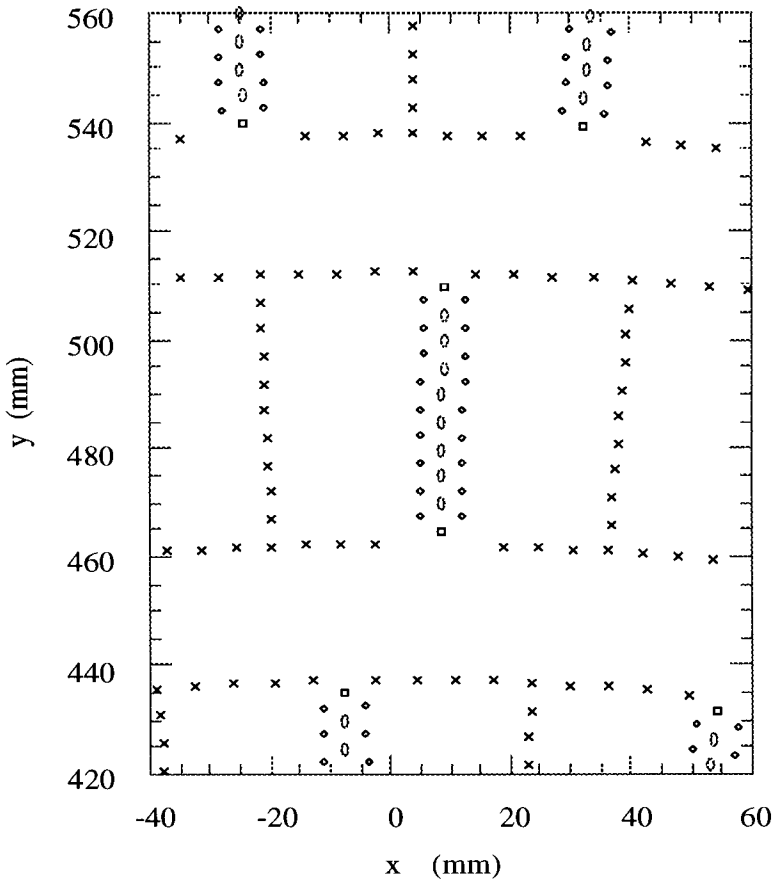

Figure 3.10: The schematics of a single cell, showing the layout of the sense wire (○), guard wires (◇) and field wires (×).

distance [30]. As the primary component, CO_2 has the properties of low drift velocity and low diffusion constant. The former property allows for a finer sampling of the signal for a fixed electronics speed; the latter reduces the contribution of diffusion to the resolution. For such mixed gas, the drift velocity is about 9 μm/ns on average.

The CDC readout electronics [31] were designed to operate in the 120 Hz SLC beam cycle. At each beam crossing, the electrical pulses on the sense wires are sampled on both ends at 119 MHz and stored onto Hybrid Analog Memory Units (HAMUs), and digitized for the trigged events. The double-ended readout allows a charge division measurement of the z position of the track hit, which aids track finding.

The CDC is installed inside the solenoidal magnet which provides a uniform 0.6 T field along the beam axis to allow the measurement of particle momentum.

Drift Model and T2D

A charged particle traversing the cell ionizes the gas atoms, and the liberated electrons will drift toward the sense wires under the electric field. Such a drift process is simulated in a model, yielding a drift time to drift distance relationship, known as the T2D relation. From the measured time between a beam crossing and the arrival of the signal on the sense wire, one can thus determine the distance of a hit from the sense wire via T2D relation.

The electric field at every point of a cell can be calculated from wire configuration (see Fig. 3.10) and corresponding voltage setup as

$$\vec{E} = \sum_i \frac{Q_i}{r_i^3}\vec{r}_i, \qquad Q_i = \sum_{i \neq j} C_{ij} V_j. \tag{3.3}$$

where C_{ij} is the capacitance between wire i and j, and V_j is the voltage on wire j. With such a wire configuration and voltage setup, a cell ends up with two distinctive regions: a drift region with a nearly uniform field between the field wires and guard wires, and a nonlinear region between the guard wires and sense wires. The liberated electrons drift toward the sense wires with a constant velocity in the drift region. Near the sense wires (nonlinear region) the electrons in the high gradient field undergo amplification via the avalanche mechanism. The mean drift field is about 0.9 kV/cm,

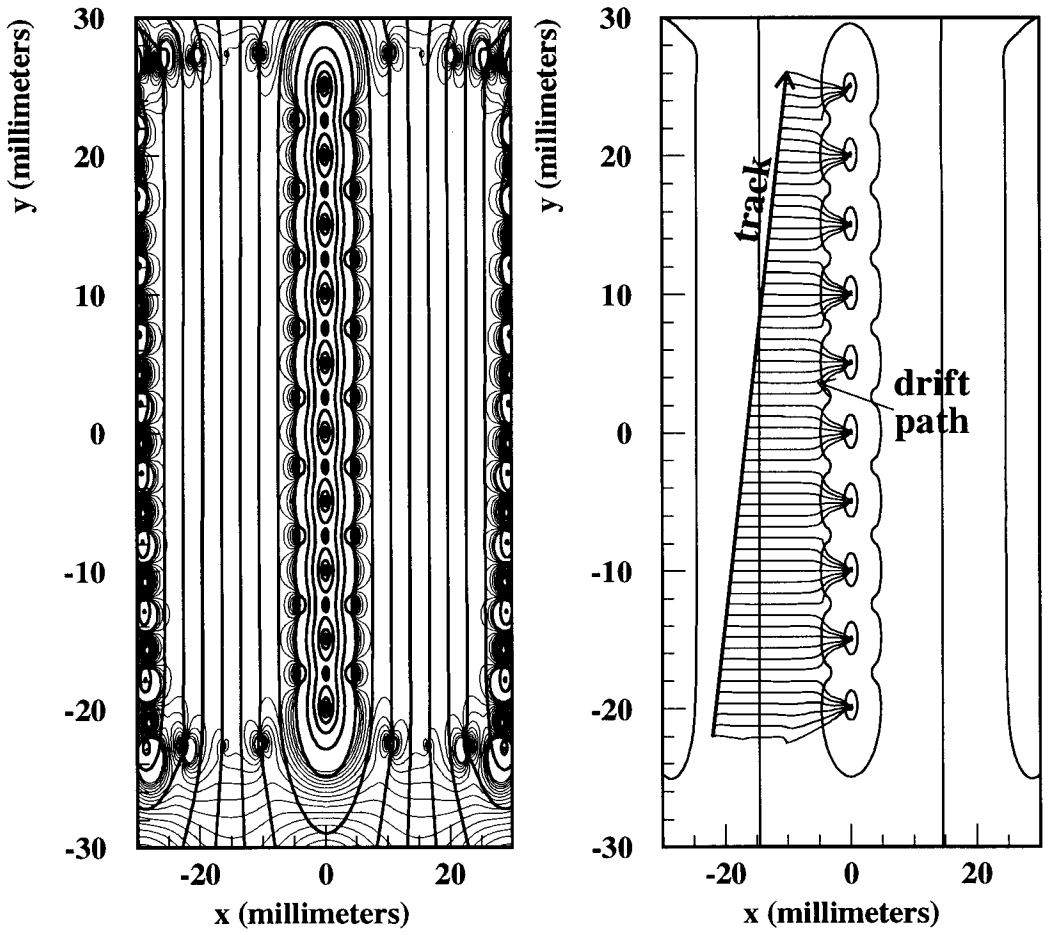

Figure 3.11: The left figure shows equipotential lines (bold) and lines of constant field strength (thin). The right figure shows the drift paths of electrons in the field.

but the field near a sense wire rises to over 40 kV/cm. A field map in a cell and a schematic of simulated drift paths are shown in Fig. 3.11. For a given distance from the sense wire, a number of points are applied to slice it into segments: more points are required in the non-linear region than in the drift region where the drift velocity is constant. The drift time is found by integrating up the time intervals for each drift segment, thus forming a time to distance relation (T2D). A T2D relation is displayed

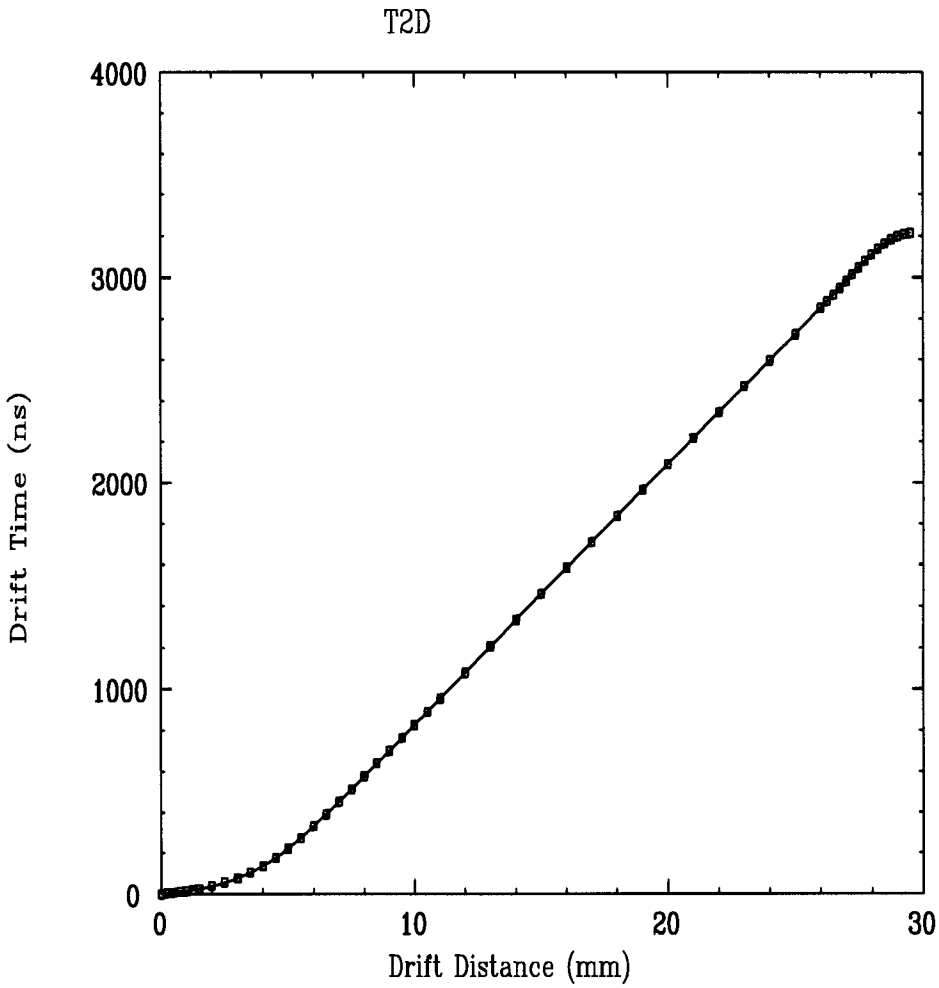

Figure 3.12: T2D relation. Points to segment the path is indicated by mark ◇. Values between the points can be obtained by interpolation.

in Fig. 3.12. It should be noted that the above T2D is constructed assuming that the track crosses the cell parallel to the sense wire plane. For a track with a certain angle, we applied an angular correction based on a simple parameterization. We also performed the corrections for cases such in which the high voltage is off for a layer. The average residual (the distance between the measured hit position and the fitted track) can be further used as a correction to the drift distance [32].

Track Reconstruction

Track reconstruction is accomplished via four steps in SLD. The first of these steps is to find the raw hits. The double-ended readout enables the z position of each hit along the sense wire to be estimated by calculating the asymmetry of the charge division of the pulses, while the drift time information can be used to determine the distance of the hit from the sense wire via the T2D. Certain thresholds were set to discriminate the noise from the signal pulse.

The second step is to use hits within a cell to form into track segments, usually called vector hits (VH). There must be at least three hits present in a cell to form a track segment. The track segment is characterized by a space point $\vec{x}$ and a two dimensional direction $\vec{t}$ in the $x-y$ plane. The hit positions are then corrected for the effects of the relative angle between the track segment and the sense wire plane through the T2D as mentioned above.

The third step is to link these track segments together, a process also called pattern recognition. The linking algorithm operates in the $x-y$ plane, as shown in Fig. 3.13. If two track segments belong to the same track then they must have equal (but opposite-signed) angles with respect to the vector joining the spatial coordinates of the track segments. Initially, the combination of VHs on axial layers are formed by fitting them into circles. The VHs from stereo layers are then added if they fit on these circles. The z information from the charge division measurement is used to project the stereo VHs onto the circles. In the first instance, only tracks with 10 VHs are considered, and the one with the best χ^2 is taken as a candidate track. Its VHs are removed from further consideration, and the process is repeated until all tracks of at least three VHs are found.

The last step is to process all track candidates by an iterative track fitter. The fitter starts with the estimated track parameters from the pattern recognition. It then swims a helical trajectory through the detector material, taking into account the variation of the magnetic field, energy loss and multiple scattering. The fitter uses the individual hits of the candidate tracks, and may add or delete hits as the iterations proceed. Finally, a best set of helix parameters describing the track is obtained.

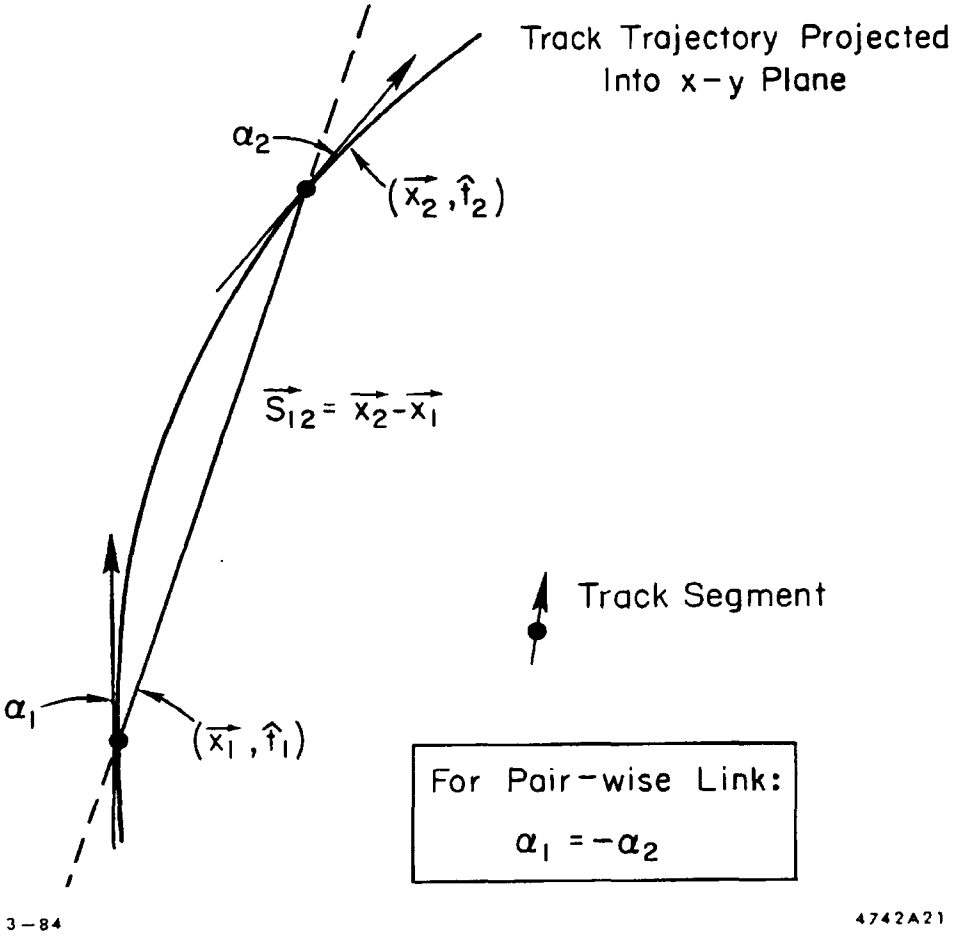

Figure 3.13: A scheme for linking track segments.

Performance

A track passing through all CDC layers is ideally expected to have a hit in each wire layer, thus making 80 hits in total. Shown in Fig. 3.14 is the distribution of the number of hits found on a track with a comparison to MC. Fig. 3.15 shows the hit-finding efficiency as a function of wire layer, where layer 0 is the innermost layer. The lower efficiency on the inner layers is attributed to the finite two-hit resolution as the tracks become closer, and the higher backgrounds in this region. Fig. 3.16 shows the drift distance resolution measured as a function of the drift distance. We distinguish between local and global resolution. The local resolution is determined

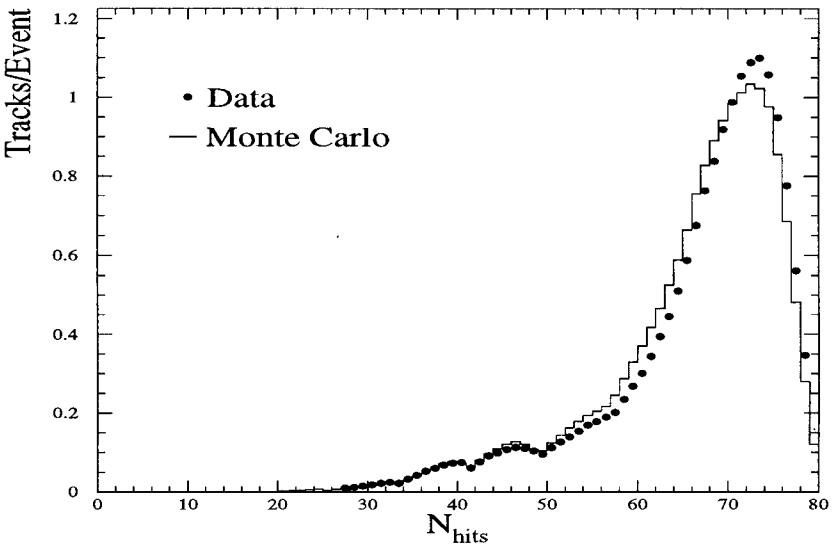

Figure 3.14: Distribution of number of hits on track.

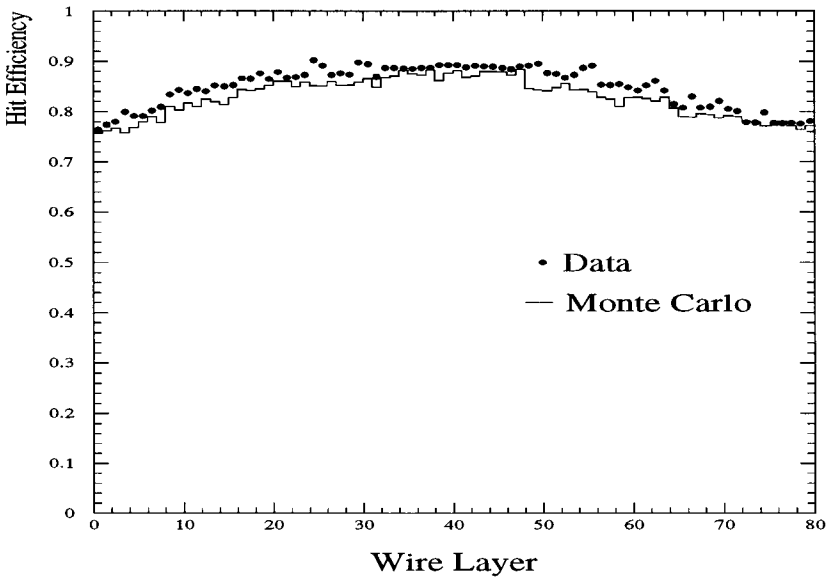

Figure 3.15: Hit-finding efficiency as a function of wire layer.

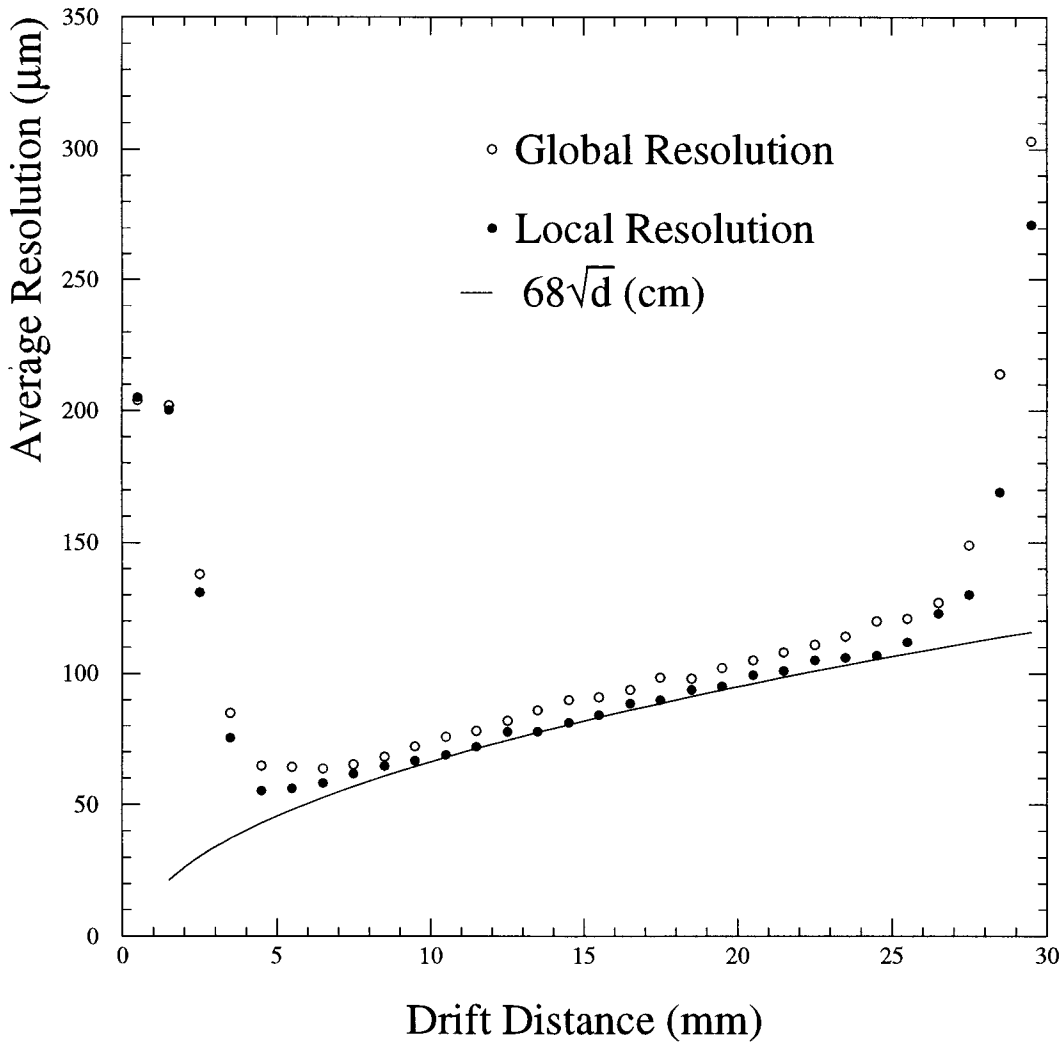

Figure 3.16: Drift distance resolution in CDC measured as a function of the drift distance.

from the width of the distribution of the residuals to the vector hits in each cell, while the global resolution from the width of the distribution of the residuals to the fitted track. In the region of linear field the resolution follows the curve expected from diffusion (68μm at 1 cm and varying as $\sqrt{d}$). As it is seen, the spatial resolution has a strong dependence on the distance to the sense wire. Note the degradation of the resolution in the regions near the sense wire and field wires. This is mainly due to the increasing drift velocity and non-uniformity of the drift fields in these regions.

3.2.4 The Cherenkov Ring Imaging Detector

Identification of charged particle types is accomplished with the Cherenkov Ring Imaging Detector (CRID) [36]. When a charged particle passes through a material at relativistic speed, it produces a cone of Cherenkov light, whose opening angle w.r.t the incident particle is inversely proportional to the velocity: $\cos(\theta_c) = 1/\beta n$, n is the refraction index of the material and β the velocity of the particle. Using this principle, the CRID is able to measure the velocity of a charged particle. By combining the velocity with the momentum measured in the tracking detectors, one can calculate the mass of the particle, and thus determine the type of charged particle.

The CRID in SLD is designed to identify charged particles over a large range of momentum and mass through the combined use of liquid C_6F_{14} and gaseous C_5F_{12} radiators. Charged particles above Cherenkov threshold passing through the radiators emit photons, which are imaged through quartz windows into time projection chambers (TPCs) containing a photosensitive gas. The resulting photoelectrons drift to wire chambers where the conversion point of each is measured in three dimensions using drift time, wire address and charge division. These positions are used to reconstruct a Cherenkov angle with respect to each extrapolated charged track. A schematic view of the principle of the CRID operation is shown in Fig. 3.17.

3.2.5 The Liquid Argon Calorimeter

The measurement of the energy of particles is provided by the Liquid Argon Calorimeter (LAC). The LAC is a sampling calorimeter which is made of stacks of lead tiles

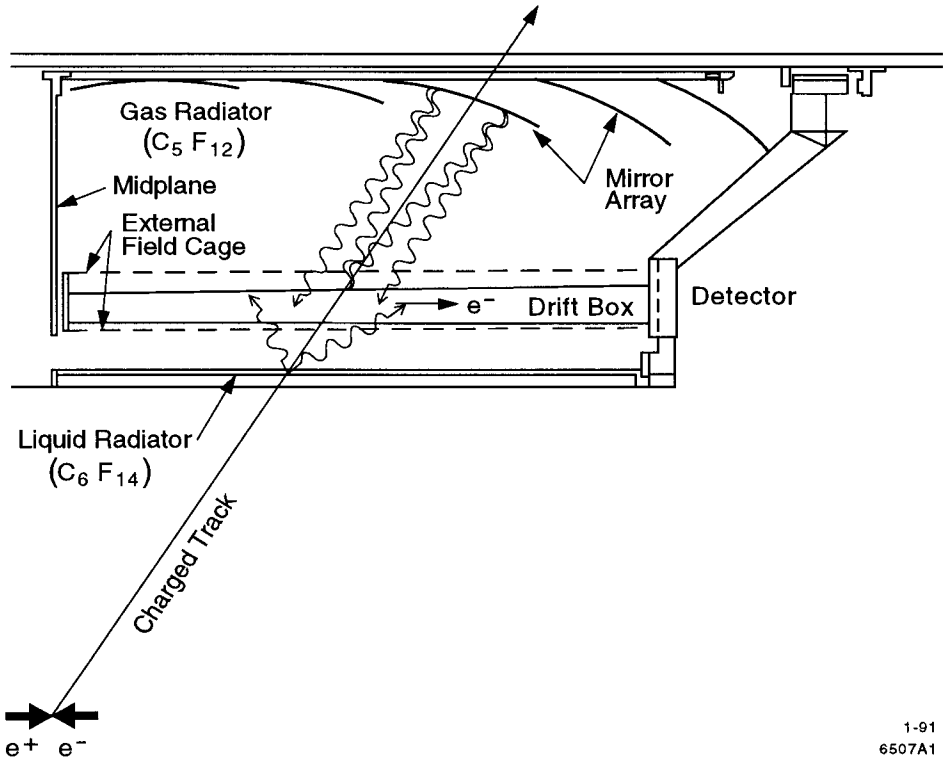

Figure 3.17: A schematic view of the principle of the CRID operation. Charged particles create Cherenkov light in liquid C_6F_{14} radiator or gaseous C_5F_{12} radiator. Cerenkov light is detected in the drift box when it frees single electrons, which then drift to the wire chamber. The endcap CRID operates in a similar way.

immersed in a bath of liquid argon. The tiles are alternately at ground potential and at negative high voltage, and the stacks of tiles are aligned to form projective towers pointing back to the IP. Shown in Fig. 3.18 is the basic structure of the LAC. Particles that interact with the lead produce a shower of lower-energy secondary particles which ionize the argon. The charges liberated from ionization are then collected by the tiles. Since argon supplies no charge amplification, the charge collected is thus proportional to the energy deposited by particles.

To be able to measure the energies of different particles, the LAC is divided into two sections: an electromagnetic section (EM), which is thin and designed to measure electrons and photon energies, and a hadronic section (HAD), which is deeper

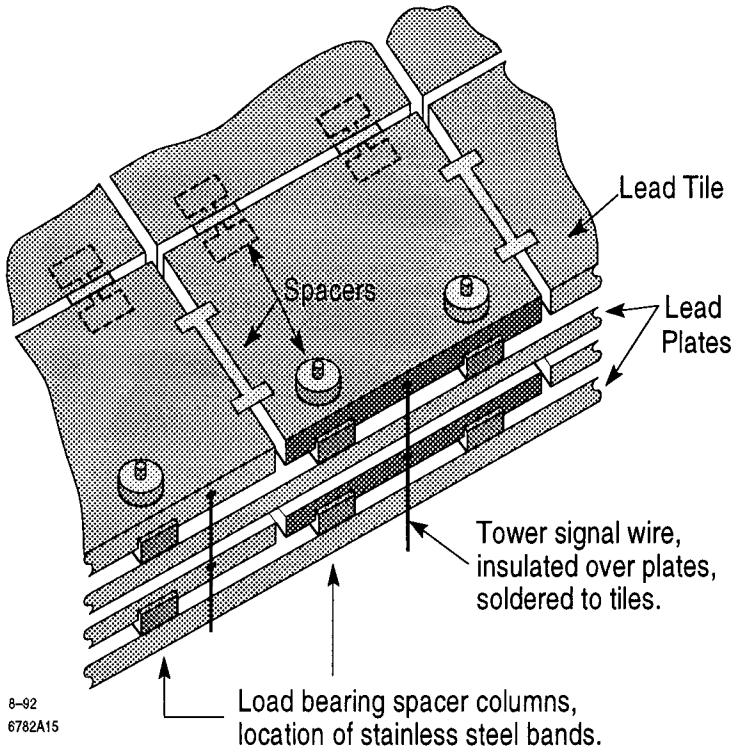

Figure 3.18: The basic structure of the LAC.

and designed to measure hadron energies. Each section is subdivided into two layers: EM1 and EM2, HAD1 and HAD2. The energy resolution for the LAC has been measured to be $12\%/\sqrt{E}$ and $65\%/\sqrt{E}$ for the EM and HAD sections [34], respectively. Approximately 95% of the energy in a hadronic Z^0 decay can be measured by the LAC. The WIC is expected to measure the remaining 5%, acting as a tail-catching calorimeter as described below. The LAC endcaps are a continuation of the barrel in the forward and backward direction with a similar structure.

3.2.6 The Solenoidal Coil

Surrounding the LAC is the SLD magnet, a cylindrical aluminum coil of 5.9 m diameter, 6.4 m long and 29 cm thick. A current of 6600 A through 508 turns provides a magnetic field of 0.6 Tesla inside the coil. The iron structure of the WIC in the

barrel and endcap described below serve as the flux return path. The lowest order polynomial approximation to the field can be written as

$$B_r = B_r^0 \frac{rz}{r_0 z_0}, \qquad B_z = B_z^0 + 0.5 B_r^0 (\frac{r^2 - 2z^2}{r_0 z_0}). \tag{3.4}$$

where $B_r^0 = 0.0214T$, $B_z^0 = 0.601T$, $r_0 = 1.2$ m and $z_0 = 1.5$m.This agrees with the measured field to within 0.05% inside the volume of the CDC. The field has been mapped to be uniform to 3% over the tracking volume of the CDC to ensure the accurate measurement of the momenta of charged tracks; the lowest order polynomial expansion to the non-axial field in a finite solenoid is used during track reconstruction to parameterize the field non-uniformity.

3.2.7 The Warm Iron Calorimeter

The Warm Iron Calorimeter (WIC) basically serves three functions within the SLD: muon tracking, a tail-catcher of the leakage of the hadronic showers from LAC and a magnetic flux return [37].

The WIC is the outer structure of the SLD, and is 4 interactions length thick. Sixteen layers of plastic streamer tubes (Iarocci tubes) interleaved with 2 inch thick plates of absorber provide muon hit resolutions of 0.4 cm and 2.0 cm in the azimuthal and axial directions respectively. The WIC structure is shown in Fig. 3.19. Placed on one side of each Iarroci tube are square pads for calorimeter readout, and on the other side strips for muon identification. Transverse strips, placed in special double layers, supply coordinate information perpendicular to the Iarroci tubes for muon tracking. The geometry of the pads is a continuation of the hadronic tower structure of the towers in the LAC. The readout is analog, proportional to the energy deposited. The energy resolution is $\sigma(E) \sim 0.8\sqrt{E}(GeV)$. The background of the muon identification comes from pion punch-through. Pattern recognition and tracking capability for individual tracks can extrapolate the particles back to the drift chamber, and thus is able to remove this background significantly.

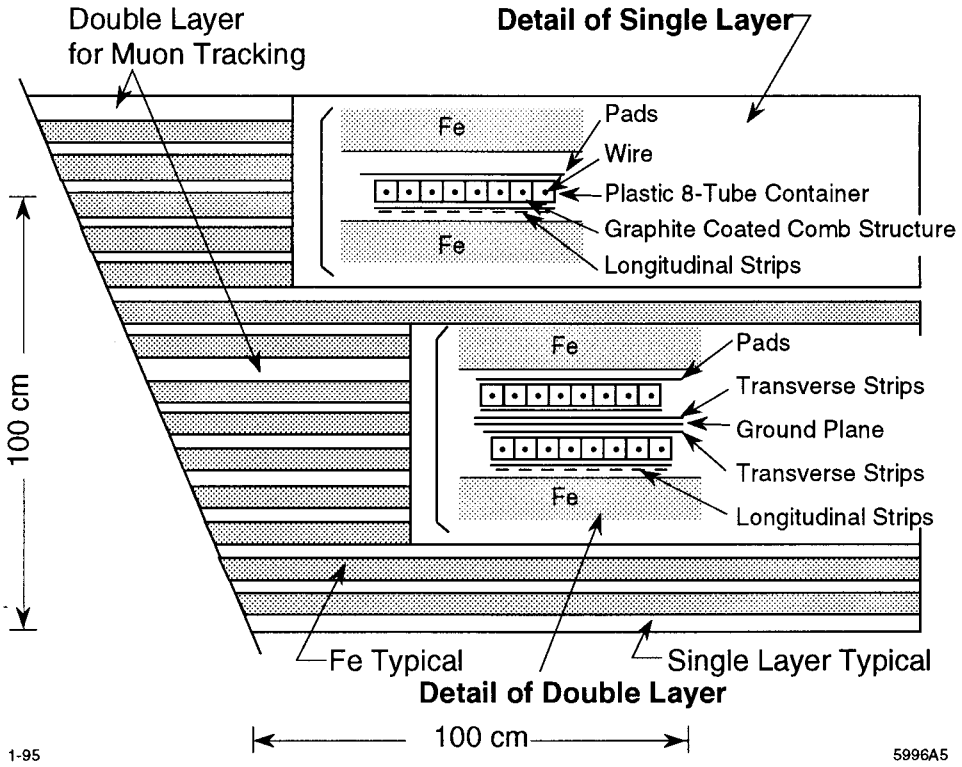

Figure 3.19: The WIC schematics.

3.3 The SLD Monte Carlo Simulation

To be able to interpret measurements one has to use models to simulate the physics process and also the detector performance. SLD uses the JETSET 6.3 event generator [75] to simulate the process of $e^+e^- \rightarrow$ hadrons at the Z^0 resonance. The simulation of detector performance is based on the GEANT3 package [39] developed at CERN.

3.3.1 Event Generator

The JETSET event generator always includes all four phases in the process of $e^+e^- \rightarrow$ hadrons as described in Chapter 2. There are a large variety of options provided by JETSET for simulating these phases. JETSET 6.3 uses the parton shower model to account for the parton evolution, and string fragmentation for the hadronization. Listed in Table 3.1 are a few major parameters with both default and optimized values,

as determined by thhe SLD QCD analysis group. Λ_{QCD} is the QCD scale parameter

Parameter	Default	Optimized
Λ_{QCD}	0.40 GeV	0.29 GeV
Q_0	1.0 GeV	1.0 GeV
σ_q	0.35 GeV	0.37 GeV
a	0.50	0.18
b	0.90 GeV^{-2}	0.34 GeV^{-2}

Table 3.1: Major parameters in JETSET 6.3.

which determines the boundary between non-perturbative and perturbative energy ranges. Q_0 is a cutoff parameter (normally $Q_0 = O(1GeV)$, corresponding to an effective gluon mass) which determines the termination of parton showering. The three other parameters σ_q, a and b belong to the hadronization process, controlling the transverse and longitudinal momentum spectrum of hadrons. These parameters were optimized to reproduce the experimental distributions of single particle and event topology observables at the Z^0 resonance.

3.3.2 Detector Simulation

The SLD detector simulation is performed by the package GEANT, providing the detector response to the particles produced by the event generator. The SLD detector is a collection of different kinds of particle detectors, each with its own particular way of responding to a particle and producing a signal. Also, there is much material in SLD for mechanical support, electronic cables, gas and liquid plumbing systems, etc., and particles will interact with and be affected by these materials as well. Basically, the simulation includes the effects such as energy loss, particle decays, Bremsstrahlung, Compton scattering, multiple scattering, delta-ray production, gamma conversions, and nuclear and electromagnetic interactions. Other effects such as readout electronics that were not properly operational (e.g. dead channels) during a certain part of the run, and high voltages off for some superlayers in CDC were simulated as well,

so that the time-dependent configuration of the simulated detector matches that of the real SLD over the course of the run. In addition, the beam backgrounds that arise in the various detector elements were considered in the simulation by overlaying the background noise (measured at the random trigger during beam crossings where a collision occurred), on top of the MC hadronic events. Finally, these fully simulated MC events were reconstructed using the same process, and written in the same format, as real data.

The MC event sample plays an important role in determining the detector efficiency and spatial acceptance. Besides hadronic MC samples, some other MC samples such as WAB's and $\tau^+\tau^-$ were produced to account for different physics processes, and also used to estimate the background contaminations and study the tracking efficiency. These issues will be covered in the later chapters.

Chapter 4

Hadronic Event Selection

The SLD started its physics data collection in 1992, and has been recording data smoothly ever since. The analyses presented in this thesis are based on the data collected during the period of 1993-1995. Data were taken under highly variable beam conditions. An online trigger and an offline filter were therefore applied to filter out Z^0 events from the backgrounds. For the interests of testing QCD, a set of cuts were further applied to select the hadronic events. In the following sections we will describe in some detail the processes that led to the hadronic event sample suitable for QCD studies.

4.1 The SLD Trigger

The SLD trigger is designed to record Z^0 events with a high efficiency, while rejecting most of the background processes such as beam-gas, beam-wall interactions, cosmic rays and synchrotron radiation. The following different triggers were applied to select the events to be written to tape. The trigger algorithms are described in details in Ref. [40].

- The Energy trigger required a minimum total of energy 8 GeV deposited in the barrel and endcap LAC, where the sum is made only over those towers above the thresholds (60 ADC counts in EM section and 120 ADC counts in HAD section). ADC counts convert to MeV as follows: for EM towers 1 ADC = 4.1

MeV, for HAD towers 1 ADC = 10.8 MeV. Only the calorimeter systems were read out when this trigger fired only.

- The Tracking trigger was activated when two (or more) CDC tracks were detected. A CDC track is defined to have at least 6 hits in each cell of 9 or more superlayers in the CDC, with an opening angle $> 30^0$ and momentum greater than 250 MeV/c. All SLD subsystems were read out if this trigger fired.

- The HAD trigger was activated if the energy trigger was satisfied plus at least one CDC track was detected. Most Z^0 events would satisfy this trigger. All SLD subsystems were read out if this trigger fired.

- The WAB trigger required a minimum total energy of 15 GeV deposited in the LAC EM section, where the sum is made over those towers above the threshold (154 MeV). All SLD subsystems were read out if this trigger fired. This trigger was designed to insure that all wide-angle Bhabha events ($Z^0 \rightarrow e^+e^-$) were recorded.

- The Muon trigger required a combination of at least one CDC track and two back-to-back barrel WIC tracks. All SLD subsystems were read out if this trigger fired. This trigger was designed to select $Z^0 \rightarrow \mu^+\mu^-$.

- The LUM trigger required a total energy in LUM EM2 section to be above 12.5 GeV in both north and south detectors, where the sum is made over those towers above the threshold (125 MeV). Only the LUM/MASIC systems were read out when this trigger fired.

- The Random trigger was activated at a fixed average rate of 1/20 Hz when beams were colliding. The events recorded are used for background studies.

The trigger rate was typically between 0.5-2 Hz, depending on the beam conditions. It should be pointed out that the energy thresholds were changed several times, and the values quoted above were used during most of the data taking. The events which passed any of these triggers were written onto tape called the 'RAW tape'.

4.2 Event Filtering

To further remove backgrounds and make an initial hadronic event selection, a process called the Pass 1 Filter is run on all raw data. Only the LAC information is used in this filter since it is much easier and faster to process than the tracking data. The filter is designed to be quick and efficient, basically requiring that an event deposits a small amount of energy in the LAC and that it has good forward-backward momentum balance. The following three LAC quantities are used to define the filter [40]:

- EHI, a high-threshold energy sum, which is the sum of energy deposited in all EM towers with signals above 60 ADC counts and all HAD towers with signals above 120 ADC counts
- ELO, a low-threshold energy sum, which is the sum of energy deposited in all EM towers with signals above 8 ADC counts and all HAD towers with signals above 12 ADC counts
- $NEMHI$, the number of EM towers that have signals above 60 ADC counts.

To pass the filter, the event must satisfy:

1. $NEMHI \geq 10$
2. $EHI > 15$ GeV
3. $ELO < 140$ GeV
4. $2 \times EHI > 3 \times (ELO - 70)$
5. The north and south side of the detector must each have $NEMHI > 0$.

Requirements (1) and (2) are designed to identify the high calorimetric energy of hadronic events; (3) and (5) to remove beam related background; and (4) to remove SLC muon background. The combined efficiency for hadronic Z^0 decays to pass the SLD trigger and Pass 1 Filter is approximately 92% [42]. The events passing this filter were then fully reconstructed and written onto tapes called 'RECON tapes'.

4.3 Hadronic Event Selection

The Pass 1 Filter is designed to be quick and efficient, and is thus quite loose. The filtered samples are very likely contaminated with a fair amount of backgrounds such as tau pairs, WAB's, and so on. This analysis used charged tracks measured in the CDC and VXD. In order to select a sample of hadronic events useful for this physics analysis, we designed a set of cuts to further improve the purity of the sample and to ensure that the tracks were well measured and the events were contained within the fiducial region of the detector.

The well-measured charged tracks were required to have

- a distance of closest approach transverse to the beam axis within 5 cm, and within 10 cm along the axis from the measured interaction point
- a polar angle, θ, with respect to the beam axis within $|\cos(\theta)| < 0.8$
- a momentum transverse to the beam axis greater than 0.15 GeV/c.

Each track is extrapolated back towards the interaction vertex. Figure 4.1a and Fig. 4.1b shows the distributions of the longitudinal impact parameter Z and transverse impact parameter R. The data are compared with the Monte Carlo. Cuts $R < 5$ cm and $|Z| < 10$ cm ensure that the tracks originate from the proximity of the interaction point. The cut values are indicated on the figures by arrows. In this and the following plots, all tracks and events selection cuts have been applied except the one shown. Shown in Fig. 4.2 is the polar angle distribution of the charged tracks with respect to beam axis. The tracking efficiency outside the coverage of the CDC ($|\cos(\theta)| > 0.8$) drops off significantly. Cut $|\cos(\theta)| < 0.8$ is thus chosen to ensure that the tracks are well contained in the active region of the CDC. The p_t cut serves two main purposes: First, most of tracks produced from beam-related background and from photon conversions have very low transverse momentum with respect to the beam; second, tracks with very low p_t can loop back into tracking system so that they may be doubly reconstructed. In addition, low p_t tracks are difficult to model precisely due to multiple scattering. The p_t distribution of the charged tracks is shown in Fig. 4.3. The well-contained hadronic events were then required to have

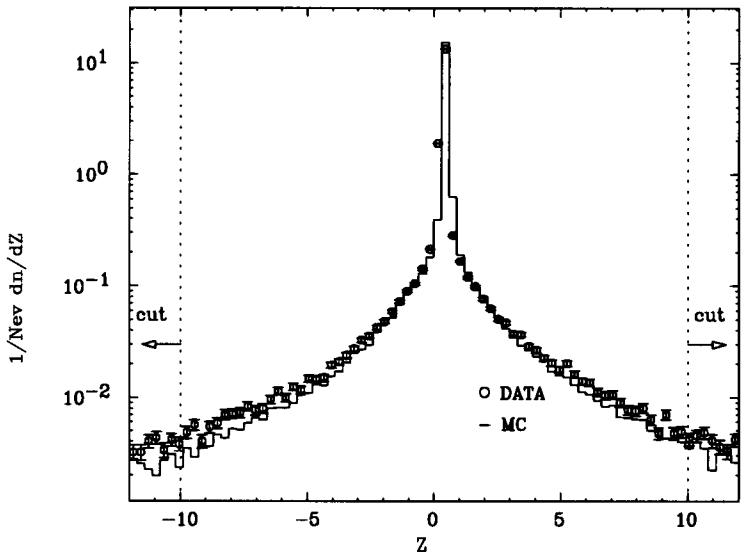

a. The distribution of longitudinal impact parameter Z(cm).

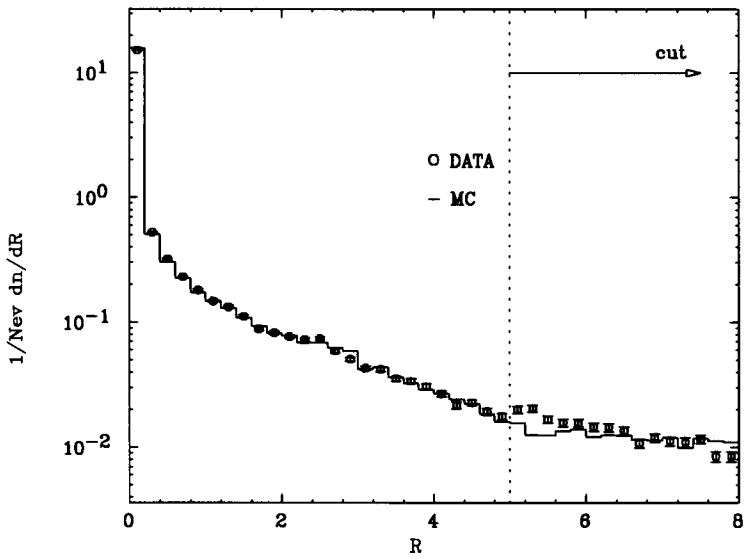

b. The distribution of transverse impact parameter R(cm).

Figure 4.1: Impact parameter distributions

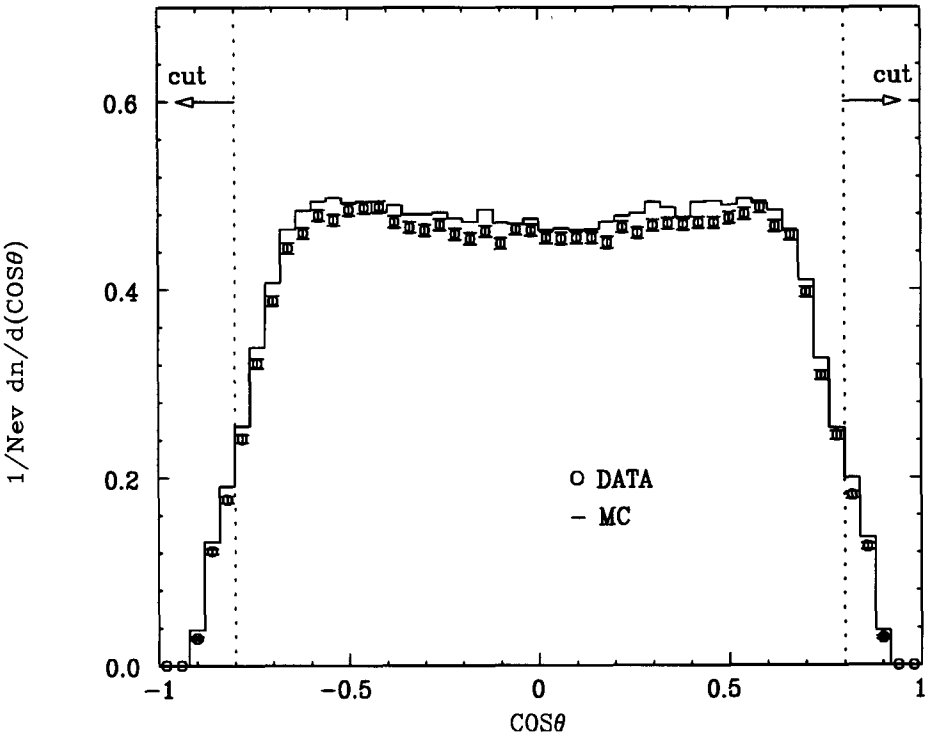

Figure 4.2: Polar angle distribution of the charged tracks, w.r.t beam axis.

- a minimum of five well-measured tracks;
- a total visible energy E_{vis} of at least 20 GeV, which was calculated from well-measured tracks assigned the charged pion mass;
- a thrust axis direction within $|\cos(\theta_T)| < 0.71$ (see definition of thrust below).

The cuts made here are based on the well-measured charged tracks selected above. The charged multiplicity distribution is shown in Fig. 4.4. An excess at low multiplicities is expected mostly from $\tau^+\tau^-$ pairs and Bhabha events. Thus the requirement of a minimum of five tracks is expected to remove these backgrounds significantly. The visible energy distribution is shown in Fig. 4.5. An excess at low energy is apparent. Most of the beam-related backgrounds and two-photon events have low visible energy, as the tracks within the detector acceptance from these processes tend to be very soft. The visible energy cut is thus designed to eliminate these backgrounds.

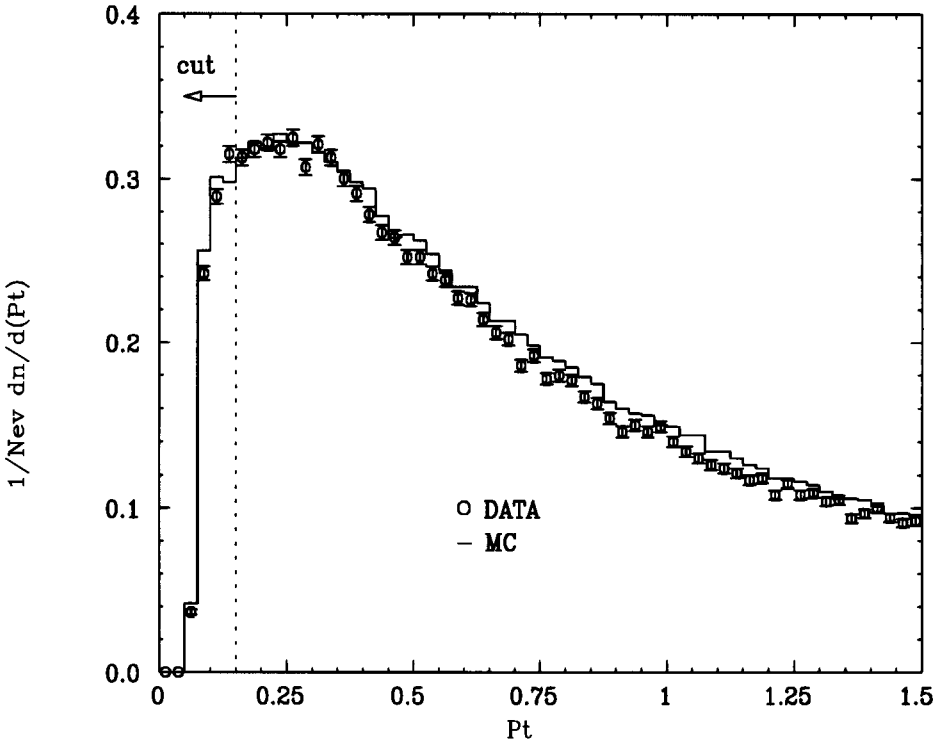

Figure 4.3: The p_t distribution of charged tracks (p_t is defined with respect to the beam axis).

Figure 4.6 shows the polar angle distribution of event thrust axis. Thrust T is defined as

$$T = \max\left(\frac{\sum_i |\vec{p_i} \cdot \hat{n}|}{\sum_i |\vec{p_i}|}\right), \tag{4.1}$$

where i runs over all tracks, and the thrust axis $\hat{n}$ is chosen to maximize the value of T. The event shape variables such as T will be described in detail in later chapters. Events with thrust axis close to the beam direction are not well reconstructed due to the decreasing efficiency of the CDC in the forward region. The cut $|\cos(\theta_T)| < 0.71$ is chosen to ensure that events are contained within the fiducial region of the detector.

A total of 86679 events from the 1993,1994 and 1995 SLC/SLD runs survived these cuts and were included in this analysis. A typical hadronic event is shown in Fig. 4.7. The efficiency for selecting hadronic events satisfying the $|\cos(\theta_T)|$ cut was estimated

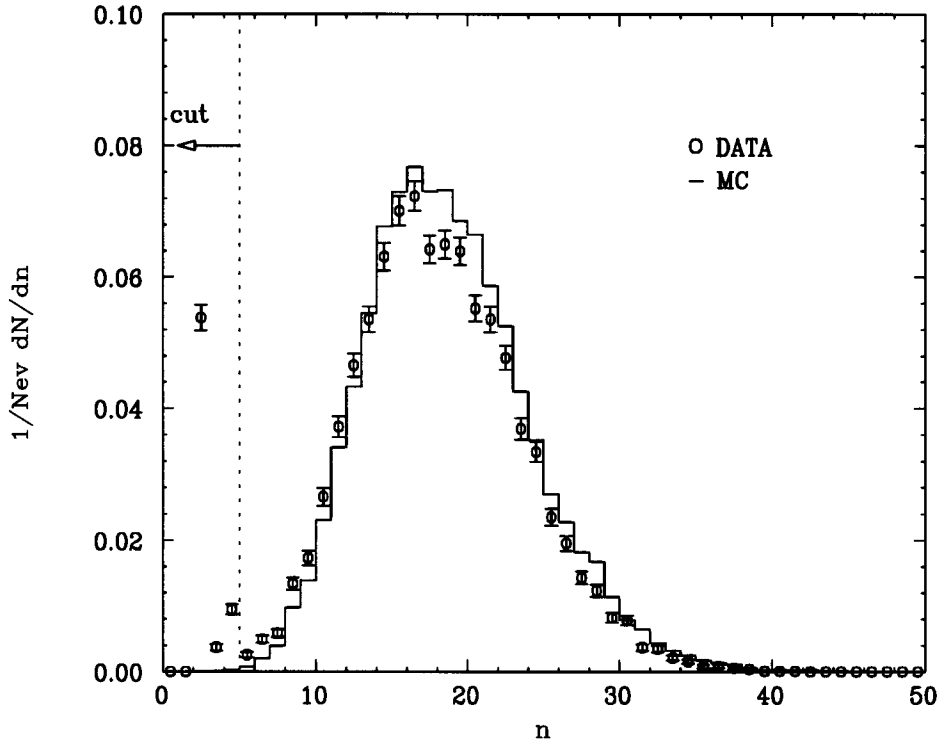

Figure 4.4: The charged-particle multiplicity distribution (before cut).

to be above 96%. Distributions of single particle and event topology observable in the selected events were found to be well described by Monte Carlo models of Z^0 decays combined with a simulation of the SLD [41].

4.4 Background Estimation

The selected hadronic event sample as described above still can be contaminated with some backgrounds. In this section, we consider three major sources of backgrounds: $\tau^+\tau^-$ pairs, two-photon and beam-related events. A typical $\tau^+\tau^-$ events is shown in Fig. 4.8.

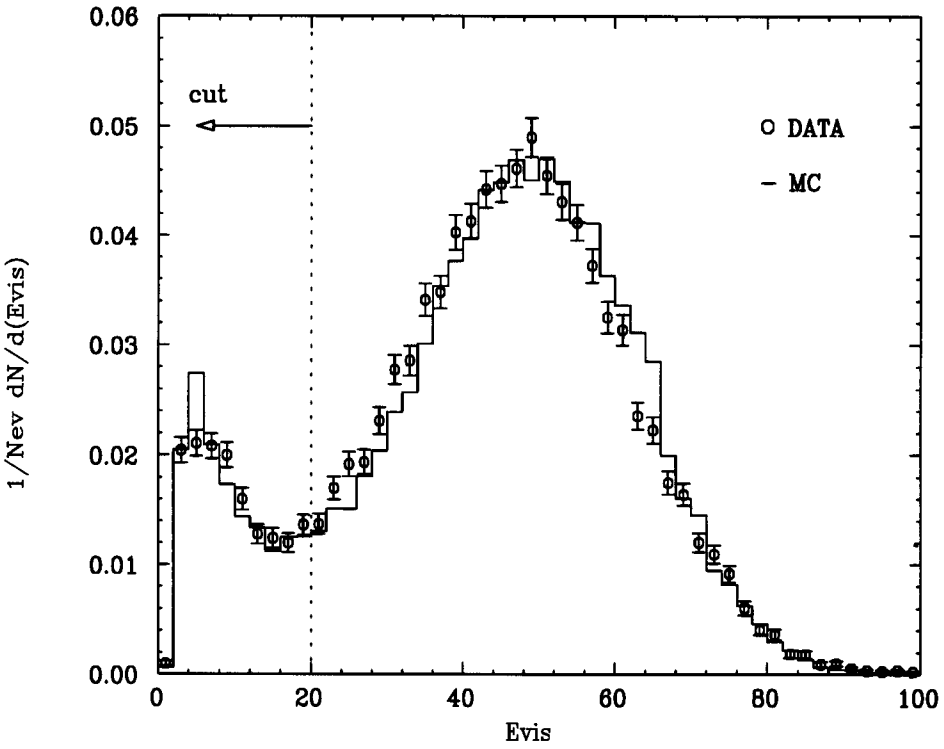

Figure 4.5: Visible energy distribution.

4.4.1 $\tau^+\tau^-$ pairs

The main decay modes of τ are semileptonic: $\tau^{\pm} \rightarrow l^{\pm}\nu_l\nu_\tau$, where $l = e, \mu$, or hadronic: $\tau \rightarrow K/\pi\nu_\tau$. The branching ratio of 1-prong decays (i.e., τ into one charged and multiple neutral particles) is 85.5%, and 14.4% for 3-prong decays. The requirement of a minimum of 5 charged tracks in the hadronic event selection is expected to exclude 97.7% of all $\tau^+\tau^-$ events. The contamination can be estimated more precisely by using a MC sample of $\tau^+\tau^-$ events. It was found [43] that $4.20 \pm 0.13\%$ of the tau pair sample passed the hadronic event section criteria. This number is larger than the expected 2.3% due to additional charged tracks created by γ conversions or interactions in the detector material. The contamination of $\tau^+\tau^-$ pairs in our hadronic event sample is thus estimated to be $0.20 \pm 0.07\%$, taking into account the ratio of $\mathrm{BR}(Z^0 \rightarrow \tau^+\tau^-)/\ \mathrm{BR}(Z^0 \rightarrow \text{hadrons}) = 4.7\%$.

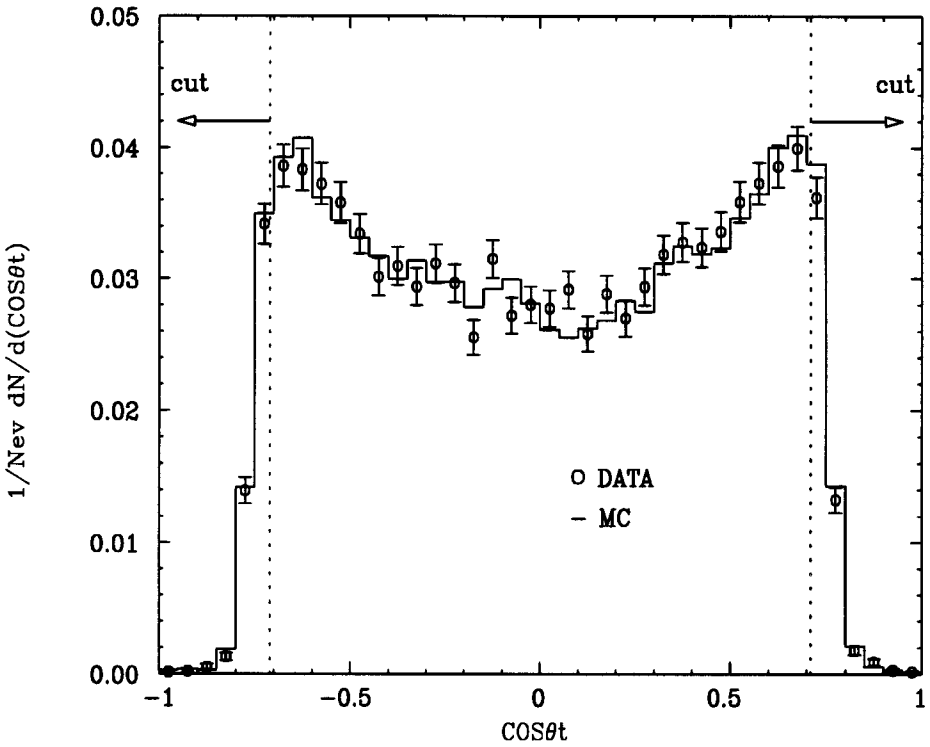

Figure 4.6: $\cos(\theta_{thrust})$ distribution.

4.4.2 Two-photon events

The two-photon process is defined as $e^+e^- \rightarrow e^+e^- + \gamma\gamma, \gamma\gamma \rightarrow$ hadrons, with cross section equal to 6.5 nb at $\sqrt{s} = M_z$. These events are usually of low visible energy, and peaked very forward, so that very few are energetic enough to trigger the detector. A MC study similar to the $\tau^+\tau^-$ case shows the contamination of this process in the hadronic event sample is about $0.10 \pm 0.03\%$ [43].

4.4.3 Beam-related events

The events created by the interactions of an e^+, or e^- from beam with the beam pipe wall or material inside the pipe are called beam-related events. These events can be easily identified due to their characteristics such as large momentum imbalance. It is

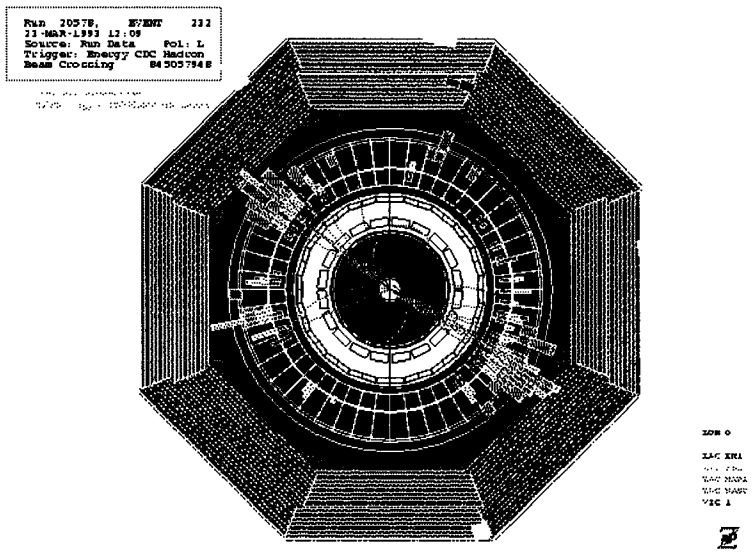

Figure 4.7: A typical hadronic event. Shown is a view looking parallel to the beam axis. The lines indicate charged tracks.

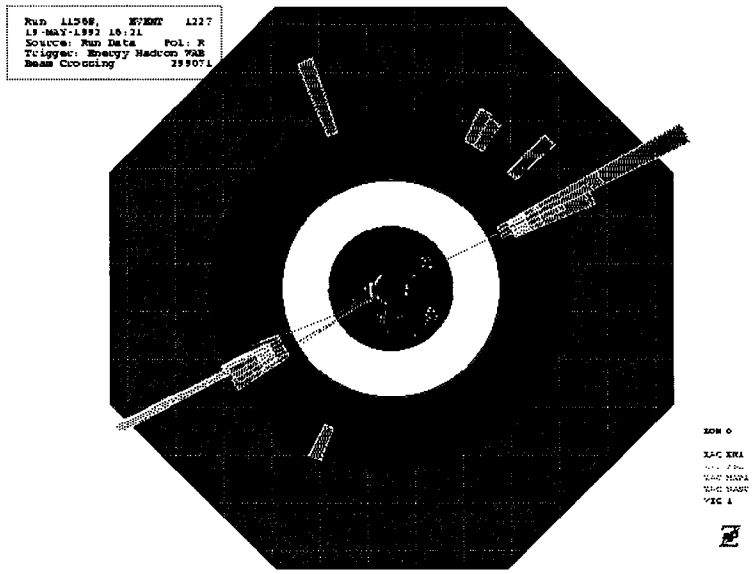

Figure 4.8: A typical $\tau^+\tau^-$ event. Shown is a view looking parallel to the beam axis.

unlikely to calculate their cross sections, since their production rate is strongly dependent on the beam conditions which can vary from time to time. The contamination of these events was estimated to be less than 0.1% [43].

The total contamination of backgrounds in the hadronic event sample was estimated to be less than 0.4%. This value is considered to be small. The effect of background contamination will be considered in the analysis.

Chapter 5

Tracking Efficiency

Understanding the tracking efficiency of the detector is essential to many physics analyses performed with SLD. It is, however, difficult to determine the tracking efficiency in most cases where the input to the detector is unknown and is sometimes the thing to be measured. The measurement of hadronic multiplicity is one such example. Traditionally, Monte Carlo has been used to simulate the detector tracking efficiency, which is then applied to the observed data to yield the physics results. Apparently, such measurements have strong model dependences. For a better measurement, we attempt to improve the Monte Carlo simulated tracking efficiency, based on studies of the tracking efficiency determined from WAB and tau pair events where the input is known.

5.1 Tracking Efficiency for Single Track

We begin with the study of the tracking efficiency for isolated tracks using wide angle Bhabha (WAB) events measured in the LAC. A well measured WAB event must have two back to back EM clusters in the LAC. Correspondingly, there should be two back to back tracks in the CDC associated with the measured EM clusters in the LAC (if the tracking efficiency in the CDC is 100%). The first thing needed for this study is to select well measured WAB events.

5.1.1 WAB selection

The selection criteria of WAB events make use of the low multiplicity and the high energy deposition into two clusters in the EM section of the LAC, which will be back to back. We start with the selection of good clusters, which are required to have the following properties:

- $E_{EM} > 0.0$ GeV
- $E_{clus} > 1.0$ GeV
- not tagged as an SLC μ.

The EM clusters are then tagged by requiring:

- $E_{EM} > 10$ GeV
- $E_{HAD1} < 3$ GeV
- $E_{HAD2} < 0.5$ GeV.

where E_{EM} is the cluster energy deposited in the EM section, E_{HAD1} (E_{HAD2}) is the cluster energy in HAD1 (HAD2). These well measured events are then required to have:

- $E_{tot} > 15$ GeV
- $I < 0.6$
- $N_{clus} < 9$.
- $|\cos(\theta_t)| < 0.7$
- $N_{EM} = 2$

where E_{tot} is the total energy summing over the number of selected clusters N_{clus}, I is the energy imbalance, and θ_t is the thrust angle of the event. The cuts applied here are based on work done by K. Pitts & J. Yamartino (see [35, 40] for details), but are tighter to ensure that the event is in a well defined region of detector. In addition, two EM clusters are required.

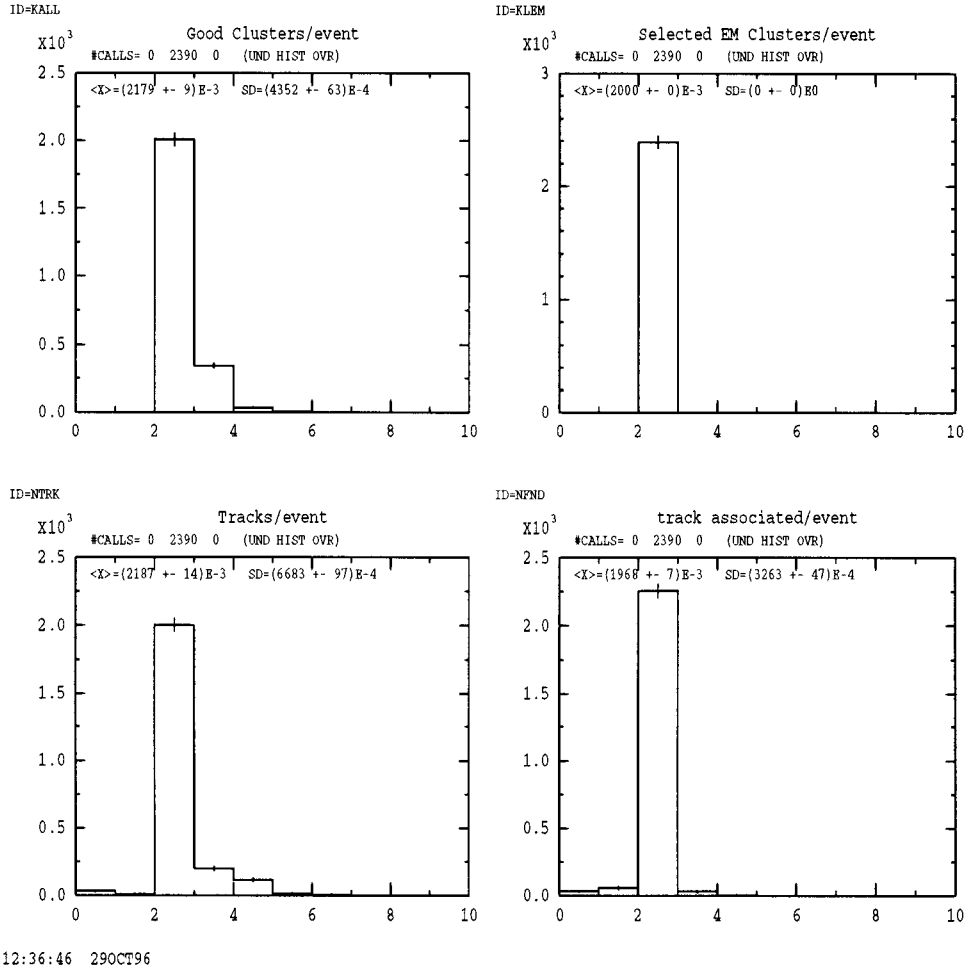

Figure 5.1: For the selected WAB events, distributions of the number of selected good clusters (top left), the number of selected EM clusters (top right), the number of found tracks (bottom left), and the number of tracks associated with the EM clusters (bottom right).

5.1.2 Results

Some distributions for the selected WAB events are shown in Fig. 5.1. In most cases, there are exactly two tracks associated with the two tagged EM clusters, while in some cases there are less or more than two associated tracks (see Fig. 5.1 bottom right). Fig. 5.2 shows an example where one track is missing, and Fig. 5.3 shows an example where two tracks are missing. However, in the events such as the one

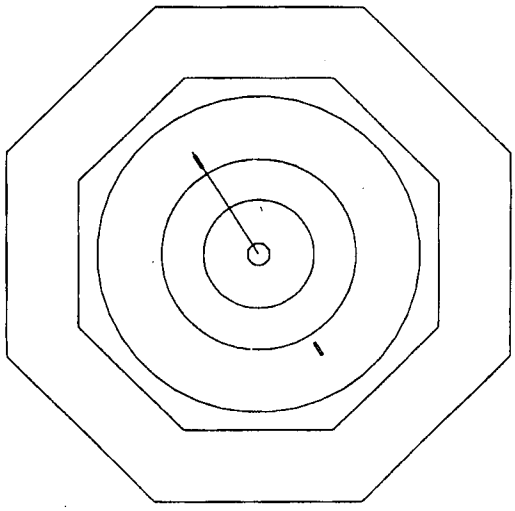

Figure 5.2: A WAB event with one track lost.

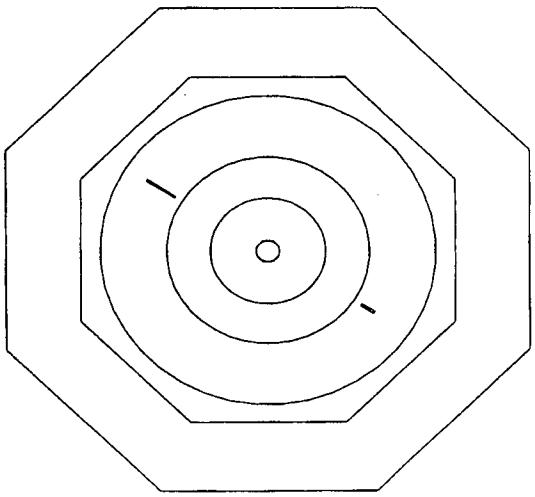

Figure 5.3: A WAB event with two tracks lost.

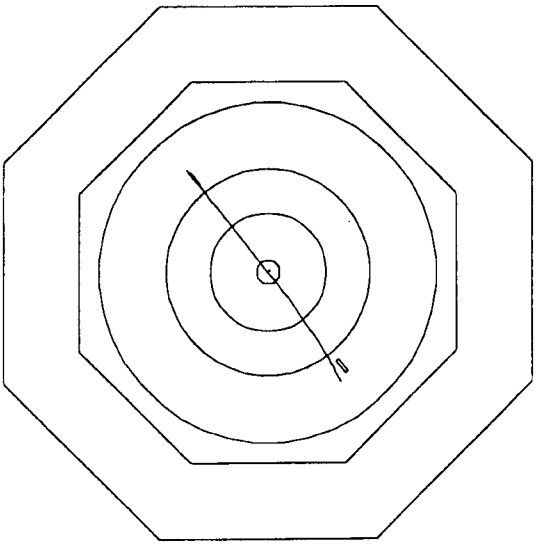

Figure 5.4: A WAB event with one un-associated track due to γ radiation.

shown in Fig. 5.4, the track is actually found but not associated with the cluster. This could be due to γ radiation. From the point of view of the tracking efficiency, this un-associated track is counted as found.

For those events in which tracks are missing, we seek to isolate the cause of tracking inefficiency. To do this, we reprocessed these events and carefully checked each step of the track reconstruction. The track reconstruction in SLD is accomplished via four steps, as described in detail in Chapter 3 and summarized below:

- find the raw hits.
- form the raw hits within each cell into a track segment, usually called a vector hit (VH).
- link VHs together into track candidates (a process also called pattern recognition)
- process all candidates by an iterative tracking fitter, yielding a set of parameters best describing the tracks.

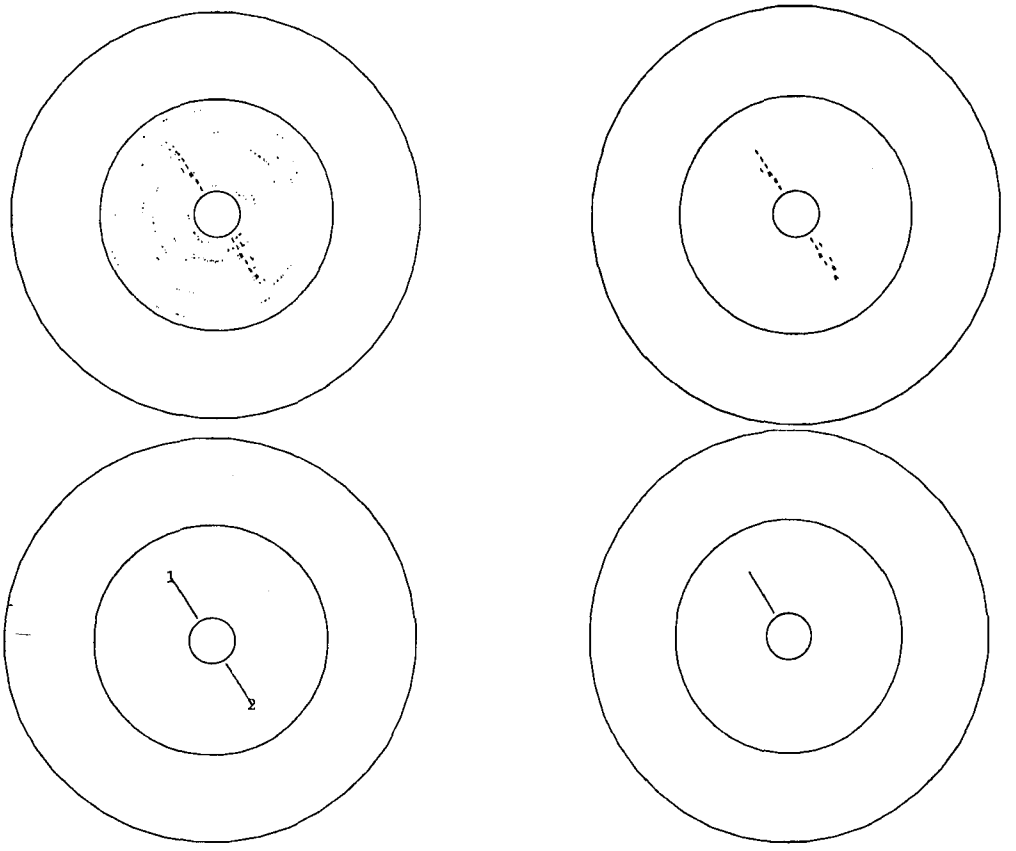

Figure 5.5: Reconstruction of a WAB event with one track lost. Top left shows the status of raw hits finding, top right shows the status of VHs, bottom left shows the status of pattern recognition, and bottom right shows the status of track fitting.

The result of each step of the reconstruction for the event shown in Fig. 5.2 is presented in Fig. 5.5. It can be seen from the above event display that the track reconstruction proceeded successfully through the pattern recognition, but failed the fitting process. This was found to be due to a cut on χ^2 in all such cases. This track could be recovered (see Fig. 5.6) by loosening the standard χ^2 cut. We followed the same exercise for the events such as the one shown in Figure 5.3, and found that the lost tracks were actually due to a corrupted CDC constant file, confined to a specific run period in 1993. This group of events was excluded from the tracking efficiency study.

In total, we have 2390 well measured WAB events. A total of 20 tracks were found

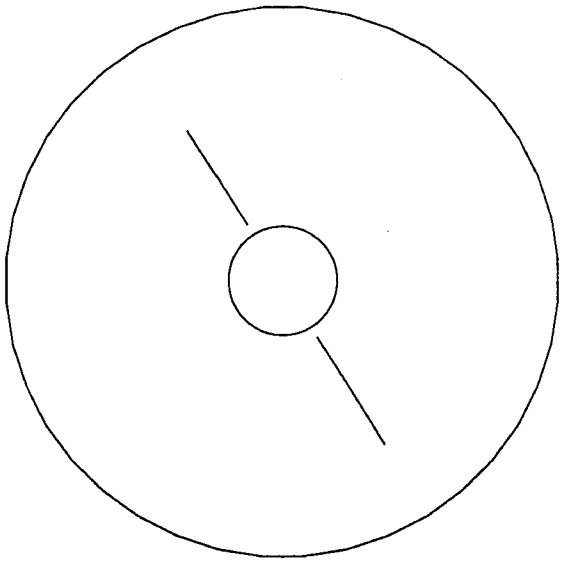

Figure 5.6: The lost track could be recovered when SLD standard χ^2 cut was loosened by a factor 2.

to be lost due to the χ^2 cut. Thus, the tracking efficiency for the isolated tracks is measured to be $99.58 \pm 0.13\%$. The same analysis was performed on WAB Monte Carlo, and we found that the efficiency was $99.85 \pm 0.01\%$, which is slightly higher than in the data. The efficiency difference between data and MC is $0.27 \pm 0.13\%$.

5.2 Momentum Dependence of Tracking Efficiency

It is known that the tracking efficiency for low momentum particles is lower. Such dependence on momentum can be studied using a sample of one-prong tau pair events.

Tau pair events are selected according to the standard SLD tau event selection criteria as listed in the Table 5.1 [44]. The tau pair multiplicity distribution is shown in Fig. 5.7. Figure 5.8 shows the momentum spectrum. In both cases, the data and MC are in good agreement. Since the properties of τ decays are well known and the data is well reproduced by MC, we thus use MC to study the momentum dependence.

True one prong MC events were selected in order to study the momentum dependence of the tracking efficiency for isolated tracks. Charged and stable particles

Table 5.1: SLD Tau Selection Cuts

Cut Name	Cut Value	Removes
Two Hemispheres	> 1 track in each hemi.	Garbage
Visible Energy	$Evis > 10$ GeV	Two Photon
EM Energy	$E_{em} < 62.5$ GeV	WAB
Neutral Clusters in Jets	$\#clusij < 9$	Multihadron
Ekal outside Jets	$Ekaloj < 5$ GeV	Multihadron
Good Tracks	$\#tracks \leq 6$	Multihadron
Jet cones	$Jet - trackangle < 15$ deg.	Multihadron
Multiprong Acolinearity	$Acol < 20$ deg.	Multihadron
Jet Mass	$M_{jet} < 2.3$ GeV	Multihadron
Two largest tracks	$p1 + p2 < 65$ GeV	WAB, Mu pair
2 Prong Acolinearity	$A_{col} > 10$ mRad	WAB, Mu Pair
Missing Momentum	$\|cos(\theta_{missing})\| < 0.88$	WAB, Two Photon

with momentum p were generated. Only particles passing through the CDC were tagged. The reconstruction was then performed to see if the tagged particles were actually found. Thus, the tracking efficiency as a function of momentum p is simply formulated as

$$eff(p) = \frac{n_{fnd}(p)}{n_{gen}(p)}, \tag{5.1}$$

where $n_{gen}(p)$ was the generated number of particles with momentum p, and $n_{fnd}(p)$ was the number found. The resulting efficiency from MC is shown in Fig. 5.9. It can be seen that the efficiency increases with the momentum p, and is close to 100% at high momentum, which is consistent with the WAB data.

5.3 Tracking Efficiency in 3 prong τ decays

Tracks are most likely to be lost when they are close to each other. This has been studied in 3 prong τ decays where the tracks are typically not well separated. An

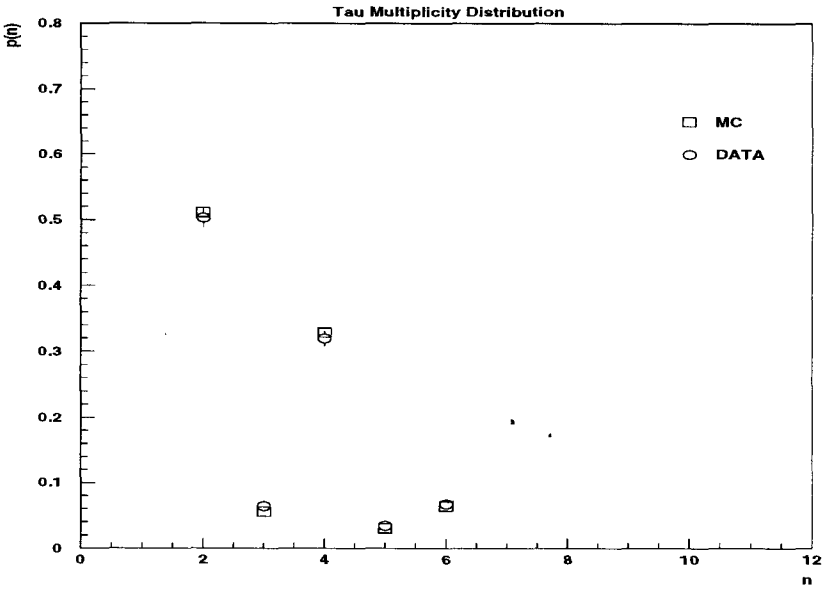

Figure 5.7: Tau pair multiplicity distribution.

example of a 3 prong τ decay is displayed in Fig. 5.10. Figure 5.11 shows the opening angle distribution of track pairs in 3 prong events. We find that the data and MC agree well.

The tracking efficiency for 3 prong decays is determined from both MC and data. Initially, we assume that the event topology 1-2 is attributed to one track lost from a 1-3 event. Table 5.2 shows the results. The tracking efficiency for 3 prong decays is thus

Table 5.2: Number of τ pair events with topology 1-2 and 1-3 in data and MC.

τ pair topology	# of events (data)	# of events (MC)
1-2	161	2455
1-3	802	14384

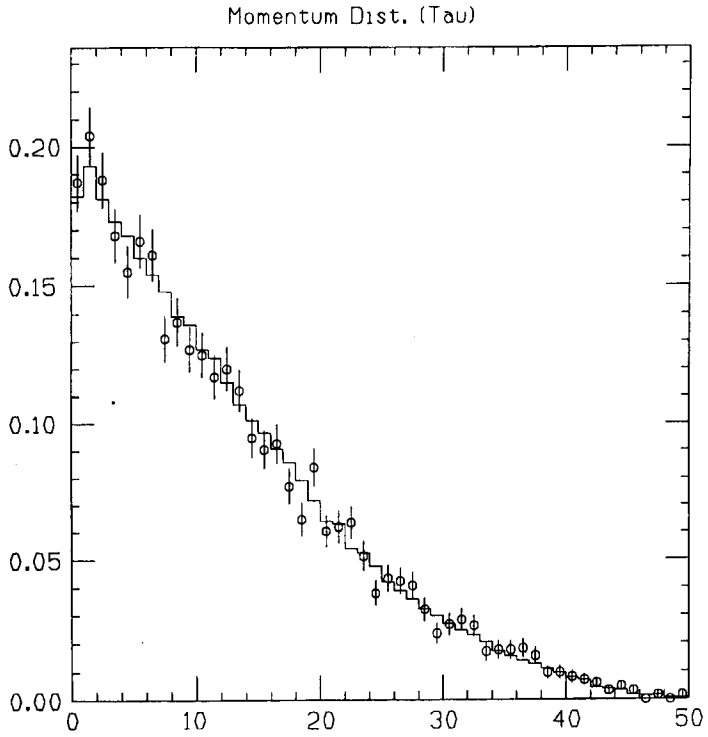

Figure 5.8: Momentum distribution of the charged particles in tau pair events. The histogram represents τ pair MC and the open circles represent the data.

estimated to be $eff(data) = 94.43 \pm 0.42\%$ for data, and $eff(MC) = 95.14 \pm 0.10\%$ for MC.

The 1-1 events may have some contributions to 1-2 as well due to conversions. This contribution can be estimated by generating a number of 1-1 events and checking how many of them are reconstructed as 1-2. Table 5.3 shows the numbers. Thus, the

Table 5.3: Number of generated 1-1 events and the number reconstructed as 1-2.

# of Generated 1-1 events	25594
Reconstructed as 1-2	1457

contribution to 1-2 from 1-1 is 5.69%

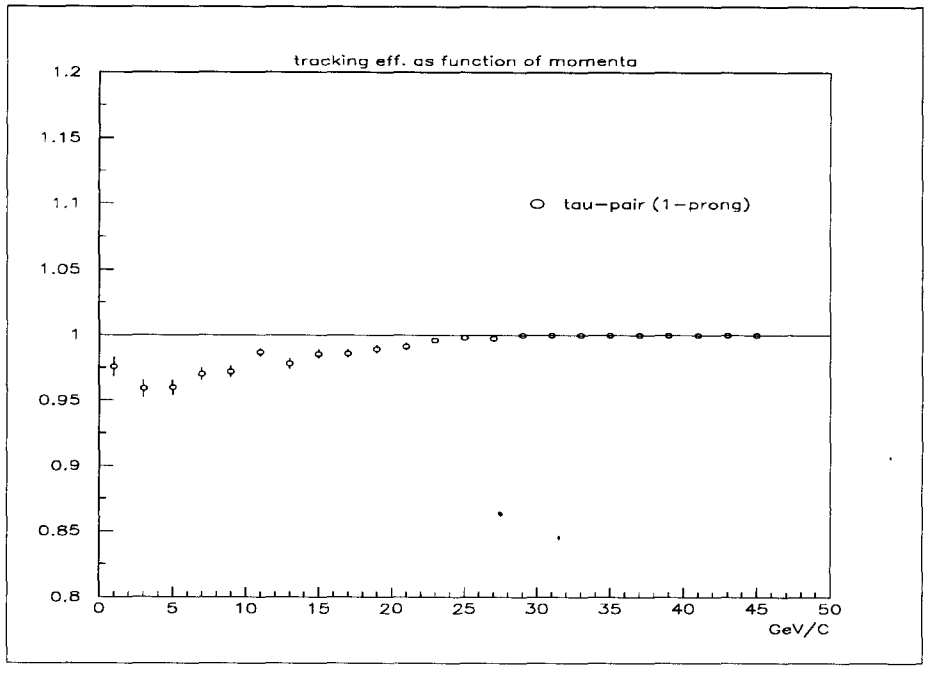

Figure 5.9: Tracking efficiency as a function of momentum p, determined from one prong tau pair MC sample.

Taking the 5.69% contribution from 1-1 into account, the tracking efficiencies for 3 prong decays (shown above) are corrected and calculated to be $eff(data) = 96.67 \pm 0.35\%$ for data, $eff(MC) = 97.47 \pm 0.07\%$ for MC. The efficiency difference between data and MC is $eff(MC - data) = 0.8 \pm 0.36\%$.

5.4 Summary

We studied the tracking efficiency of the detector using well measured WAB events and tau pair events. The efficiency for stand-alone tracking is determined from WAB events, and we found the efficiency difference between data and MC to be $0.27 \pm 0.13\%$. The momentum dependence of the efficiency is studied using one prong tau pair events, and we found that the efficiency increases with the momentum p, and is

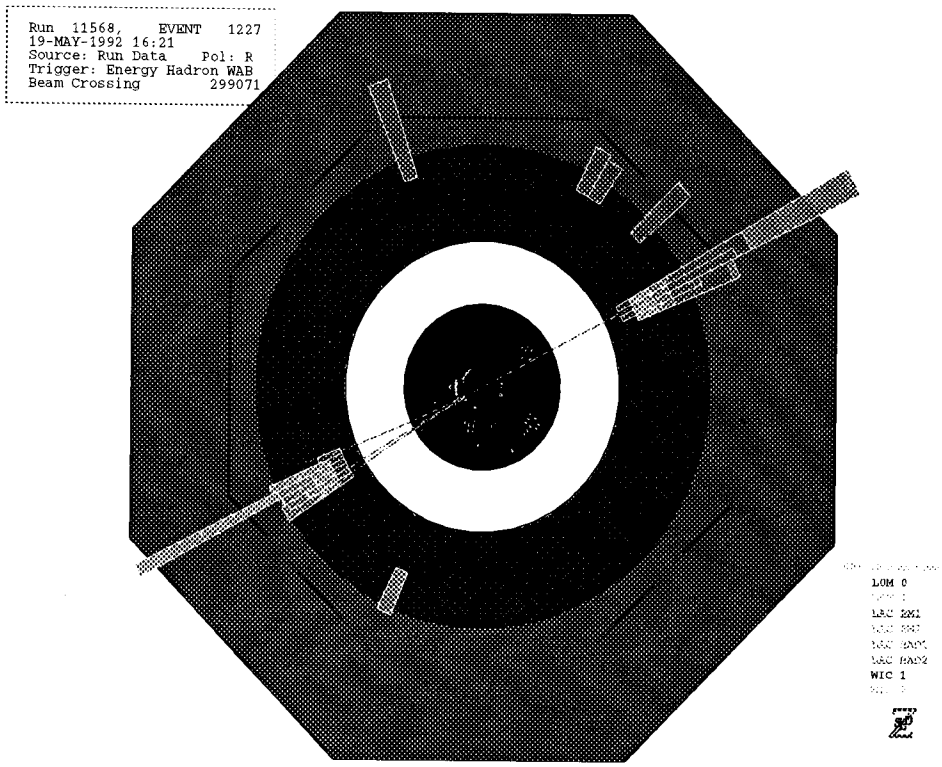

Figure 5.10: An example of a τ pair event with 1-3 topology.

close to 100% at high momentum, which is consistent with the WAB data. We also investigated the tracking efficiency in 3 prong tau decays where the tracks are usually poorly separated. The efficiency difference between data and MC was found to be $0.8 \pm 0.36\%$. These results will be used to correct the hadronic Monte Carlo in the next chapter.

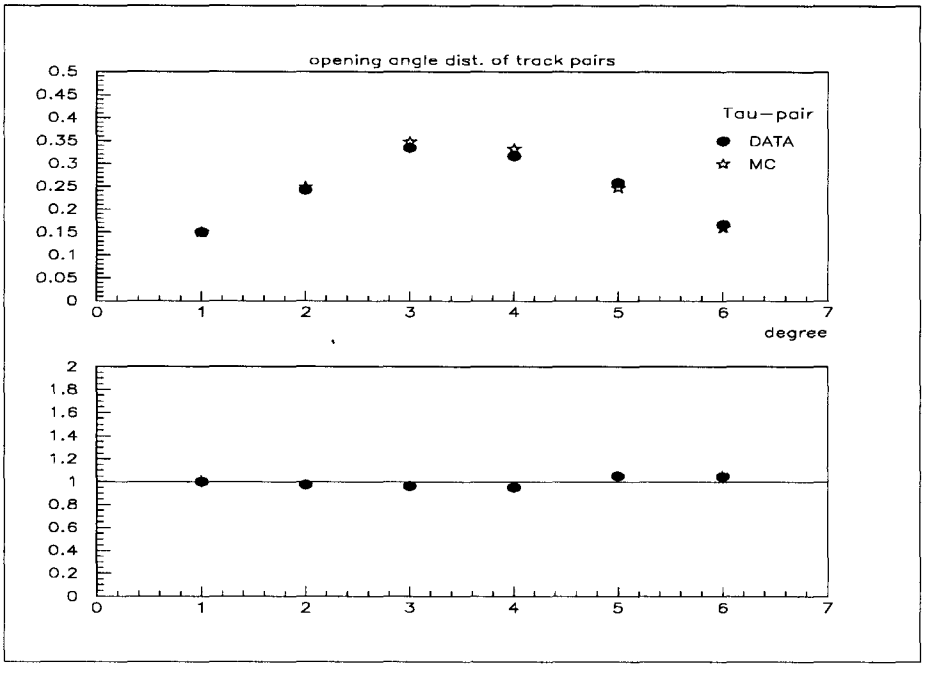

Figure 5.11: The comparison of the opening angle (in degrees) of track pairs in 3-prong event between data and MC (top plot). The bottom plot shows the ratio of MC and data.

Chapter 6

Multiplicity Distribution

6.1 Introduction

One of the most fundamental observables in high-energy particle interactions is the multiplicity distributions of charged hadrons produced in the final states. The distributions are expected to contain valuable information about the dynamics of hadron production, and have been studied extensively both experimentally and theoretically (for reviews see [45]).

Experimental data are available for a large variety of interactions: hadron-hadron, lepton-hadron and electron-positron collisions. The Poisson distribution (PD) has been found to considerablly deviate from the data, implying that the particles are not produced independently. Phenomenological models have yielded improved descriptions of the data. For example, models in which the interaction produces a number of objects, each of which decays into a random number of particles, predict a negative binomial distribution (NBD), which provides a good parameterization of much experimental data [46]. The theory of strong interaction, Quantum Chromodynamics (QCD), cannot at present be used to calculate the multiplicity distribution of the final state hadrons since the mechanism of hadronization has not been solved. However, perturbative techniques (PQCD) can be applied to calculate the multiplicity distribution of partons [47].

In this chapter, we present the experimental study of the charged particle multiplicity distribution from e^+e^- annihilations into hadrons at the Z^0 resonance. Our results are compared with those obtained by other experiments at the same and at lower center-of-mass energies, as well as with the expections of perturbative QCD and phenomenological models. This chapter is arranged as follows: section 2 describes the correction procedure, section 3 discusses the systematic uncertainties affecting our measurement, the results are presented in section 4, followed by a summary in section 5.

6.2 Correction Procedure

The charged particle multiplicity distributions observed experimentally need to be corrected for the loss of tracks due to the limited geometrical acceptance and resolution of the detector as well as for the tracking inefficiency. Meanwhile, any faked tracks produced due to γ conversions and particle interactions in the material of the detector should be excluded. In addition, the biases introduced due to track and event selection criteria and QED initial state radiation should also be corrected.

The final charged multiplicity distribution to be presented were corrected for all the effects mentioned above. In this analysis, the charged multiplicity of an event is defined to include all promptly produced charged particles, as well as those produced in the decay of particles with lifetime $\tau < 3 \times 10^{-10} s$ (see Table 6.1). Thus, the charged decay products of K_s^0 and strange baryons are included.

Our correction was performed using approximately 146,000 hadronic Z^0 decays generated according to the JETSET 6.3 [48] event generator plus a detailed simulation of the SLD detector. These Monte Carlo (MC) events were then reconstructed in the same way as the data. For each such MC event passing the same selection criteria (or cuts) as applied on the data (see chapter 4), the number of observed tracks n_o, with distribution $N_{obs}^{MC}(n_o)$, was compared with the number of generated tracks n_g, with distribution $N_{gen}^{MC}(n_g)$. This comparison yielded the correction matrix $M(n_g, n_o)$ whose elements are defined as

particle	lifetime	decay modes
K_s^0	$0.89 \cdot 10^{-10}$	$\pi^+\pi^-$
Λ	$2.63 \cdot 10^{-10}$	$p\pi^-$
Σ^+	$0.80 \cdot 10^{-10}$	$p\pi^0, n\pi^+$
Σ^-	$1.63 \cdot 10^{-10}$	$n\pi^-$
Ξ^-	$1.63 \cdot 10^{-10}$	$\Lambda\pi^-$
Ω^-	$0.82 \cdot 10^{-10}$	$\Lambda K^-, \Xi^0\pi^-$

Table 6.1: Charged decay products. Only main decay modes are listed.

$$M(n_g, n_o) = \frac{N(n_g, n_o)}{N_{obs}^{MC}(n_o)}, \tag{6.1}$$

where $N(n_g, n_o)$ stands for the number of MC events with n_g generated tracks when n_o tracks were observed. The correction matrix is displayed in Fig. 6.1. The observed distribution $N_{obs}^{MC}(n_o)$ is thus related to the generated distribution $N_{gen}^{MC}(n_g)$ by

$$N_{gen}^{MC}(n_g) = \sum_{n_o} M(n_g, n_o) \cdot N_{obs}^{MC}(n_o). \tag{6.2}$$

The MC sample employed for constructing the correction matrix had cuts applied, and consequently did not reflect exactly the true multiplicity distribution. In addition, QED initial state radiation results in a small bias to the multiplicity. Both biases were corrected by using a set of factors $C_F(n_g)$, which were calculated from MC by comparing the normalized generated multiplicity distribution $P^{fix}(n_g)$ at fixed c.o.m energy in the total sample, to the normalized generated multiplicity distribution $P^{sub}(n_g)$ in the sub-sample (i.e., the one which passed the applied cuts),

$$C_F(n_g) = \frac{P^{fix}(n_g)}{P^{sub}(n_g)}. \tag{6.3}$$

The correction factors C_F are shown in Fig. 6.2. Finally, the correction matrix M and correction factors C_F were applied to the experimentally observed multiplicity distribution $N_{obs}^{exp}(n_o)$ to yield the corrected multiplicity distribution, $N_{cor}^{exp}(n)$:

$$N_{cor}^{exp}(n) = C_F(n) \cdot \sum_{n_o} M(n, n_o) \cdot N_{obs}^{exp}(n_o). \tag{6.4}$$

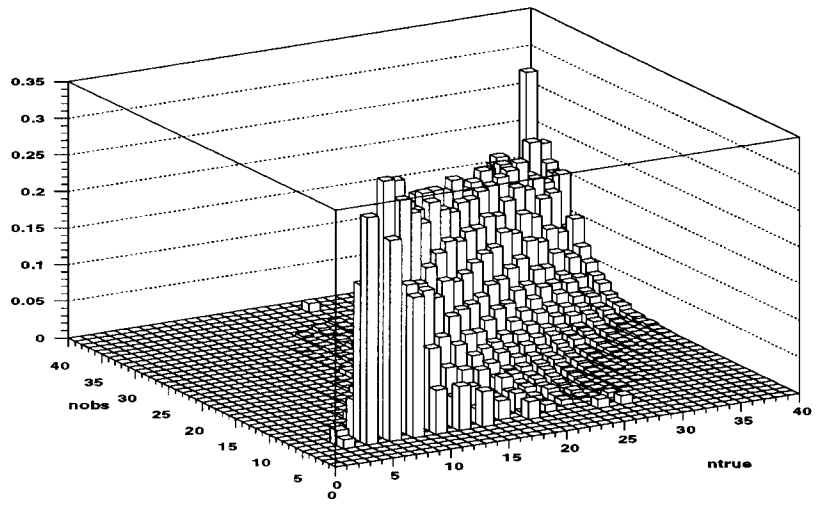

a. Three dimensional view.

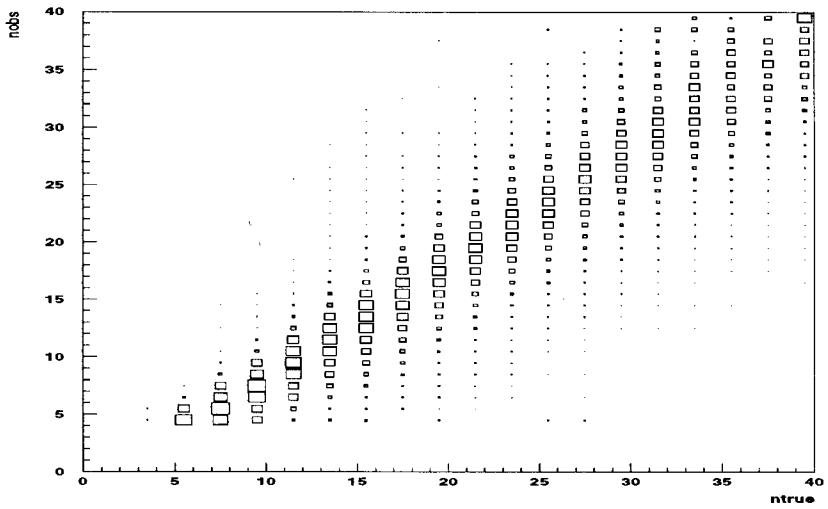

b. Two dimensional view. The box size is proportional to the value of probability.

Figure 6.1: Overview of correction matrix

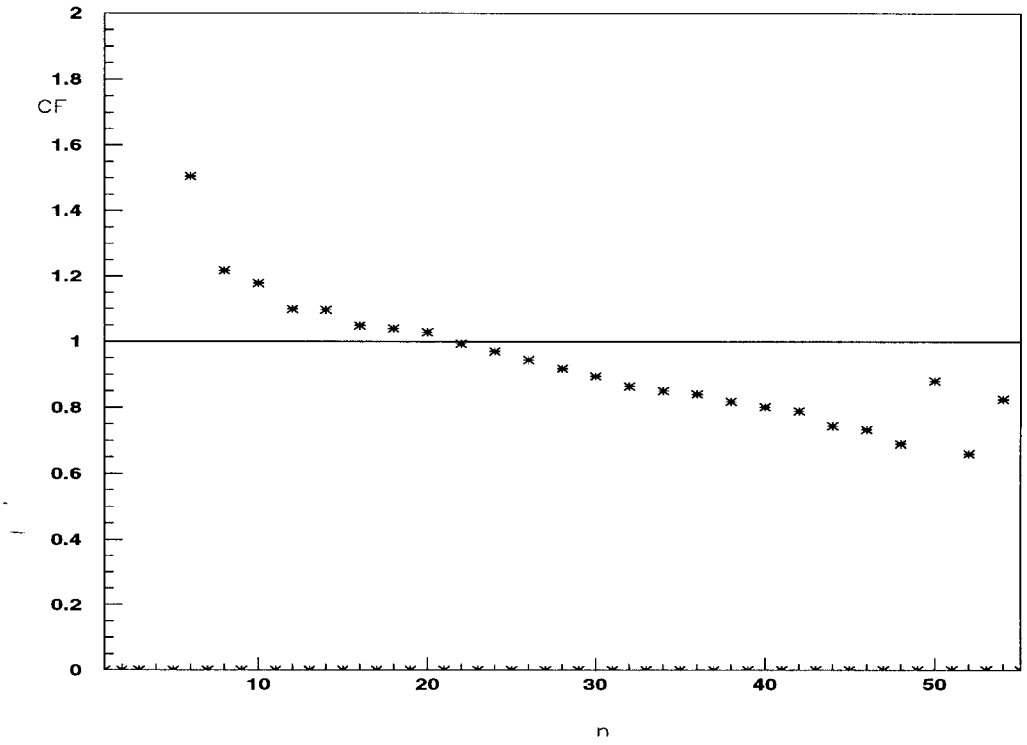

Figure 6.2: Correction factors C_F.

To provide a reliable correction of the data, the multiplicity distribution observed experimentally must be well reproduced by the simulated MC events. This is the case in this analysis although a slight derivation can be seen as shown in Fig. 6.3. Any possible difference between the actual detector performance and that represented in the simulation will be evaluated to contribute to the systematic uncertainties as discussed below.

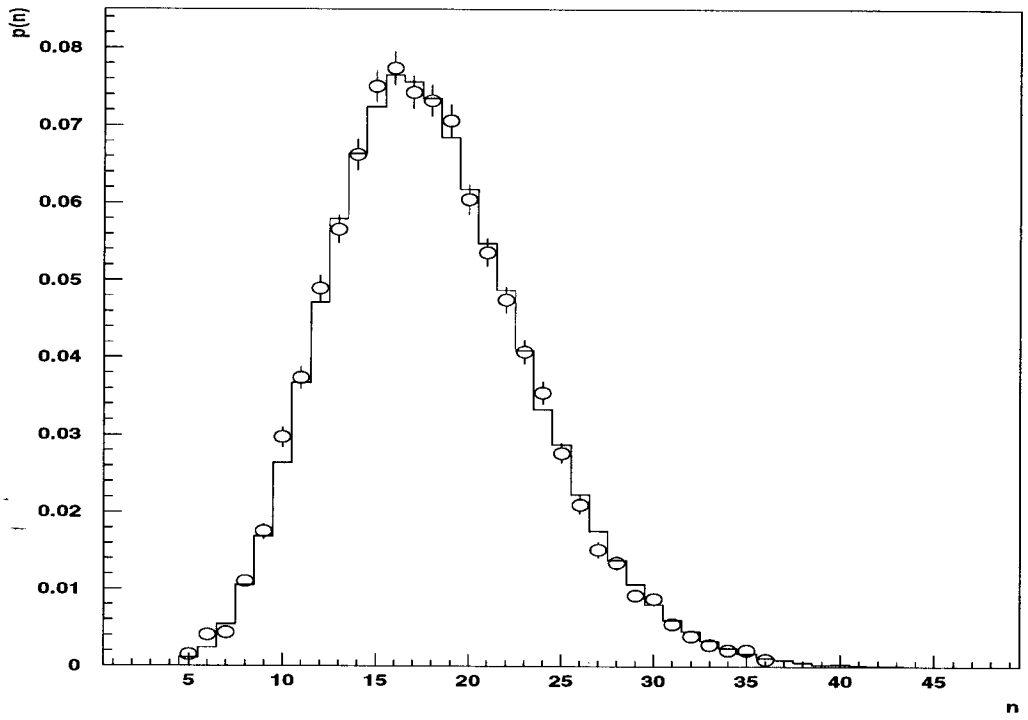

Figure 6.3: The observed (uncorrected) multiplicity distributions compared with MC shown in histogram.

6.3 Systematic Uncertainties

We have examined the following contributions to the experimental systematic uncertainties. In some cases the entire correction and analysis process will be repeated in order to test the influence of a systematic effect on the final results.

- Tracking efficiency:

  The correction matrix $M(n_g, n_o)$ determined above from Monte Carlo represents the simulated detector tracking efficiency. The tracking efficiency has been studied using well measured WAB and tau pair events as discussed in Chapter 5, and we found that the difference between the actual detector tracking efficiency

and the Monte Carlo simulated efficiency is $0.27 \pm 0.13\%$ for isolated tracks, and $0.8 \pm 0.36\%$ for poorly seperated tracks. The Monte Carlo was thus corrected by tossing 0.27% for well seperated tracks and tossing 0.8% for poorly separated tracks. The uncertainties in the differences were transfered to the systematic error for the final results.

- Statistical fluctuations in the correction matrix:

  The correction matrix $M(n_g, n_o)$ was constructed from a Monte Carlo sample with finite statistics. The display of slices of the correction matrix with statistical errors is shown in Fig. 6.4. The stability of our results has been tested by using a smoothed version of the correction matrix found by parameterization as shown by the solid curves. The difference compared with that calculated from the original matrix was conservatively taken as a systematic error. This systematic uncertainty can be estimated more realistically by a set of correction matrices generated by a parameterized distribution (as will be discussed in Chapter 7).

- Model dependence:

  Since the event selection criteria required at least 5 observed tracks, the values of the corrected multiplicity distribution at entry $n = 2$ and $n = 4$ were not derived from the data but were taken instead from the expectation of JETSET 6.3. The difference with the case when these entries are not included in the calculation is included in the systematic error.

- Hadronic event and track selection.

  The sensitivity to the definition of well measured tracks and the selection of hadronic events has been tested. The criteria for selecting well-measured tracks, like impact parameters (R and Z), transverse momentum, track polar angle, and the criteria for selecting good hadronic events, like invisible energy, thrust polar angle, minimum number of tracks, were varied over a wide range. A new set of correction matrices and correction factors were computed and applied to the

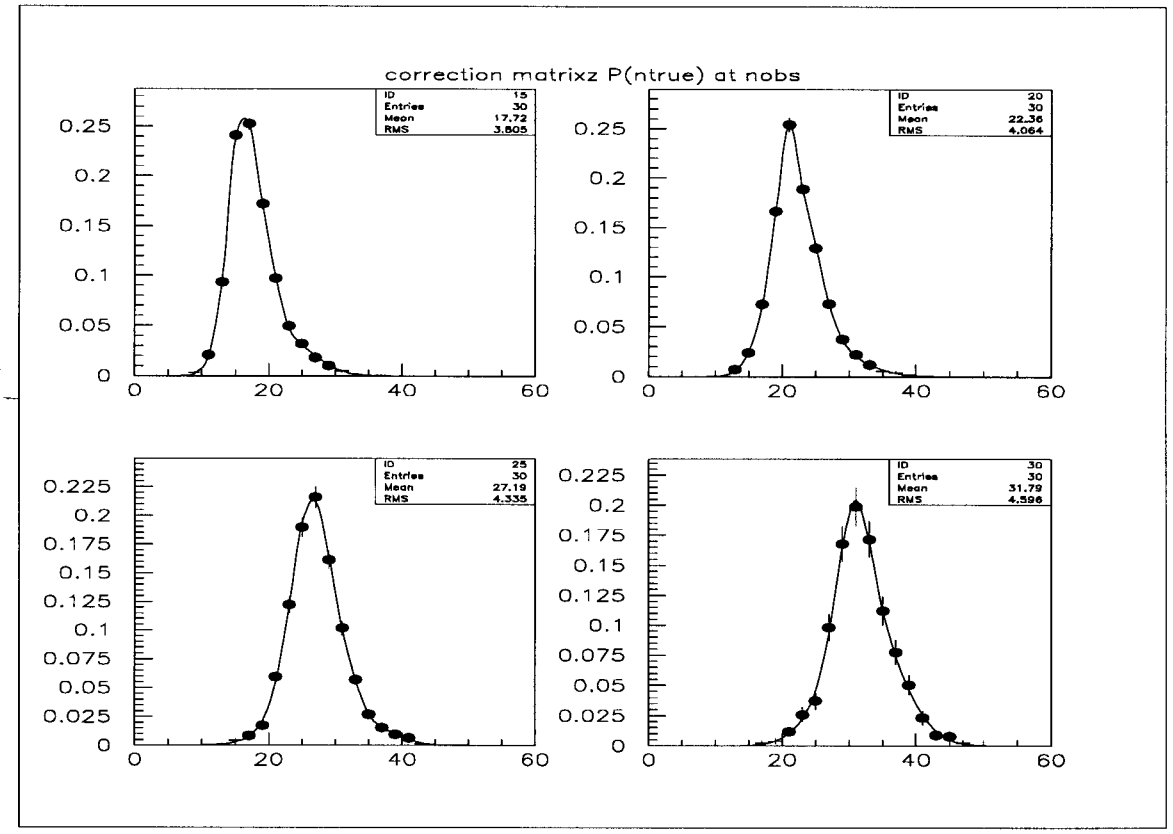

Figure 6.4: The display of slices of the correction matrix: the probability distribution of having n_g for fixed n_o. The solid curve represents a fit to three Gaussian distributions.

data, processed with the corresponding criteria. Any significant sensitivity to the selection was included in the systematic error.

A number of other systematic effects which are sensitive to the higher order moments study will be discussed in the next chapter.

6.4 Results

The charged multiplicity distribution observed experimentally (uncorrected) is listed in Table 6.2, and the comparison with MC is shown in Fig. 6.3. The corrected charged multiplicity distribution is presented in Table 6.3, together with the lists of the statistical and systematic errors. The distribution was normalized, giving $p(n)$ to be the probability of having a hadronic Z^0 decay with n charged particles. The leading moments computed from the corrected distribution are presented in Table 6.4. The moments include the average charged multiplicity $< n >$, the ratio of $< n >$ and the dispersion $D = (< n^2 > - < n >^2)^{1/2}$, and the second binomial moment R_2, where

$$R_2 = \frac{< n(n-1) >}{< n >^2} = 1 + \frac{D^2}{< n >^2} - \frac{1}{< n >}. \tag{6.5}$$

The systematic errors are the quadratic sum of all the contributions to the systematic uncertainties.

6.4.1 Average Multiplicity

The average charged multiplicity calculated from the corrected distribution is $20.63 \pm 0.01 \pm 0.34$. The contributions to the overall systematic error are listed in Table 6.5. Our data is in good agreement with those measured at the same center-of-mass energy by MARK II [49], DELPHI [50], ALEPH [51], OPAL [52] and L3 [53]. The comparison with these data is listed in Table 6.6.

To study the energy dependence of average multiplicity $< n >$, we compared our data with those measured at different energies, as shown in Fig. 6.5. A number of phenomenological models have been proposed to describe the evolution of $< n >$ with

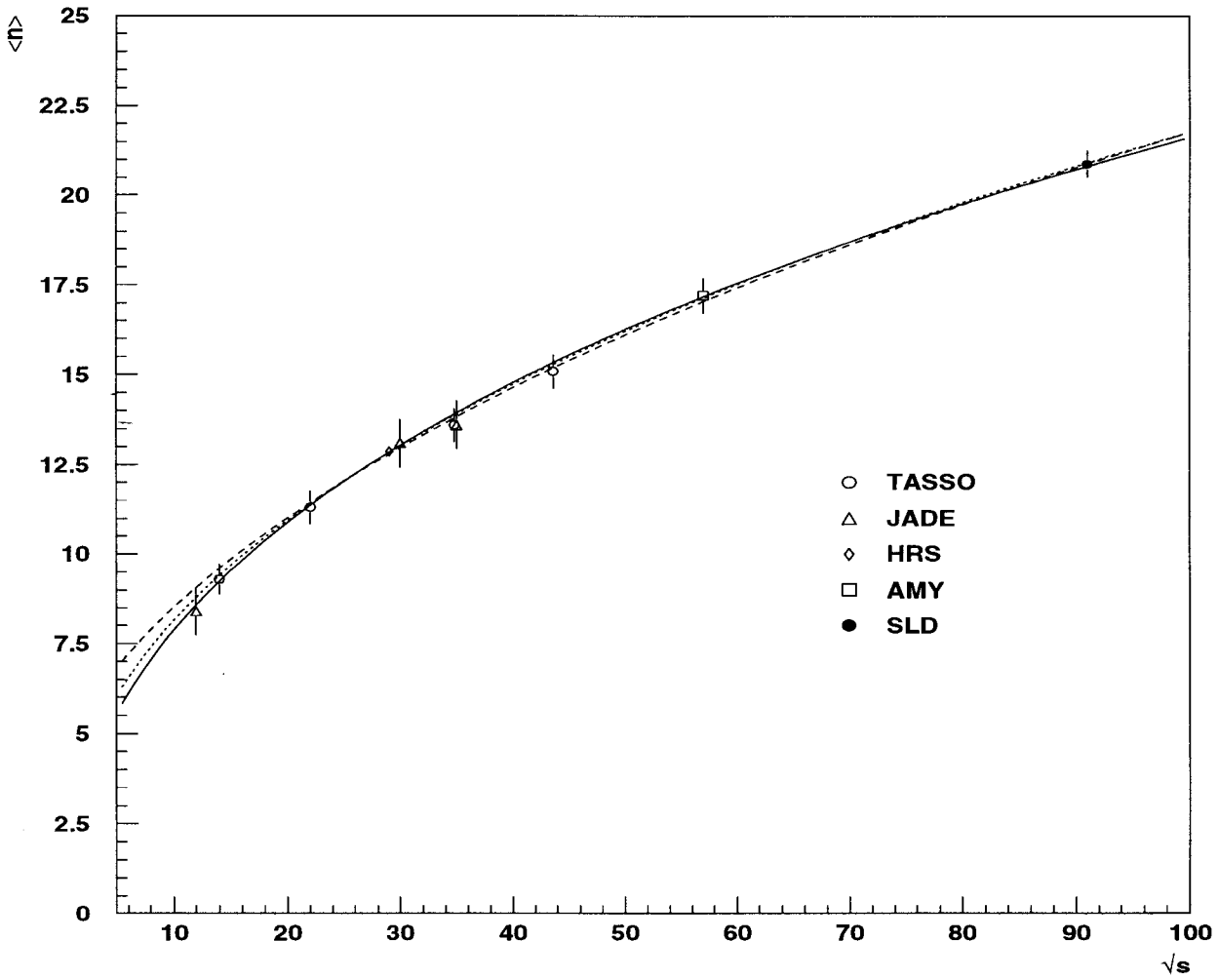

Figure 6.5: The energy dependence of the average charged particle multiplicity measured in e^+e^- interactions. The dotted line represents the fit to a phenomenological model, dashed line the prediction from leading-log perturbative QCD, and solid line the prediction from next-to-leading order perturbative QCD.

n	No. of events	n	No. of events
5	93	26	1024
6	212	27	759
7	245	28	643
8	557	29	439
9	821	30	410
10	1378	31	259
11	1812	32	196
12	2330	33	137
13	2753	34	97
14	3234	35	81
15	3592	36	43
16	3657	37	32
17	3488	38	25
18	3480	39	16
19	3382	40	11
20	2933	41	6
21	2653	42	3
22	2281	43	0
23	1878	44	1
24	1662	45	1
25	1311	46	1

Table 6.2: Uncorrected charged particle multiplicity distribution.

energy. One of the simplest relations

$$< n >= a \cdot s^b, \tag{6.6}$$

was predicted by the fireball and hydrodynamical models for hadron-hadron interactions [54]. The fit to the data gave $a = 3.047 \pm 0.284$ and $b = 0.214 \pm 0.013$, with $\chi^2/NDF = 1.44/8$.

A perturbative QCD prediction based on the leading-log approximation relates $< n >$ to energy by [55]

$$< n >= a + b \cdot \exp(c \cdot \sqrt{\ln(s/Q_0^2)}), \tag{6.7}$$

where Q_0^2 is a QCD cut-off parameter that corresponds to the termination of the parton showering. We fitted this function to the data (given $Q_0^2 = 1$ GeV), yielding $a = 4.822 \pm 0.323$, $b = 0.093 \pm 0.012$ and $c = 1.716 \pm 0.043$, with $\chi^2/NDF = 2.965/7$.

Including next-to-leading order corrections, perturbative QCD predicts an energy dependence of the form [56]

$$< n >= a \cdot \alpha_s^b \cdot \exp(c/\sqrt{\alpha_s})(1 + O(\sqrt{\alpha_s})), \tag{6.8}$$

Neglecting the $O(\sqrt{\alpha_s})$ term, there are only two free parameters left: the normalization constant a which can't be calculated perturbatively, and a scale parameter Λ which is associated with the running coupling constant by (referring to Chapter 2)

$$\frac{\alpha_s}{4\pi} = \frac{1}{\beta_0 \ln(s/\Lambda^2)}(1 - \frac{\beta_1 \ln\ln(s/\Lambda^2)}{\beta_0^2 \ln(s/\Lambda^2)}). \tag{6.9}$$

The rest of the parameters are fixed within QCD; for five active flavours $\beta_0 = 11 - 2N_f/3 = 7.67$, $\beta_1 = 102 - 38N_f/3 = 38.67$, $b = 1/4 + (10N_f)/(27\beta_0) = 0.49$ and $c = \sqrt{96\pi}/\beta_0 = 2.27$ [57]. The fit to the data is reasonable, with $\chi^2/NDF = 1.260/8$. The fitted values of the two free parameters are $a = 0.060 \pm 0.008$ and $\Lambda = 0.115 \pm 0.033$ GeV. Figure 6.5 shows how the fits compare to data. It seems that all can describe the data. Obviously, more sensitive quantities are needed in order to exclude some models. The average multiplicities computed from the JETSET at various energies were also compared with data and an overall agreement was found.

6.4.2 Second Binomial Moment R_2

We compared our second binomial moment R_2 with the existing data measured at the same center-of-mass energy (see Table 6.7). Within the errors, the agreement is good. Figure 6.6 shows a comparison with the data measured at lower energies[59, 60]. The perturbative QCD calculation predicts R_2 as a function of energy to follow [58]

$$R_2 = \frac{11}{8}(1 - k\sqrt{\alpha_s}) \tag{6.10}$$

with $k = 0.55$ for five active flavors. The comparisons with both leading and next-to-leading order QCD predictions are also shown in Fig. 6.6. For next-to-leading order QCD, the running coupling constant α_s in Eq. 6.10 was calculated from Eq. 6.9 in which Λ was set to be 0.115 GeV (obtained from the fit to the energy dependence of the average multiplicity).

It appears that the next-to-leading order lies closer to data and shows a similar weak energy dependence as the data while the prediction from the leading order is far above the data and has no energy dependence at all. The JETSET model again provides a good description of the data as shown in Fig. 6.6. We therefore suspect that even higher corrections or non-perturbative effects are needed in order to explain the higher order moments properties. The issues of higher order moments will be addressed in the next chapter.

6.4.3 Shape of the Multiplicity Distribution

A number of parameterizations based on phenomenological models have been proposed to describe the shape of the charged multiplicity distribution [61]. One of the simplest distributions is the Poisson distribution, which has been found not to describe the data, implying non-random production mechanisms.

One distribution which provides a good parameterization of much experimental data at lower energies is the negative binomial distribution (NBD),

$$P_n(\langle n\rangle, k) = \frac{k(k+1)...(k+n-1)}{n!}\left(\frac{\langle n\rangle}{\langle n\rangle + k}\right)^n\left(\frac{k}{\langle n\rangle + k}\right)^k, \qquad (6.11)$$

where $< n >$ and k are two free parameters. There are several phenomenological models leading to a NBD distribution [61]. For example, a model in which the interaction produces a number of objects, corresponding to the number of partons in a QCD cascade, each of which decays into a random number of particles, predicts such a NBD type of distribution [62]. In fact, the leading moments predicted in next-to-leading order QCD were found to be very close to that of a NBD [58]. We have fitted the NBD to our corrected multiplicity distributions. The results are shown in Fig. 6.7. The normalized residuals between the data points and the fit are also shown in the

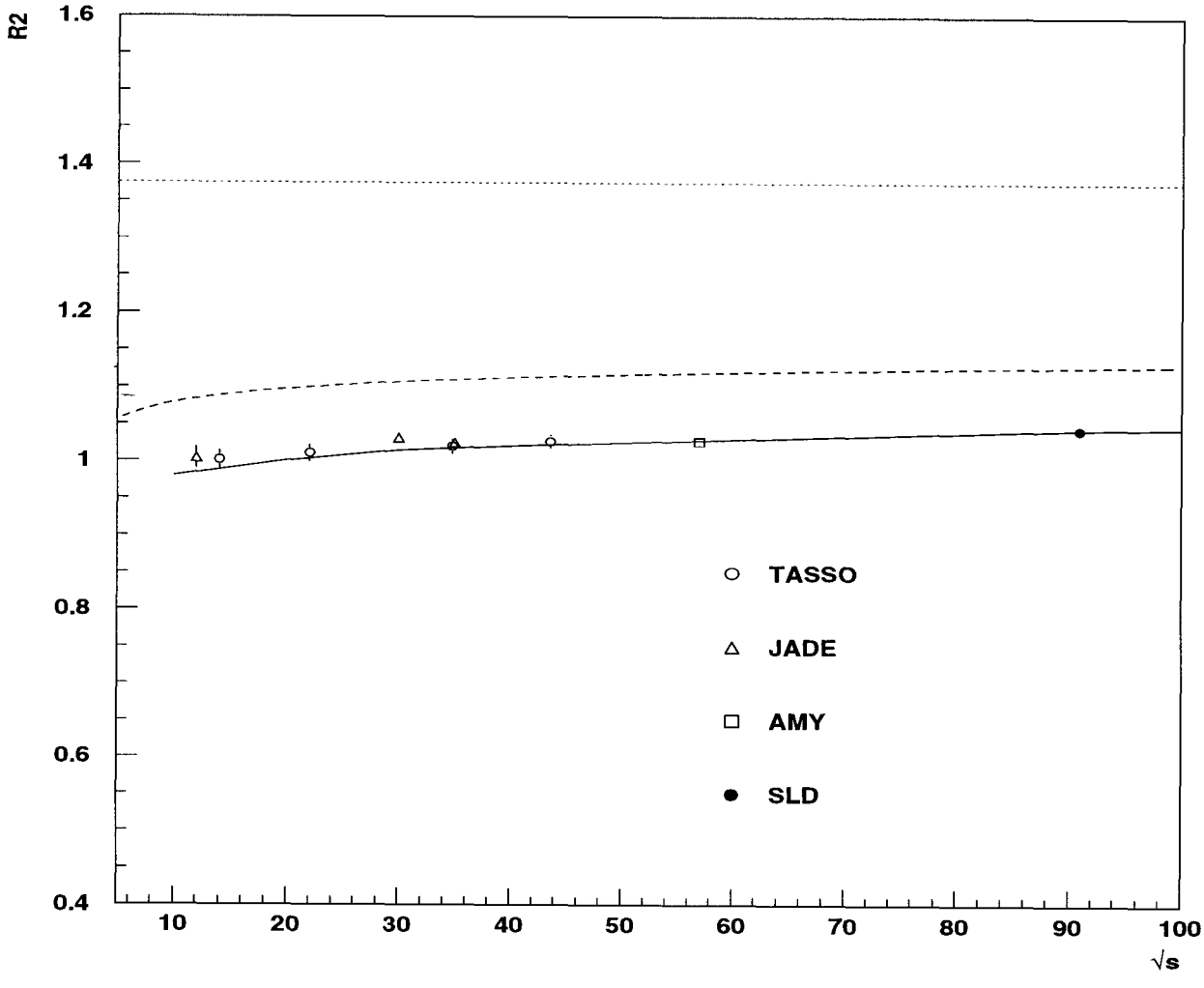

Figure 6.6: The energy dependence of R_2. The dotted line represents the prediction from leading order perturbative QCD, the dashed line for next-to-leading, and the solid line for JETSET.

figure. The fits yielded parameter values of $k = 24.86 \pm 0.93$ and $\langle n \rangle = 20.64 \pm 0.10$, with $\chi^2/NDF = 68.0/24$.

Recently the log-normal distribution (LND) has been introduced as a parameterization of multiplicity distributions in high energy interactions [63]. This distribution is particularly interesting and has a very appealing physical interpretation in terms of current models for the dynamics of mutiparticle production. The LND is obtained for a cascade-like process where the probability of each step multiplies the probability of the previous outcome (a scale-invariant stochastic branching process). This gives a natural connection to state-of-the art models for multiparticle production involving QCD parton cascades and hadronization. The LND has the form of

$$P_n(\mu, \sigma, c) = \int_n^{n+1} \frac{N}{n' + c} \exp\left(-\frac{(\ln(n' + c) - \mu)^2}{2\sigma^2}\right) dn', \tag{6.12}$$

where

$$\sigma^2 = \ln(1 + \frac{d^2}{(\overline{n} + c)^2}), \qquad \mu = \ln \frac{(\overline{n} + d)^2}{\sqrt{d^2 + (\overline{n} + c)^2}}. \tag{6.13}$$

In the limit $\mu - \ln c \gg \sigma$ the new parameters $\overline{n}$ and d can be identified as the mean and the dispersion of the distribution. We have fitted the LND to our corrected multiplicity distribution (see Fig. 6.8). The fit yielded parameter values of $\overline{n} = 20.99 \pm 0.10$, $d = 6.11 \pm 0.05$ and $c = 11.74 \pm 1.18$, with $\chi^2/NDF = 30.5/23$. As it is seen, the LND offers better description of data than NBD (see residual plots). The prediction from the JETSET was found in good agreement with data (not shown in the figure).

6.5 Conclusion

We measured the charged-particle multiplicity distribution in hadronic Z^0 decays. The average multiplicity and the second binomial moment were found to be $< n >= 20.63 \pm 0.01 \pm 0.34$ and $R_2 = 1.0429 \pm 0.0003 \pm 0.0034$, which are in good agreement with the data measured at the same center-of-mass energy $\sqrt{s} = 91$ GeV. We have studied the energy dependences of the average multiplicity, and noticed that both leading-log and next-to-leading order pertubative QCD can describe the data.

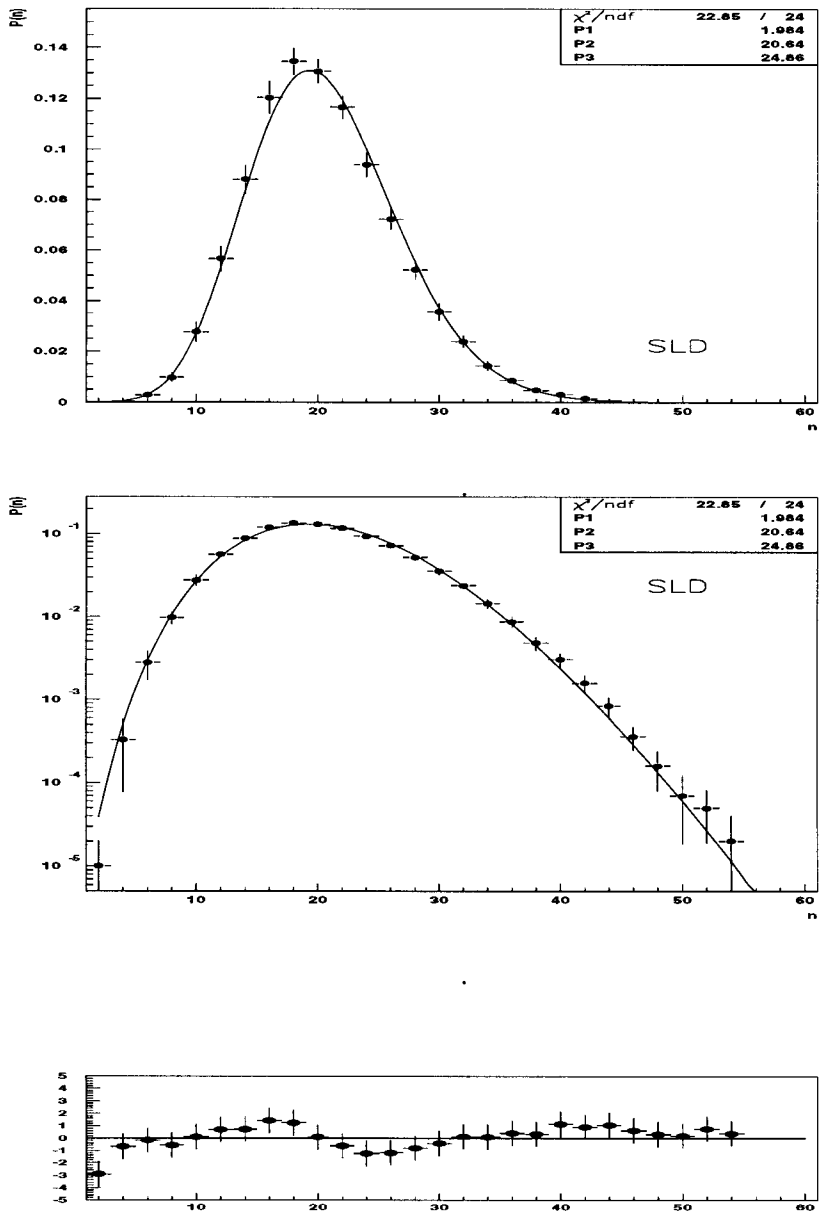

Figure 6.7: The corrected charged particle multiplicity distribution (both in linear and logarithmic scale). The solid line represents the fitted negative binomial distribution. The bottom figure shows the normalized residuals.

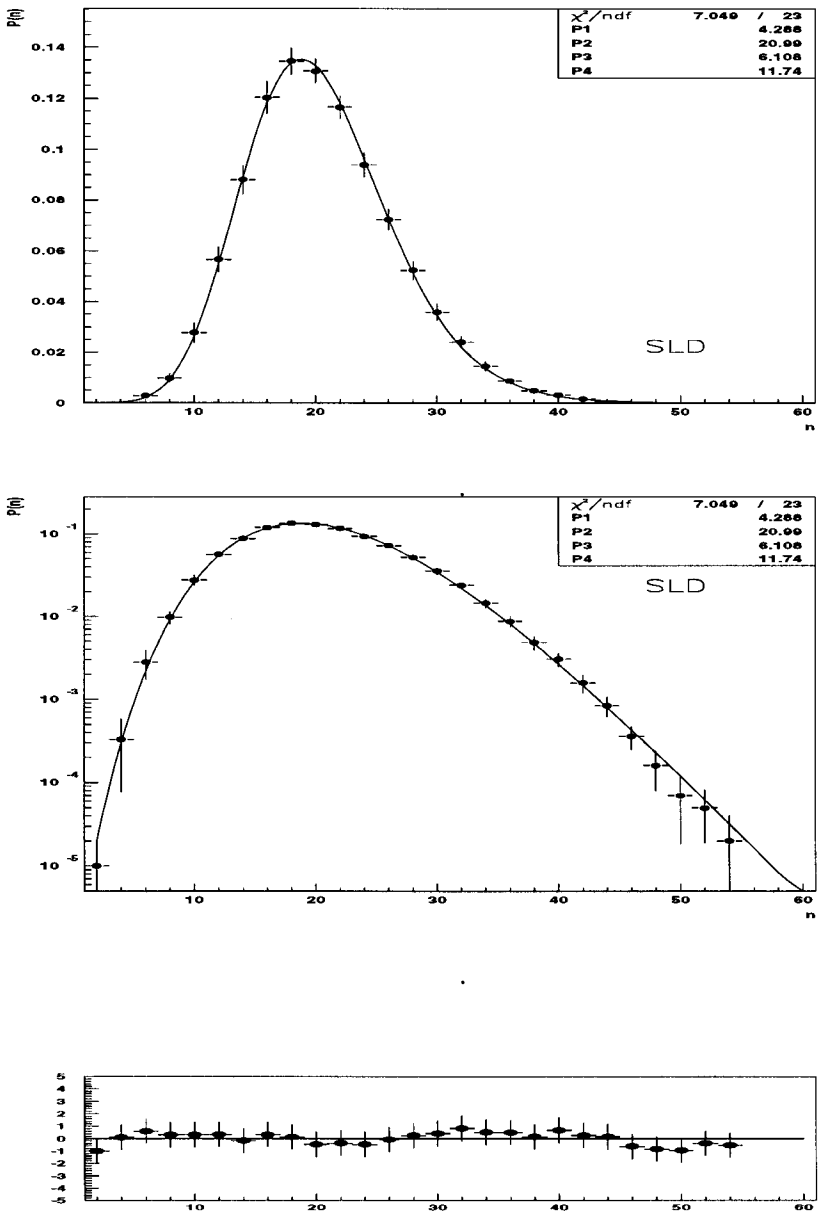

Figure 6.8: The corrected charged particle multiplicity distribution (both in linear and logarithmic scale). The solid line represents the fitted log-normal distribution. The bottom figure shows the normalized residuals.

However, we found that next-to-leading order pertubative QCD provides a better description of the energy dependence of the moment R_2. The overall properties of data can be reproduced reasonably well by the JETSET. The shape of the multiplicity distribution was fitted to two phenomenological parameterizations, the negative binomial distribution and the log-normal distribution. We found that the data are well-described by the log-normal distribution, which is predicted by a model in which the particles result from a scale-invariant stochastic branching process.

n	$p(n)$
2	$(0.00001 \pm 0.00001)^a$
4	$(0.00031 \pm 0.00025)^a$
6	$0.00263 \pm 0.00020 \pm 0.00097$
8	$0.00886 \pm 0.00046 \pm 0.00142$
10	$0.02466 \pm 0.00088 \pm 0.00356$
12	$0.05143 \pm 0.00135 \pm 0.00434$
14	$0.08207 \pm 0.00177 \pm 0.00484$
16	$0.11489 \pm 0.00221 \pm 0.00518$
18	$0.13124 \pm 0.00241 \pm 0.00324$
20	$0.13024 \pm 0.00239 \pm 0.00238$
22	$0.11873 \pm 0.00225 \pm 0.00258$
24	$0.09740 \pm 0.00198 \pm 0.00347$
26	$0.07616 \pm 0.00170 \pm 0.00301$
28	$0.05615 \pm 0.00139 \pm 0.00303$
30	$0.03909 \pm 0.00111 \pm 0.00283$
32	$0.02659 \pm 0.00089 \pm 0.00177$
34	$0.01622 \pm 0.00064 \pm 0.00135$
36	$0.01005 \pm 0.00046 \pm 0.00110$
38	$0.00565 \pm 0.00029 \pm 0.00079$
40	$0.00369 \pm 0.00026 \pm 0.00044$
42	$0.00199 \pm 0.00018 \pm 0.00032$
44	$0.00109 \pm 0.00009 \pm 0.00019$
46	$0.00049 \pm 0.00005 \pm 0.00009$
48	$0.00028 \pm 0.00005 \pm 0.00007$
50	$0.00010 \pm 0.00001 \pm 0.00005$
52	$0.00005 \pm 0.00001 \pm 0.00003$
54	$0.00002 \pm 0.00000 \pm 0.00002$

Table 6.3: Corrected normalized charged particle multiplicity distribution. The first error is the statistical, the second the systematic. The entries for 2 and 4 were taken from JETSET 6.3.

Leading moments	
$< n >$	$20.63 \pm 0.01 \pm 0.34$
D	$6.29 \pm 0.01 \pm 0.16$
$< n > /D$	$3.32 \pm 0.01 \pm 0.06$
R_2	$1.0429 \pm 0.0003 \pm 0.0034$

Table 6.4: Leading moments of the charged particle multiplicity distribution. The first error is the statistical error, the second the systematic error on the result.

Contributions to the systematic uncertainty	
Tracking inefficiency	0.060
Stat. fluctuation in $M(n_g, n_o)$	0.011
Model dependence	0.001
Track and event selection	0.329
Correction dependence	0.020
Overall systematic uncertainty	0.340

Table 6.5: Contributions to the overall systematic error

Collaboration	$< n >$
SLD	$20.63 \pm 0.01 \pm 0.34$
DELPHI	$20.71 \pm 0.04 \pm 0.77$
ALEPH	$20.85 \pm 0.02 \pm 0.24$
OPAL	$21.40 \pm 0.02 \pm 0.43$
L3	20.70 ± 0.70
MARK II	$20.10 \pm 1.00 \pm 0.90$

Table 6.6: Average charged multiplicity and comparision with other data measured at the same center-of-mass energy.

Collaboration	R_2
SLD	$1.0429 \pm 0.0003 \pm 0.0034$
DELPHI	$1.0435 \pm 0.0006 \pm 0.0059$
ALEPH	$1.0444 \pm 0.0006 \pm 0.0032$
OPAL	$1.0451 \pm 0.0003 \pm 0.0032$

Table 6.7: The Second binomial moment R_2.

Chapter 7

Factorial and Cumulant Moments

7.1 Introduction

The problem of the proper description of multiplicity distributions in high energy inelastic processes is up to now among the most important ones in Quantum Chromodynamics (QCD). QCD has been known to provide natural explanations of many features of multiplicity distribution, such as KNO-scaling [64, 65]. However, the distributions predicted by lowest order perturbation theory are much wider than those observed experimentally [66]. Efforts have been devoted to include higher-order perturbative corrections [67, 68, 69], which improved the agreement with experiment by reducing the width of the theoretical distribution.

One approach toward quantitative comparison of theory and experiment is provided by the study of the moments of the multiplicity distribution, and these moments can be calculated by perturbative QCD [67]. It appears that the higher order moments reveal more detailed features of the multiplicity distribution and offer more sensitive tests of QCD. The ratio of cumulant to factorial moments, $H_q = K_q/F_q$, has recently been proposed [70] as a new measure of multiplicity distributions. In this chapter we present a study of the ratio of cumulant to factorial moments of the charged particle multiplicity distribution in hadronic events from Z^0 decays. In the next section, the definition of moments will be introduced. The prediction of perturbative QCD will be briefly described in section 3. The measurement of the ratio of

cumulant to factorial moments, and the comparison with QCD will be presented in section 4, followed by a conclusion in section 5.

7.2 Factorial and Cumulant Moments

The factorial moment of rank q, F_q, is defined as

$$F_q \equiv \frac{<n(n-1)...(n-q+1)>}{<n>^q} = \frac{\sum_n n(n-1)...(n-q+1)P(n)}{(\sum_n nP(n))^q}, \tag{7.1}$$

where $P(n)$ is the multiplicity distribution, and $<n>$ is the average multiplicity in the event sample. The cumulant moments K_q are related to F_q by [72]

$$F_q = \sum_{m=0}^{q-1} C_{q-1}^m K_{q-m} F_m. \tag{7.2}$$

Here $C_{q-1}^m = \frac{(q-1)!}{m!(q-m-1)!}$ are the binomial coefficients, and $F_0 = F_1 = K_1 = 1$. Eq. 7.2 allows one to solve for the K_q in an iterative way. Thus, F_q, K_q, and hence the ratio H_q can be determined from the multiplicity distribution $P(n)$.

Theoretically, these moments can be easily calculated if the generating function of the multiplicity distribution is known. The generating function $G(z)$ is defined as

$$G(z) = \sum_{n=0}^{\infty} P(n)(1+z)^n, \tag{7.3}$$

consequently its inverse gives the multiplicity distribution

$$P(n) = \frac{1}{n!} \frac{d^n G(z)}{dz^n}|_{z=-1}. \tag{7.4}$$

The factorial and cumulant moments are thus expressed in terms of $G(z)$ by

$$F_q = \frac{1}{<n>^q} \frac{d^q G(z)}{dz^q}|_{z=0}, \tag{7.5}$$

$$K_q = \frac{1}{<n>^q} \frac{d^q \ln G(z)}{dz^q}|_{z=0}. \tag{7.6}$$

The recurrence relation between F_q and K_q in Eq. 7.2 was indeed derived from Eq. 7.5 and Eq. 7.6 (see [72]).

Some phenomenological models of particle production have been examined to demonstrate the sensitivity of H_q [71, 72]. The simplest one is the Poisson distribution

$$P(n) = \frac{< n >^n}{n!} e^{-<n>}, \tag{7.7}$$

with its generating function given by

$$G(z) = e^{<n>z}. \tag{7.8}$$

From Eq. 7.5 and Eq. 7.6, one has

$$F_q = 1, \quad K_q = \delta_{q1}, \tag{7.9}$$

and thus

$$H_q = \delta_{q1} = \begin{cases} 1 & \text{for } q = 1 \\ 0 & \text{for } q \neq 1 \end{cases} \tag{7.10}$$

For the negative binomial distribution (see Eq. 6.11) its generating function is

$$G(z) = (1 - \frac{z < n >)}{k})^{-k}, \tag{7.11}$$

which gives rise to

$$H_q \sim q^{-k}, \tag{7.12}$$

where k is the NBD parameter. As shown above, the phenomenological distributions differ remarkably in their moment structures: for the PD, H_q is identically equal to zero except at $q = 1$; for the NBD, H_q is always positive and falls as $H_q \sim q^{-k}$.

7.3 Perturbative QCD Prediction

In perturbative QCD, the moments of the parton multiplicity distribution have been calculated [70, 71, 72, 73] up to next-to-next-to leading order within the framework of gluodynamics [72, 74]. While the leading double logarithmic approximation (DLA) predicts that the ratio of cumulant to factorial moments H_q monotonically decreases to zero as the function of rank q

$$H_q \sim q^{-2}, \tag{7.13}$$

including the higher order corrections introduces additional features. For instance, next-to-leading correction (NLA) gives

$$H_q \sim h_2\gamma_0^2 + \frac{1}{q^2}[1 - 2h_1\gamma_0 q + h_1\gamma_0(1 - h_1\gamma_0 q)]. \tag{7.14}$$

For this case the ratio H_q falls rapidly at small q and reaches a minimum at the rank

$$q_{min} = \frac{1}{h_1\gamma_0} + \frac{1}{2} + O(\gamma_0) \sim 5 \tag{7.15}$$

with a very small value at the minimum

$$H_{qmin} = (h_2 - h_1^2)\gamma_0^2 + O(r_0^4), \tag{7.16}$$

and then increases approaching an asymptotic value $h_2\gamma_0^2$. Here $r_0^2 = 2N_c\alpha_s/\pi$, α_s is the QCD coupling constant, $N_c(= 3)$ is the number of colors; and h_1 and h_2 are two constants introduced in the next-to-leading correction. It is clearly seen that Eq. 7.14 follows the DLA prediction when h_1 and h_2 are set to be zero. Extending to next-to-next-to-leading order corrections (NNLA), it is predicted that this minimum is negative and is followed by quasi-oscillations about zero. These predictions are illustrated in Fig. 7.1. The vertical scale and relative normalizations in the plot are arbitrary. It should be noted that the current theoretical predictions have not taken confinement into account; therefore, detailed quantitative comparisons with experiment are unlikely to be successful [70]. Nevertheless, it is interesting to investigate if the predicted features can be observed experimentally in final state particles.

7.4 Experimental Analysis

The corrected charged particle multiplicity distribution $P(n)$ as presented in the previous chapter was employed to calculate the moments. The factorial moments F_q, cumulant moments K_q, and their ratio H_q were calculated up to rank $q = 17$ according to Eqs. 7.1 and 7.2, and listed in Table 7.1. H_q as a function of the moment rank q is presented in Fig. 7.2. It can be seen that H_q falls rapidly at the lower ranks (see the inset of the figure) and reaches a negative minimum at $q \sim 5$. For increasing q, H_q exhibits a quasi-oscillatory behavior about zero. The statistical and systematic errors

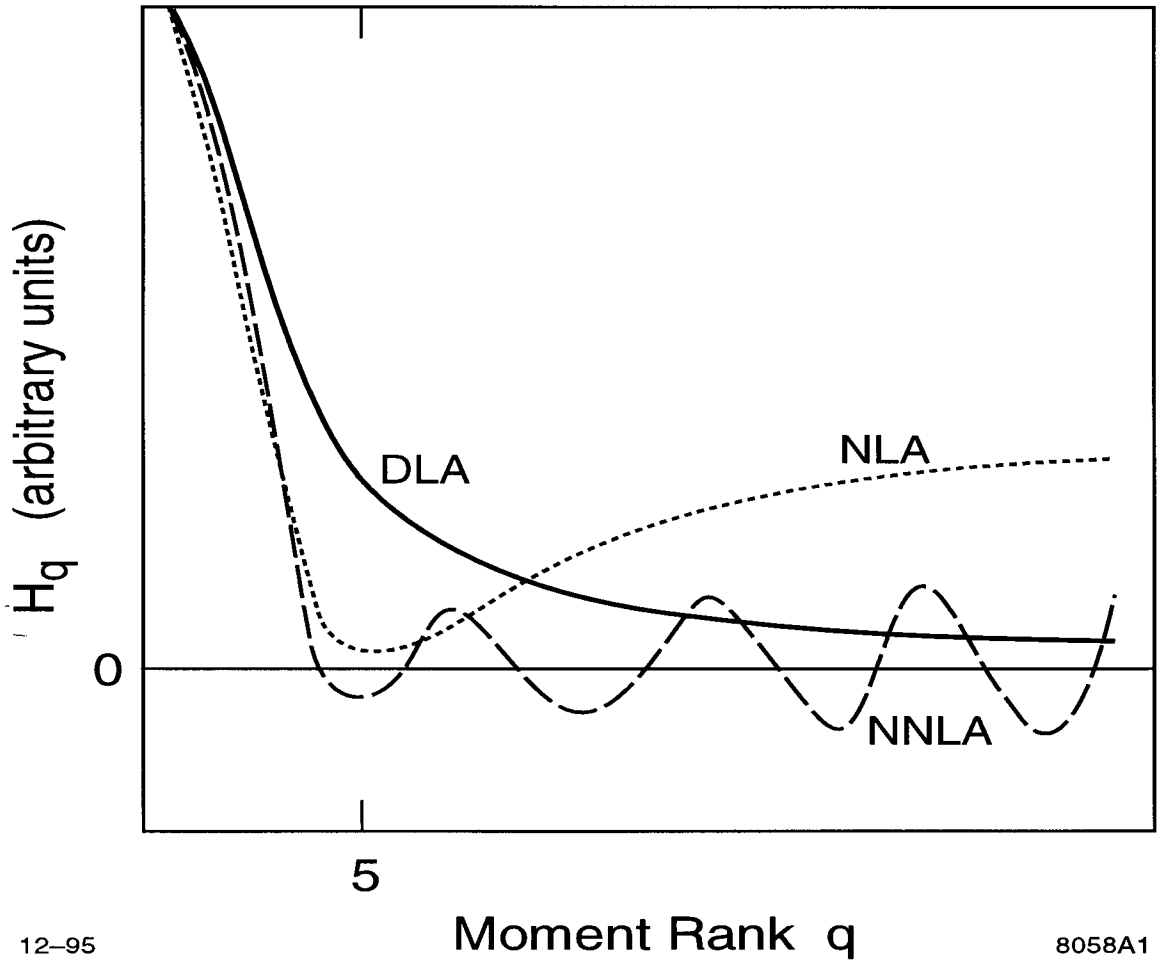

Figure 7.1: Functional form of perturbative QCD predictions of the ratio H_q of cumulant to factorial moments in the leading double-logarithm (solid line), next-to-leading-logarithm (dotted line) and next-to-next-to-leading-logarithm (dashed line) approximations. The vertical scale and relative normalizations are arbitrary.

are strongly correlated between ranks, which will be discussed below. These observed qualitative features are in good agreement with the predictions from higher-order perturbative QCD as described in section 3, and are clearly inconsistent with the leading double logarithmic approximation (DLA) which predicts H_q monotonically decreasing to zero as $H_q \sim q^{-2}$.

Table 7.1: Factorial moments F_q, cumulant moments K_q, and their ratio H_q.

q	F_q	K_q	H_q
2	1.042857	4.2856593E-02	4.1095383E-02
3	1.134744	6.1743488E-03	5.4411818E-03
4	1.288011	6.6368422E-04	5.1527849E-04
5	1.523203	-6.2110345E-04	-4.0776140E-04
6	1.872444	-6.3634361E-04	-3.3984645E-04
7	2.384605	-3.3330912E-04	-1.3977542E-04
8	3.132839	2.5401587E-05	8.1081689E-06
9	4.225152	3.8649960E-04	9.1475915E-05
10	5.818618	4.8659067E-04	8.3626503E-05
11	8.137637	7.8584257E-05	9.6568883E-06
12	11.49593	-7.6402142E-04	-6.6460183E-05
13	16.32076	-1.3480565E-03	-8.2597631E-05
14	23.17597	-4.0817657E-04	-1.7612059E-05
15	32.77740	2.9394717E-03	8.9679830E-05
16	45.99130	6.8938094E-03	1.4989378E-04
17	63.80269	3.9107543E-03	6.1294500E-05

7.4.1 Statistical Effects

Statistical effects on the results were studied from a set of Monte Carlo samples of the same statistical size as the data. For each H_q the standard deviation in these samples was taken as the statistical error, and is listed in Table 7.2. In each case H_q exhibited the same behavior as those calculated from the data, although the value of H_5 and the apparent phase of the quasi-oscillation for $q \geq 8$ were found to be sensitive to statistical fluctuations. We investigated the possibility that the observed features might result from a statistical fluctuation by generating 10,000 multiplicity distributions according to the Poisson and negative-binomial distributions with the same mean value as our corrected multiplicity distribution. In no case did any sample

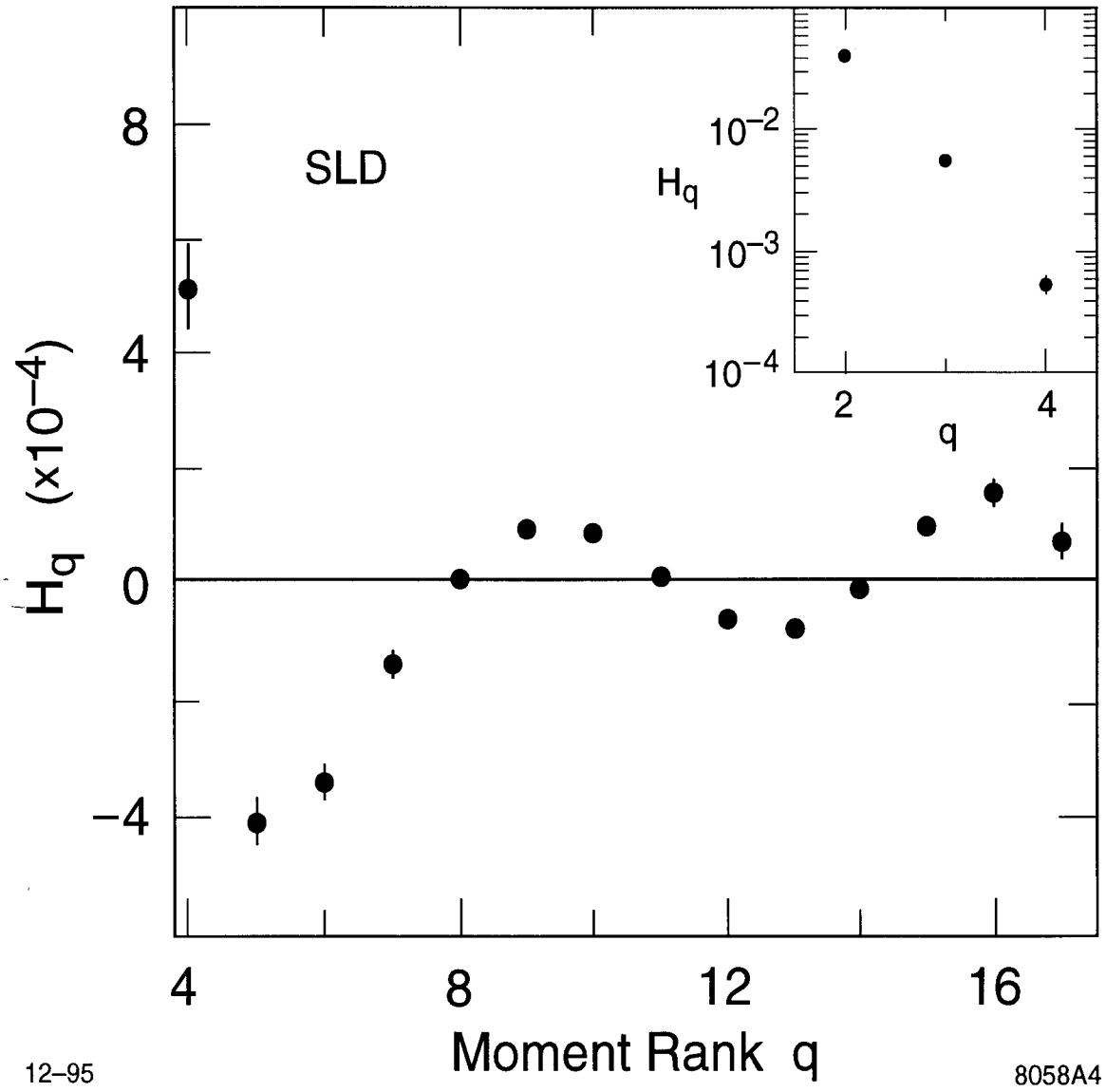

Figure 7.2: Ratio of cumulant to factorial moments, H_q, as a function of the moment rank q. The error bars are statistical and are strongly correlated between ranks.

exhibit either a minimum near q=5 or quasi-oscillations at higher q.

Table 7.2: H_q and statistical uncertainties.

q	H_q	Stat. Error
2	4.110E-02	2.962E-04
3	5.441E-03	1.393E-04
4	5.153E-04	7.370E-05
5	-4.078E-04	3.983E-05
6	-3.399E-04	2.774E-05
7	-1.398E-04	1.972E-05
8	8.108E-06	1.371E-05
9	9.148E-05	1.184E-05
10	8.363E-05	1.048E-05
11	9.657E-06	7.706E-06
12	-6.646E-05	9.999E-06
13	-8.260E-05	9.389E-06
14	-1.761E-05	9.650E-06
15	8.968E-05	1.585E-05
16	1.499E-04	1.925E-05
17	6.130E-05	2.617E-05

7.4.2 Systematic Effects

The contributions to the experimental systematic uncertainties were examined extensively. An important issue is the simulation of the track reconstruction efficiency of the detector. The H_q were found to be sensitive to the global efficiency, which was tuned in the simulation so that our average corrected multiplicity equaled the value measured in hadronic Z^0 decays [78]. The H_q resulting from a variation in the global efficiency of $\pm 1.7\%$, corresponding to the error on the measured average multiplicity, is shown in Fig. 7.3. There is an asymmetric effect on the value of H_5 and on the apparent phase of the quasi-oscillation. For each q the difference between the H_q with increased and decreased efficiency was assigned as a symmetric systematic

uncertainty.

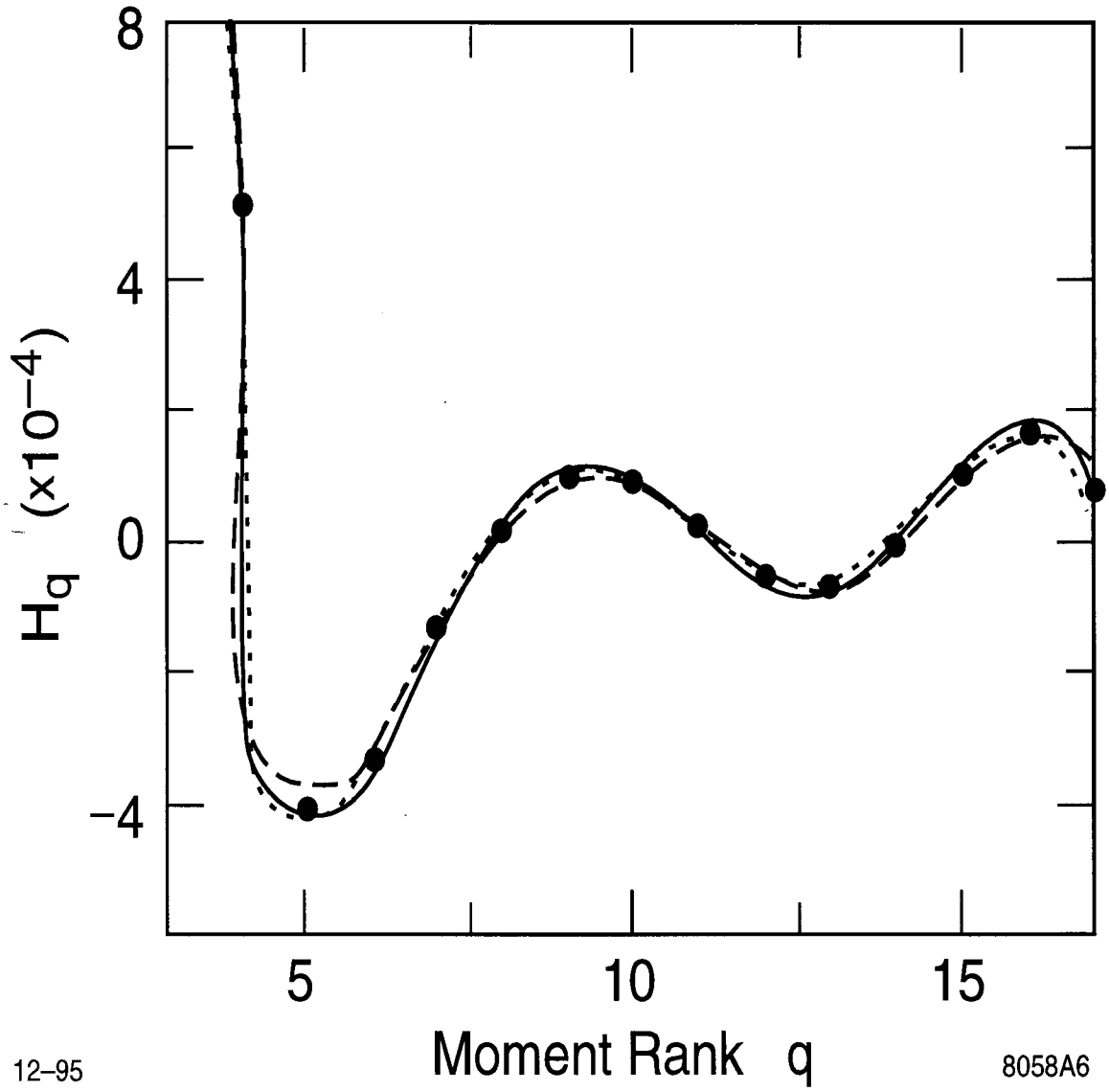

Figure 7.3: Examples of systematic effects on the H_q. The data points show the H_q derived using the standard correction. The dotted (dashed) line connects H_q values derived with an increase (decrease) of 1.7% in the simulated track reconstruction efficiency. The solid line connects H_q values derived using the unparameterized correction matrix.

It is important to consider the dependence of the track reconstruction efficiency on multiplicity. Our MC simulated efficiency is 91.5% for tracks crossing at least 40 of the 80 layers of the CDC, and is independent of n_g within $\pm 0.5\%$. Such a simulated efficiency is shown in Fig. 7.4. Varying the efficiency for $n_g > 20$ by $\pm 0.5\%$ caused a change of $\pm 4\%$ in H_5, and negligible changes for $q > 5$. This change was assigned as a systematic uncertainty.

Variation of the form of the parameterization of the correction matrix M was found to affect mainly the amplitude of the quasi-oscillations for $q \geq 8$. Application of the unparameterized version of the matrix $M(n_g, n_o)$ produced the largest such effect, which is shown in Fig. 7.3. This change was conservatively assigned as a symmetric systematic uncertainty in order to account for possible mismodeling of the far-off-diagonal elements of the matrix. The effect on the H_q of variations of the parameters of the three-Gaussian fits to M within their errors increases with increasing q, becoming the dominant uncertainty for $q \geq 16$.

The effects on the H_q of wide variations in the criteria for track and event selection were found to be small compared with those due to the above sources. The effect of including values of the multiplicity distribution at $n = 2$ and $n = 4$, taken from the JETSET model, in the calculation of the moments is also small. Varying the estimated level of non-hadronic background, which appears predominantly in the low-multiplicity bins, by $\pm 100\%$ produces a negligible change in the H_q.

The uncertainties from the above systematic sources were added in quadrature to derive a systematic error on each H_q, which is listed in Table 7.3.

In all of our studies there was a clear first minimum in H_q at $q = 5$ followed by quasi-oscillations for $q \geq 8$. The value of H_5 has a total uncertainty of $\pm 13\%$ that is strongly correlated with similar errors on H_6 and H_7 and with an uncertainty in the phase of the quasi-oscillation of ∓ 0.2 units of rank. There is an uncertainty on the amplitude of the quasi-oscillation of $\pm 15\%$ that is essentially independent of the other errors. From these studies we conclude that the steep decrease in H_q for $q < 5$, the negative minimum at $q = 5$, and the quasi-oscillation about zero for $q \geq 8$ are well-established features of the data.

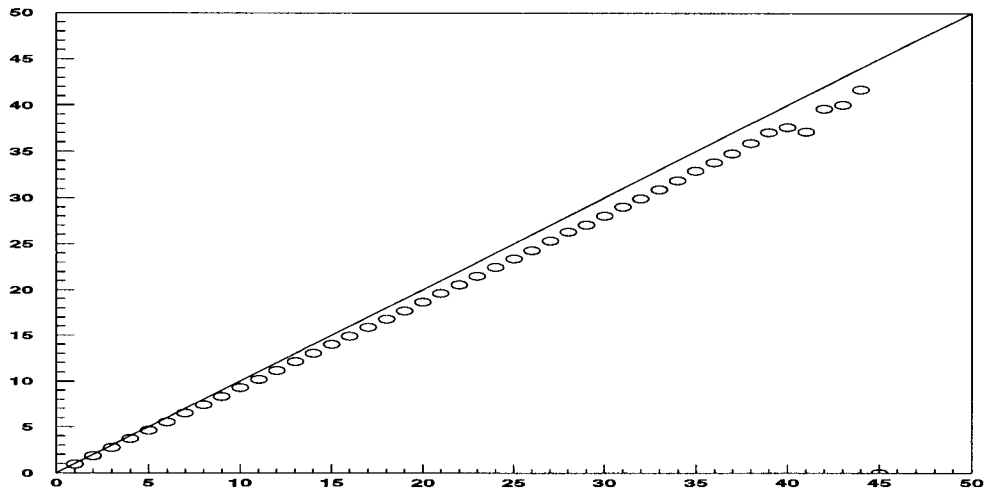

a. $< n_{recon} >$ as a function of n_{input}.

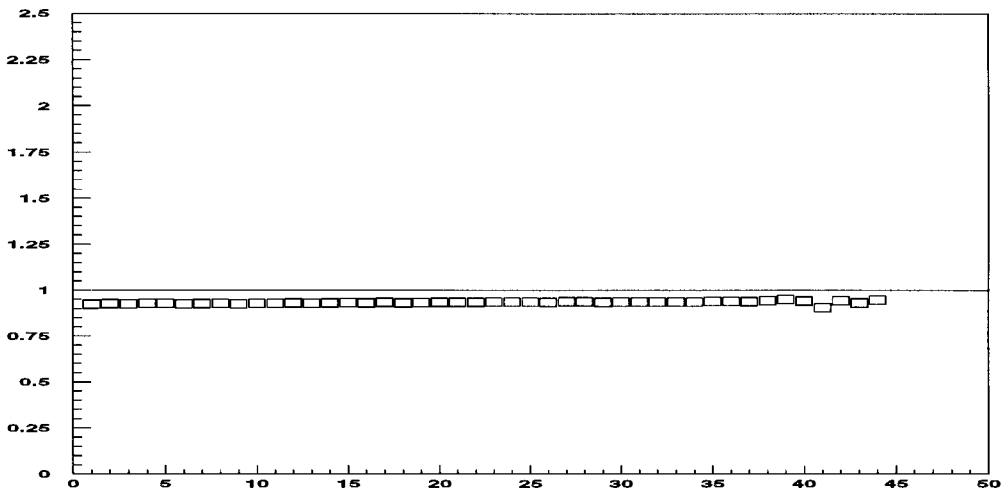

b. $eff(= \frac{<n_{recon}>}{n_{input}})$ as a function of n_{input}.

Figure 7.4: The dependence of the track reconstruction efficiency on multiplicity. n_{recon} denotes the number of tracks reconstructed, n_{input} the number of tracks entering theCDC.

Table 7.3: H_q and systematic uncertainties.

q	H_q	Syst. Error
2	4.110E-02	1.113E-03
3	5.441E-03	5.614E-04
4	5.153E-04	9.346E-05
5	-4.078E-04	5.061E-05
6	-3.399E-04	3.870E-05
7	-1.398E-04	3.175E-05
8	8.108E-06	9.736E-06
9	9.148E-05	1.563E-05
10	8.363E-05	1.863E-05
11	9.657E-06	8.988E-06
12	-6.646E-05	1.504E-05
13	-8.260E-05	2.125E-05
14	-1.761E-05	1.326E-05
15	8.968E-05	2.617E-05
16	1.499E-04	4.517E-05
17	6.130E-05	3.691E-05

7.4.3 Issue of Truncation

It was recently argued [79] that the truncation of the tail of the multiplicity distribution due to finite sample size could lead to quasi-oscillations in H_q which are similar to those observed in the data. We investigated this by observing the effect on H_q due to truncation of the tail of the best fitted NBD to our observed multiplicity distribution. The best fitted NBD is shown in Fig. 6.7, with fitted free parameters, $k = 24.86 \pm 0.93$, $\langle n \rangle = 20.64 \pm 0.10$. We notice that certain distortions appear only when the truncation happens at very low multiplicities. However, when the NBD was truncated at multiplicity values equal to or larger than the actual truncation of the experimental data, the observed distortions of H_q were found to be negligibly small.

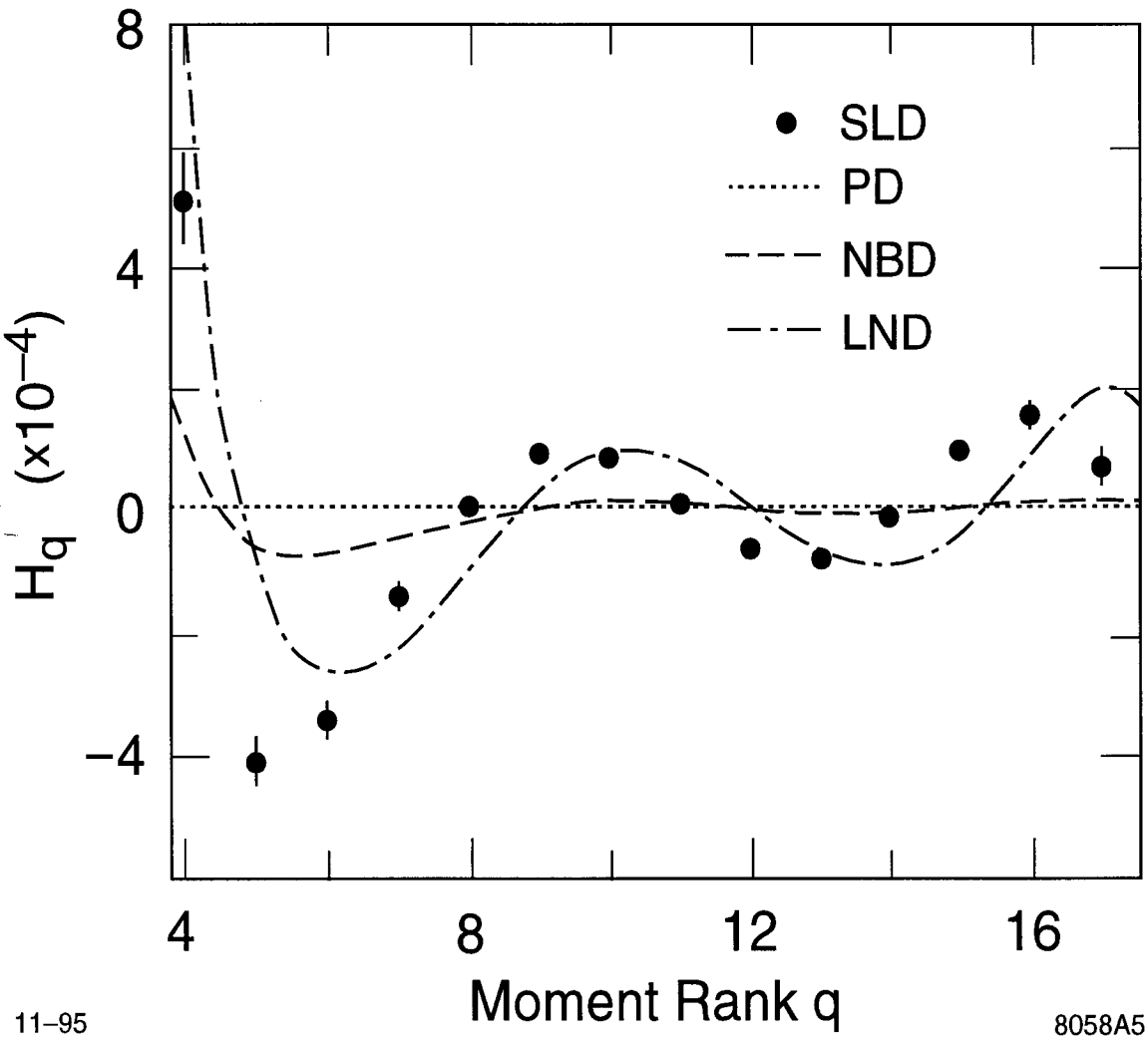

Figure 7.5: Comparison of the H_q measured in the data (dots) with the predictions of truncated Poisson (dotted line joining the values at different q), negative binomial (dashed line) and log-normal (dot-dashed line) distributions. The trucation is at the actual measured maximum multiplicity.

Similar results were obtained with the best fitted PD replacing the NBD. Figure 7.5

shows these results, in which both PD and NBD are inconsistent with the experimental data. We did the same analysis by truncating the best fitted LND, and found similar qualitative features to the data. However, the first minimum is smaller in amplitude and is at $q = 6$. The quasi-oscillation for $q \geq 8$ is displaced by about one unit from the data.

7.5 Conclusion

We have studied the ratio H_q of cumulant to factorial moments of the charged-particle multiplicity distribution in hadronic Z^0 decays. The results for H_q are summarized in Fig. 7.6. We find that H_q, as a function of the moment rank q, decreases sharply to a negative minimum at $q \sim 5$, followed by a sequence of quasi-oscillations. The observed qualitative features are in good agreement within statistical and systematic errors with the predictions from higher-order perturbative QCD calculations, excluding the leading double-logarithm approximation. The phenomenological PD and NBD distributions are clearly inconsistent with the data, while the log-normal distribution predicts features similar to those of the data, but does not describe the data in detail.

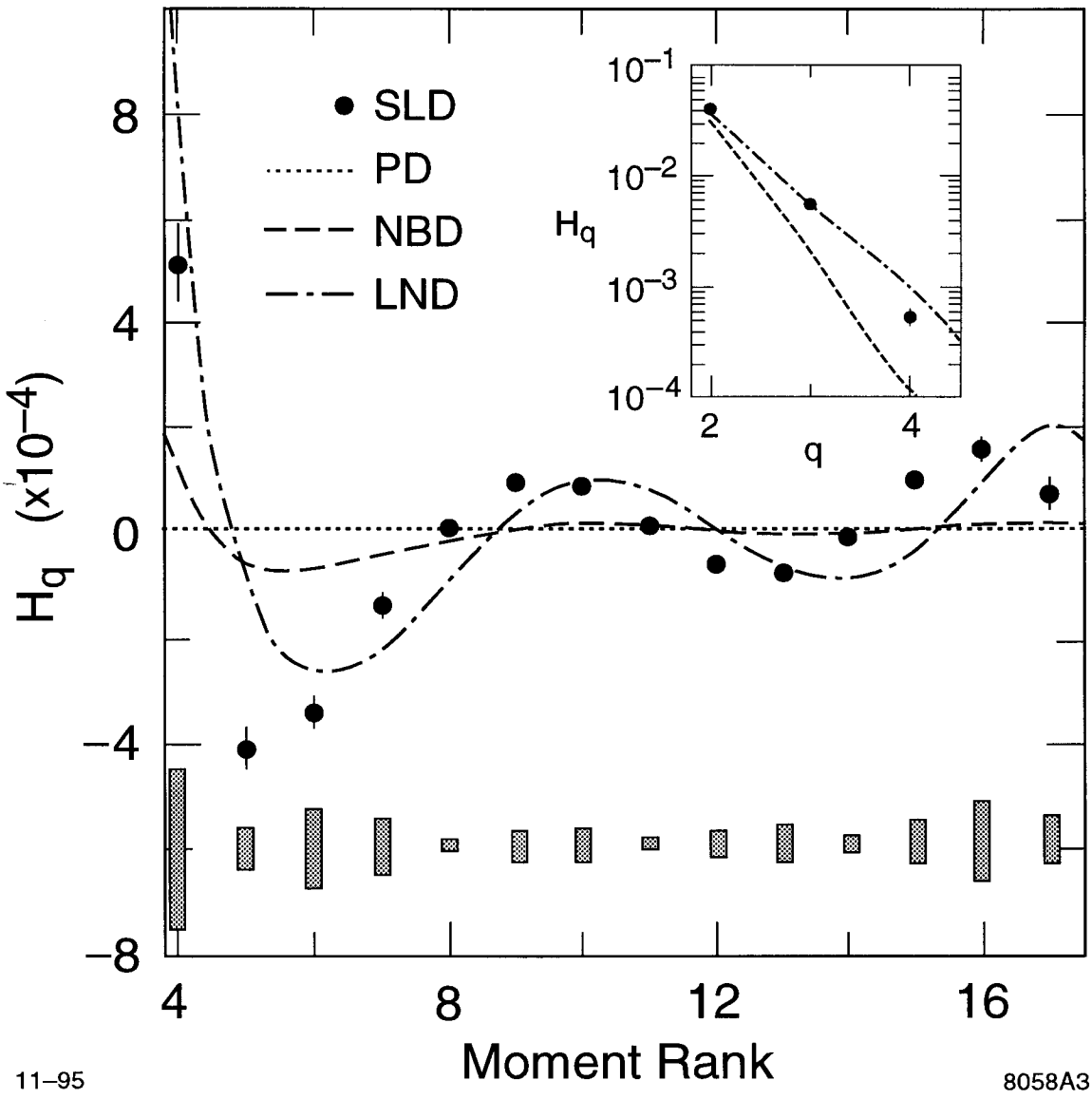

Figure 7.6: H_q as a function of the moment rank q. The shadowed bands indicate the systematic errors.

Chapter 8

Intermittency

8.1 Introduction

An important experimental feature in multiparticle production in high energy collisions is the presence of local density fluctuations [80, 81, 82, 83, 84], raising questions about whether they are of dynamical or simply statistical origin. To answer the questions, Bialas and Peschanski [85, 86] proposed to study the scaled factorial moment F_q as a function of phase space resolution δy.

Given the particle distribution in the rapidity interval (phase space) from $-Y/2$ to $Y/2$, the interval is divided into M equal bins of size $\delta y = Y/M$. The scaled factorial moment of rank q is then defined as [86]

$$F_q(M) = \frac{M^{q-1}}{< N >^q} < \sum_{m=1}^{M} n_m(n_m - 1)\cdots(n_m - q + 1) >, \tag{8.1}$$

with $N = \sum_{m=1}^{M} n_m$, and n_m being the charged particle multiplicity in bin m. The sum is over all bins, and angle brackets imply an average over events in the sample. Note that only bins containing q or more particles contribute to $F_q(M)$. Thus, the factorial moment of rank q for a resolution δy acts as a filter for selecting events with at least q particles in at least one bin. They are therefore highly sensitive to the events with large local density fluctuations. A well-known property as shown in [85, 86], is that $F_q(M)$ is independent of M (or δy) if the production of particles is random and uncorrelated. Thus, the observation of such a dependence would indicate the

presence of dynamical origin. Of particular interest is the case where the particles are produced in the self similar cascade mechanism. In this case, a power law dependence is expected [85, 86]

$$Fq \propto \delta y^{-\alpha_q}, \quad \alpha_q > 0. \tag{8.2}$$

This property is called 'intermittency' (for review, see [87, 88, 89]).

Evidence for intermittency has been collected in subsequent years in hadron-hadron and nucleus-nucleus collisions [90, 91, 92, 93, 94, 95]. The interest in these results is enhanced by the fact that the most common models are unable to reproduce the effect, inspiring some speculations of possible new mechanisms, such as a phase transition. In contrast, the data obtained in e^+e^- annihilation at LEP [96, 97, 98, 99] are in agreement with the QCD-based PS model, implying that the cascading mechanism is a natural candidate, since hadronic reaction mechanisms, such as phase transitions, are unlikely in this case. Self similar cascade is indeed expected in the $e^+e^- \rightarrow$ hadrons process, in which quark-gluon cascades appear quite naturally [102]. A number of effects, such as p_t, charge, multiplicity and space dimension dependence have been examined at LEP and other groups [98, 96, 100], adding further support to the self similar cascade mechanism and yielding some insights into the contributions to the growth of the factorial moment with increasing resolution. For a review, see [101]. In this chapter, we present our study by probing samples with different event shapes and various jet topologies. The results are compared with the Monte Carlo, a version we used through the previous chapters, i.e, a QCD-based PS JETSET event generator plus a detailed simulation of the SLD detector .

8.2 Analysis

Our analysis is performed in the rapidity phase space. Such a one dimensional study is believed to be more meaningful in revealing dynamical effect [104]. The rapidity is defined as

$$y = \frac{1}{2} \ln \frac{E + p_{\|}}{E - p_{\|}}, \tag{8.3}$$

with $p_{||}$ being the component of momentum along the event axis and the energy E calculated assuming the pion mass for all charged particles. The sphericity axis is chosen as the event axis in this analysis, and the sensitivity of the study to the choice of axis will be examined in the following. Figure 8.1 shows the rapidity distribution. The

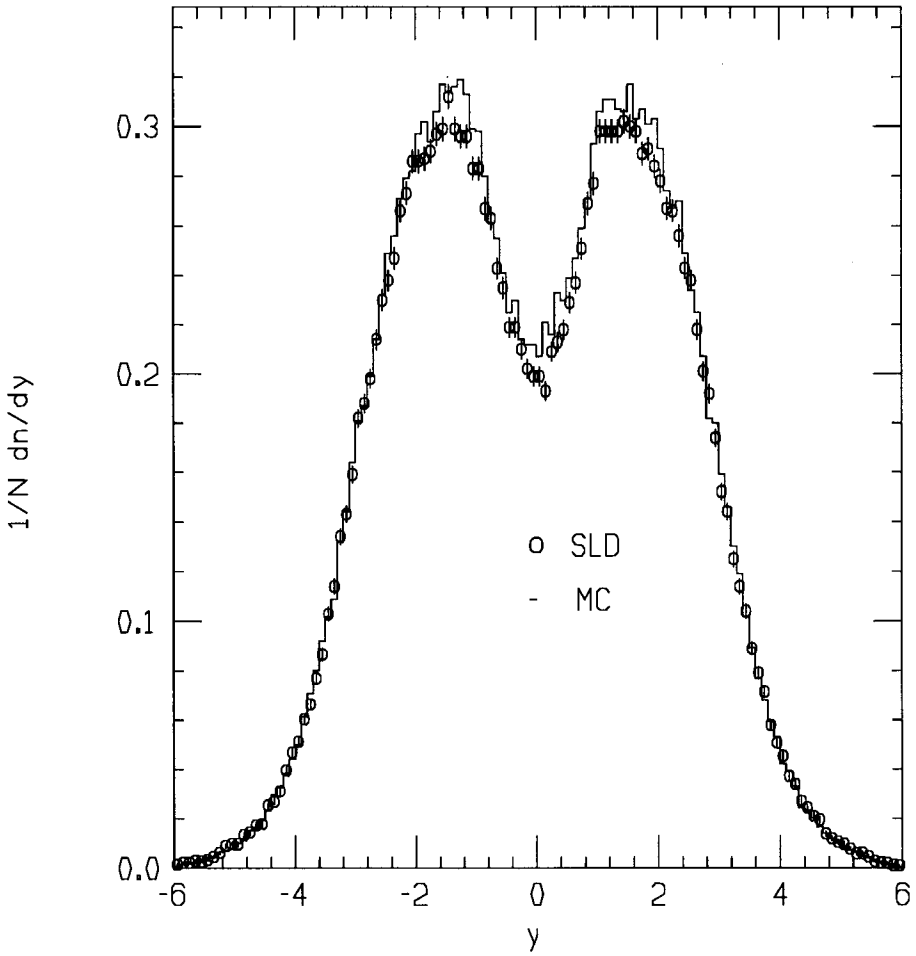

Figure 8.1: The rapidity distribution calculated with respect to the sphericity axis, and comparison with the Monte Carlo shown in the solid histogram.

distribution is well reproduced by the Monte Carlo as shown in the solid histogram. The average resolution in rapidity, Δy, on a single track was estimated by Monte Carlo to be around 0.02. We consider the central rapidity region ($|y| < 2$), where the density of particles is approximately uniform.

The scaled factorial moments of ranks from 2 to 5 at various resolutions were calculated from the selected hadronic event sample, according to the definition in Eq. 8.1. The dependence of the moments on the number M of the subdivisions of the rapidity interval $-2 < y < 2$ is shown in Fig. 8.2. It can be seen that the logarithms of the moments grow as a function of the logarithms of the number M, and then flatten off at $M > 10$ ($\delta y \sim 0.4$). The moments can saturate when the detector resolution limit is reached. This is not the case in our experiment since our detector resolution in y is around 0.02, less than the minimum bin size we used. Such a flattening at small resolutions was interpreted [104] as a running coupling effect. The Monte Carlo

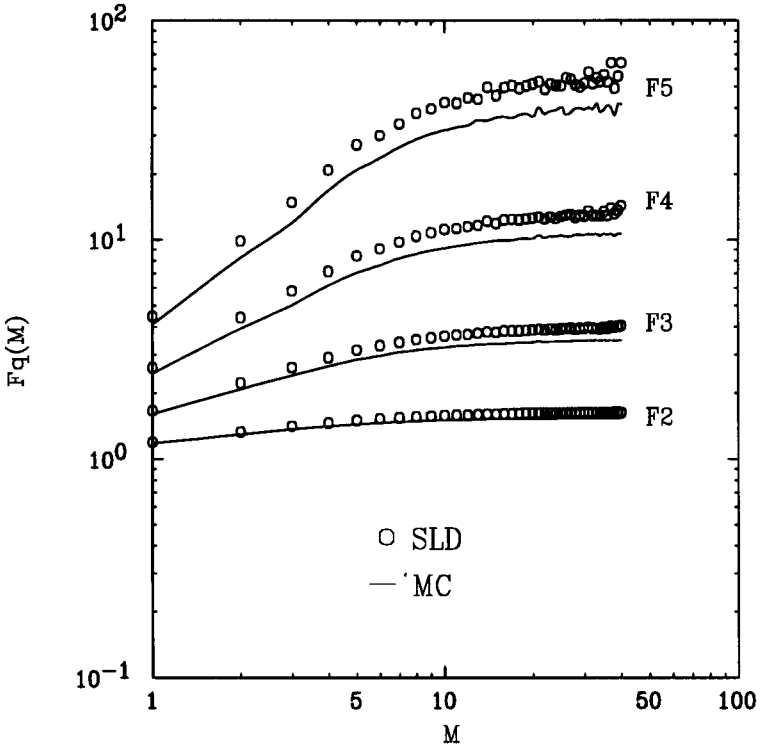

Figure 8.2: The dependence of the scaled factorial moments of rank 2,3,4,5 on the number M of the subdivisions of the rapidity interval ($|y| < 2$), plotted in bi-logarithmic scale. The solid curves represent the corresponding predictions from the Monte Carlo.

shows very similar behavior to the data, although some differences in amplitude can

be seen. Our result is compatible with the LEP experiments [96, 97, 98, 99].

8.2.1 Statistical Effect

The possible statistical bias in the evaluation of the scaled factorial moment has been examined with a set of the Monte Carlo samples, each with the same statistical size as the data. The results from these samples, as shown in Fig. 8.3a, are very consistent, indicating that the present statistics is adequate to make the bias negligible. The same conclusion has been drawn from the study of the two MC samples, one with 5 times smaller size than data, one with twice larger (see Fig. 8.3b). The standard deviation in the samples (shown in Fig. 8.3a) was taken as the statistical error. The scaled factorial moments and their corresponding statistical errors are presented in Fig. 8.4 and tabulated in Table 8.1

8.2.2 Systematic Effects

The sensitivity to the choice of event axis has been tested by comparing the results calculated with respect to sphericity and thrust axis from the Monte Carlo sample. The definition of sphericity and thrust axis will be described later. As shown in Fig. 8.5, no discrepancy is observed. In our analysis, we choose the sphericity axis as the event axis.

The effects on the factorial moments of wide variations in the criteria for track and event selection were studied and found to be small. Figure 8.6 and Fig. 8.7 show two major effects: one from the variation of detector acceptance, one from p_t cuts. The standard cut for p_t is greater than 0.15 GeV, while for detector acceptance $|\cos(\theta)| < 0.8$.

The effects from the tracking inefficiency have been checked with a set of data samples, in each of which some percentage of tracks were randomly thrown in the full rapidity phase space. The results are shown in Fig. 8.8. No apparent discrepancy has been noticed.

The Monte Carlo used in this analysis is a QCD-based PS JETSET event generator plus a detailed simulation of the detector. We have compared the moments

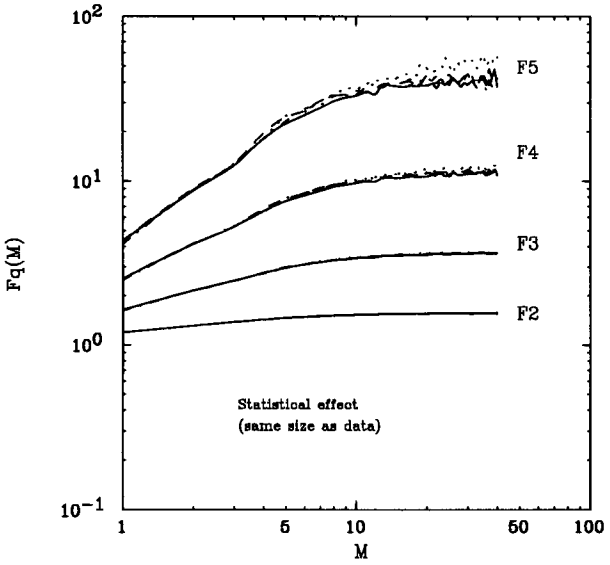

a. with the same statistical size as the data.

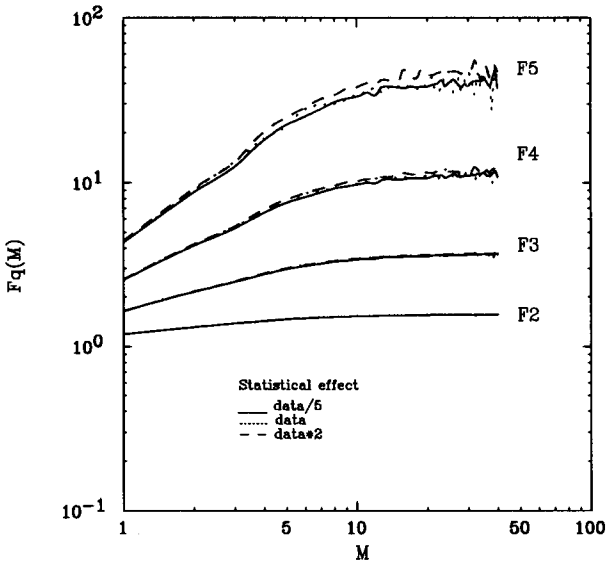

b. with the different statistical size.

Figure 8.3: Statistical effect. The results from a set of Monte Carlo sample.

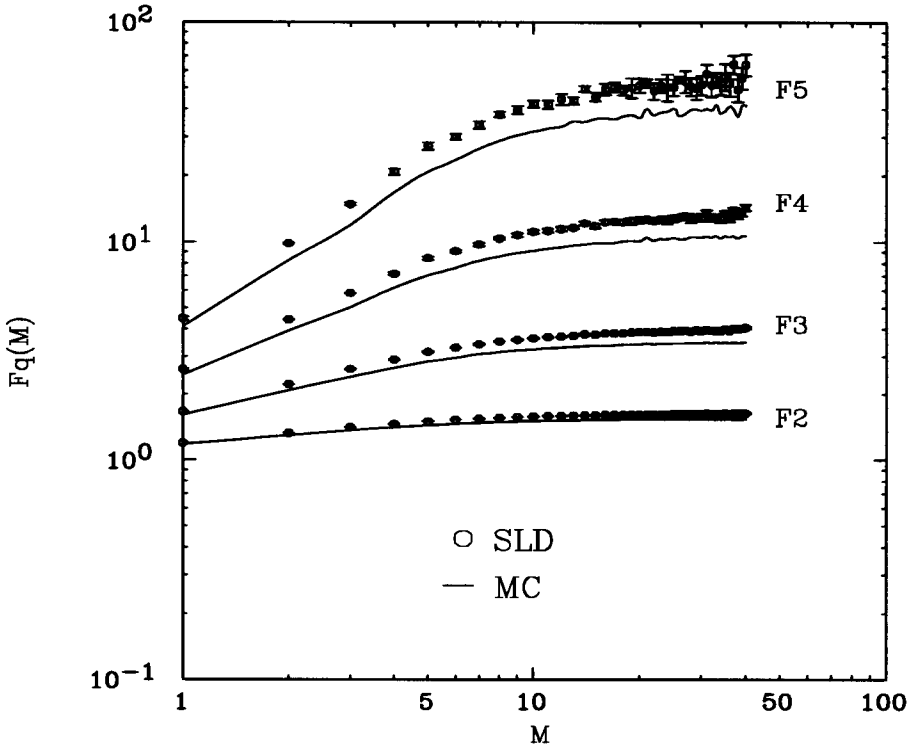

Figure 8.4: As in Fig.8.2, but with the statistical errors.

calculated at the generator level and the detector level, respectively. The result shows little discrepancy, indicating that the contribution to the moments from the detector simulation is small (see Fig. 8.9)

In the following two sections, we present our study by probing samples with different event shapes and various jet topologies.

8.2.3 Jet Topology Dependence

Jet Finding Algorithm

Jets are defined operationally by iterative clustering algorithms. One of algorithms which we used here is called Durham [105]. For each hadronic event, the scaled 'invariant mass' y_{ij} of every pair of particles is calculated, assuming particles to be

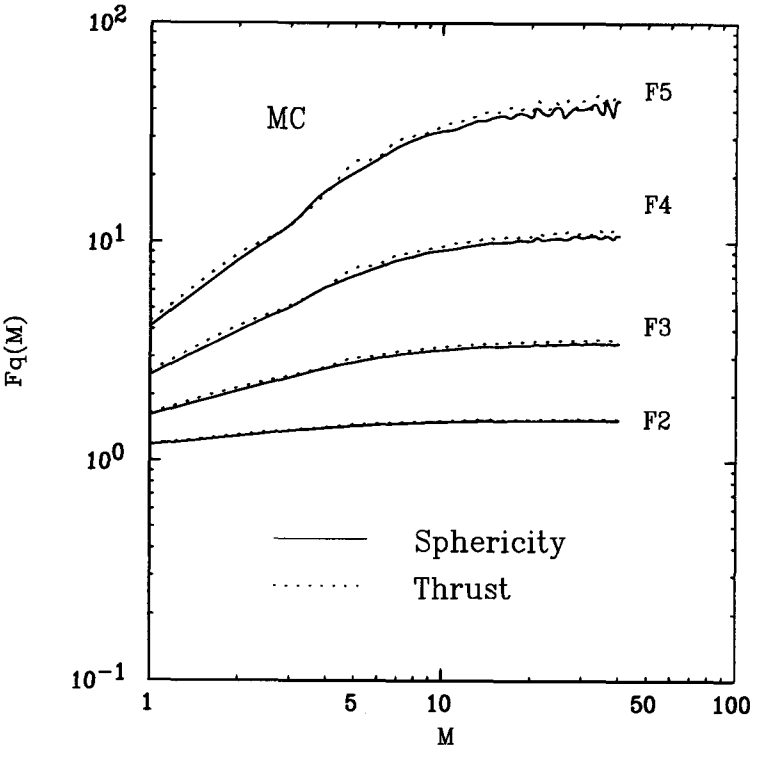

Figure 8.5: The factorial moments calculated with respect to sphericity and thrust axis from the Monte Carlo.

pions:

$$y_{ij} = \frac{2\min(E_i^2, E_j^2)(1 - cos\theta_{ij})}{E_{vis}^2}, \tag{8.4}$$

where E_i and E_j are the particle energies and θ_{ij} the opening angle between them. E_{vis} is the total visible energy in the event. The pair with the smallest y_{ij} is combined into a cluster (or pseudo-particle). This process is iterated until all pairs have $y_{ij} > y_{cut}$, where y_{cut} is the cutoff value. At this point, each cluster that remains is called a 'jet'. The number of found jets is clearly a function of y_{cut}. The jet rates as a function of y_{cut} is shown in Fig. 8.10.

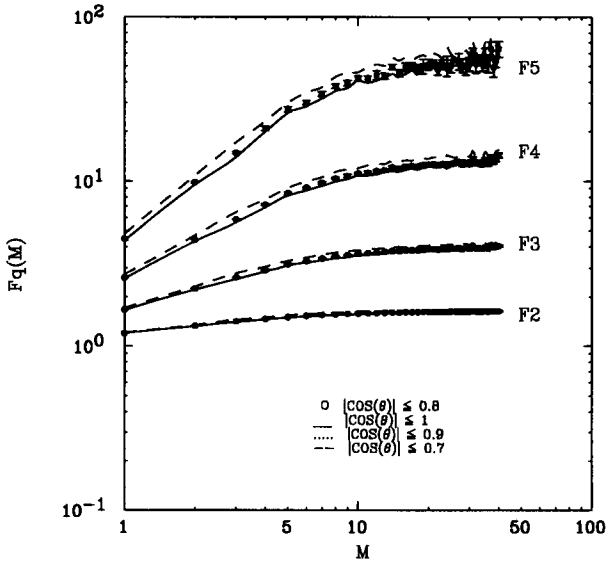

Figure 8.6: Effect from detector acceptance. The points correspond to the standard cut, $|\cos(\theta)| < 0.8$.

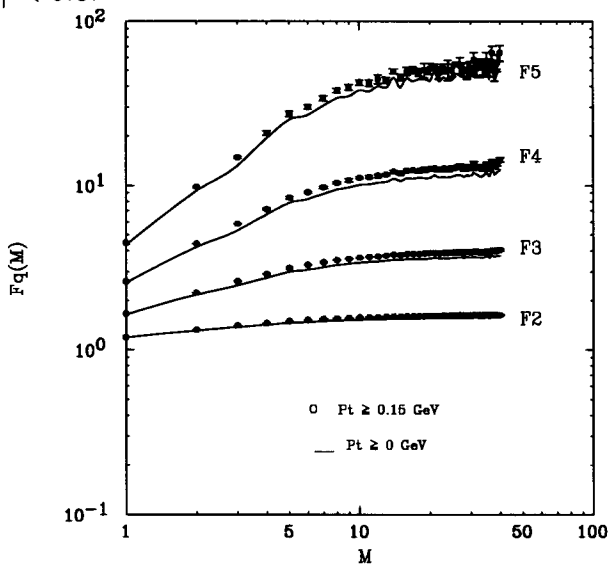

Figure 8.7: Effect from p_t cut.The points correspond to the standard cut, $p_t > 0.15$ GeV.

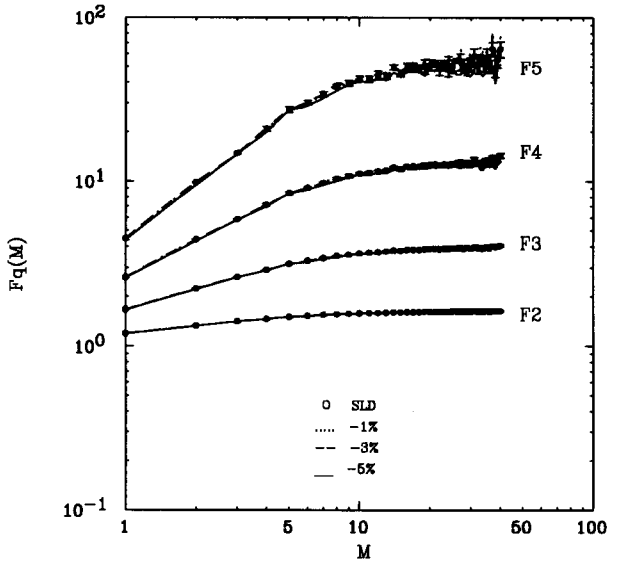

Figure 8.8: The effect from the tracking inefficiency. The inefficiency was estimated on average to be about -3%.

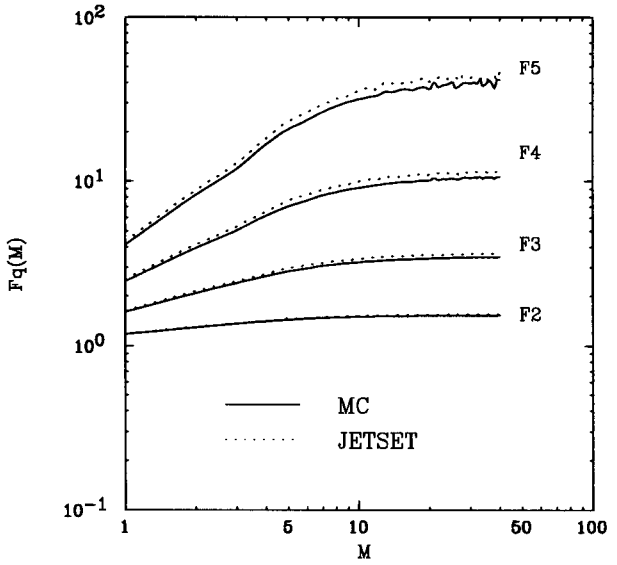

Figure 8.9: Comparison between the generator level and the detector level.

Results

The selected hadronic events are classified by using the Durham algorithm for a given y_{cut} into two groups: a sample of 2 jet events and a sample of 3 or more jet

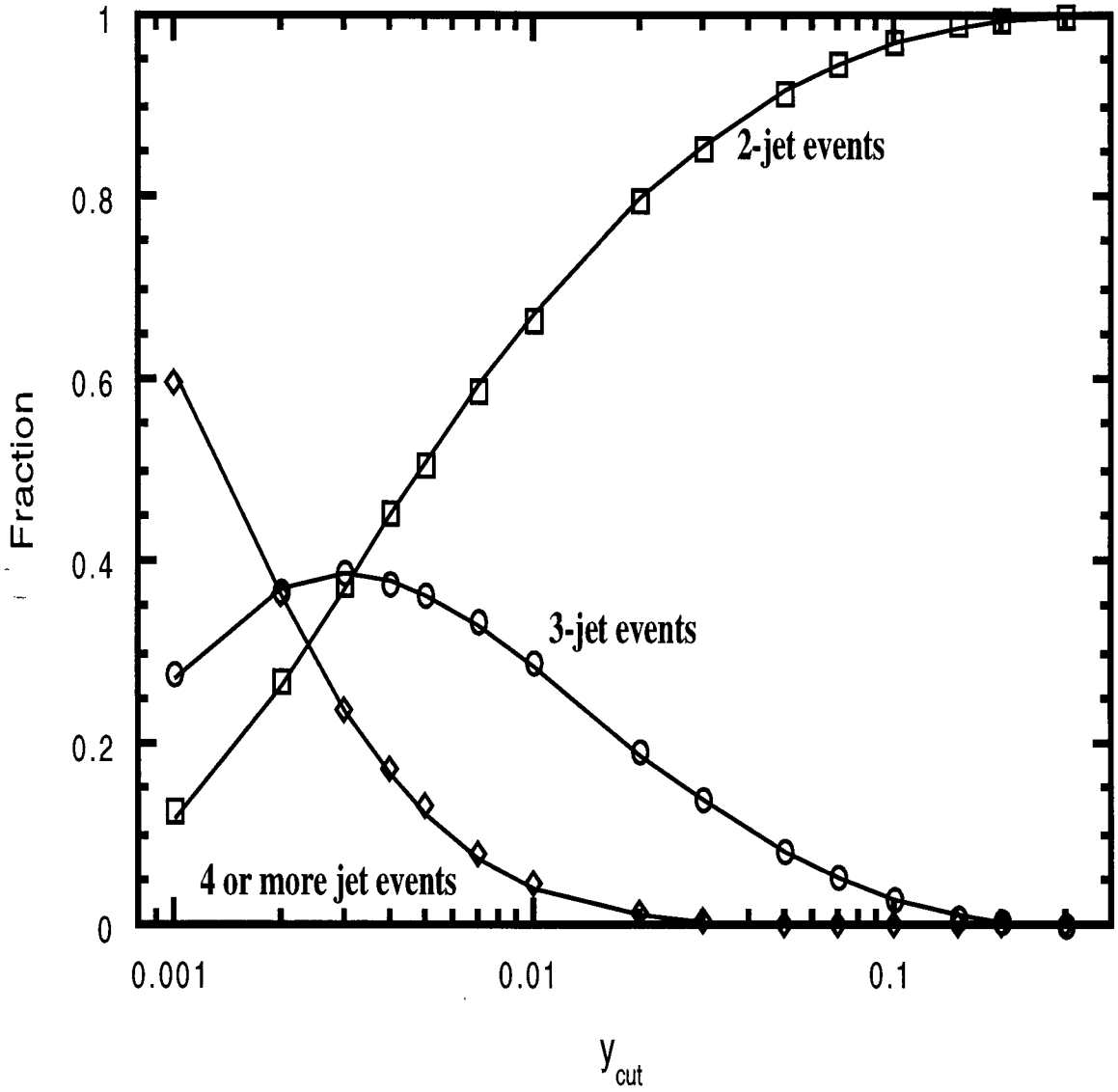

Figure 8.10: The jet rates as a function of y_{cut} obtained with the Durham jet finder. The symbols represent data, solid curves represent the Monte Carlo.

events. The latter implicates that the events have one or more hard-gluon radiations. Figure 8.11 shows the distributions of $F_q(M)$ from both samples at $y_{cut} = 0.003$, where the fraction of 2 jet events is about 0.4. We found that $F_q(M)$ grows faster as a function of M and saturates later in the 3 or more jet sample than in the 2 jet

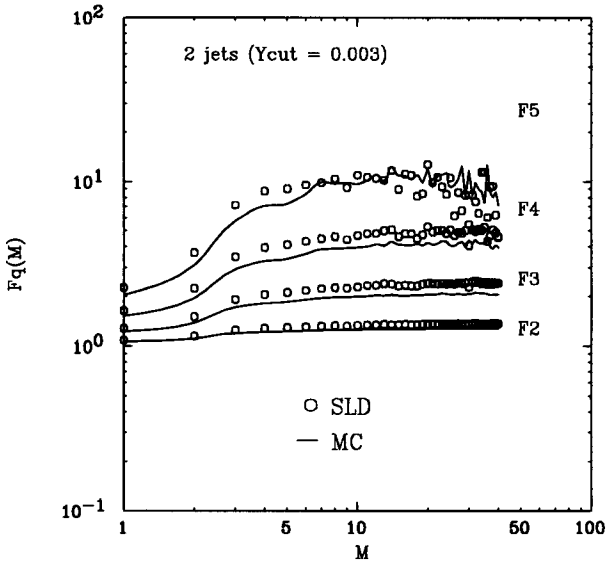

a. 2 jet event sample.

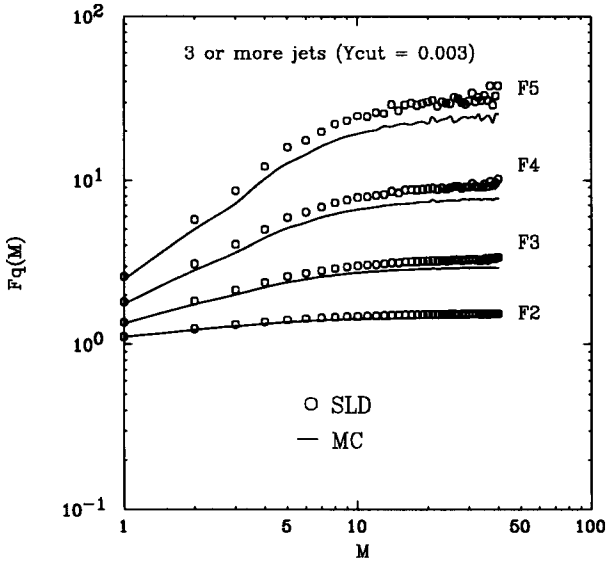

b. 3 or more jet event sample.

Figure 8.11: Jet topology dependence.

sample. The same features can be seen in the the Monte Carlo.

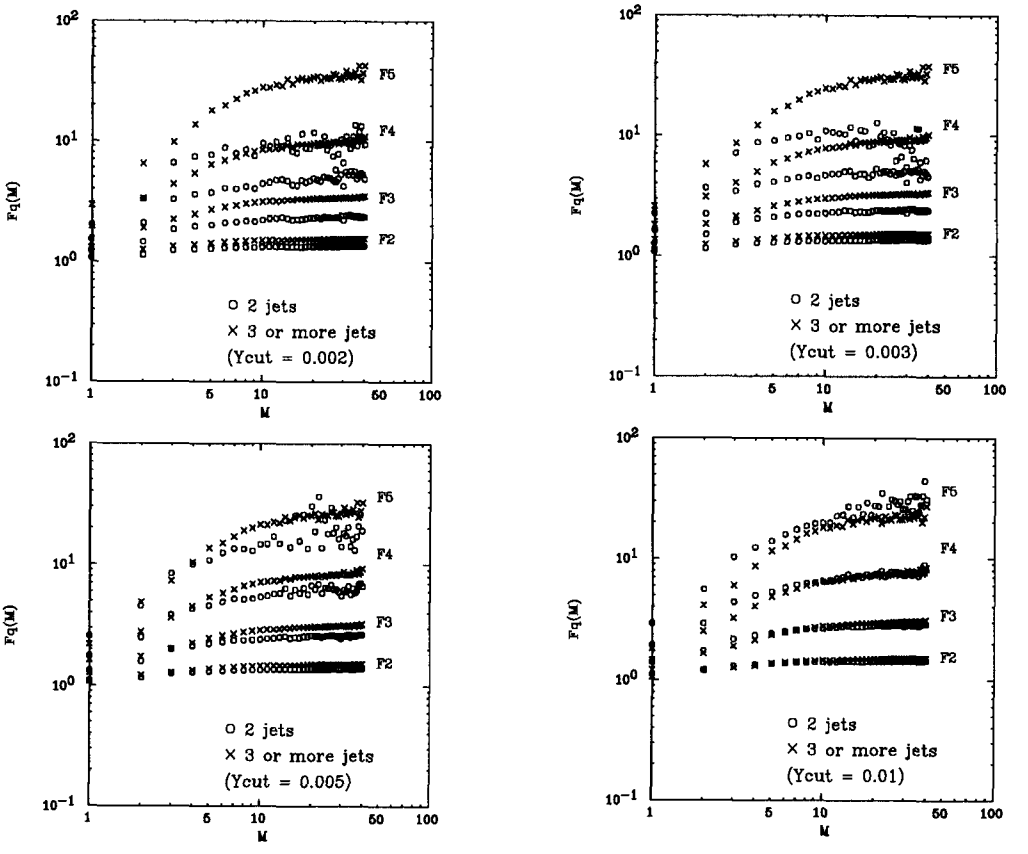

Figure 8.12: Comparison of 2 jet event sample with 3 or more jet event sample at $y_{cut} = 0.002, 0.003, 0.005, 0.01$.

The comparison between two samples at a variety of y_{cut} are shown in Fig. 8.12. As y_{cut} increases, $F_q(M)$ in the 2 jet sample are found to become larger. This is understandable since the sample has more hard-gluon jets contamination at higher y_{cut}. It appears that the hard-gluon radiations contribute much to the rise of the $F_q(M)$. This is compatible with the results from a p_t dependence study [98, 96].

To exclude the effects from the hard-gluon radiations and focus on the contribution from PS cascading, we selected the 2 jet only event sample only and studied the energy evolution of $F_q(M)$. Two samples were generated with JETSET at energy $\sqrt{s} = 91$ GeV and $\sqrt{s} = 150$ GeV, and both were constrained to have 2 jet events only. We found that $F_q(M)$ rise much faster at higher energy, where the parton shower is better developed. The result is shown in Fig. 8.13. We therefore conclude

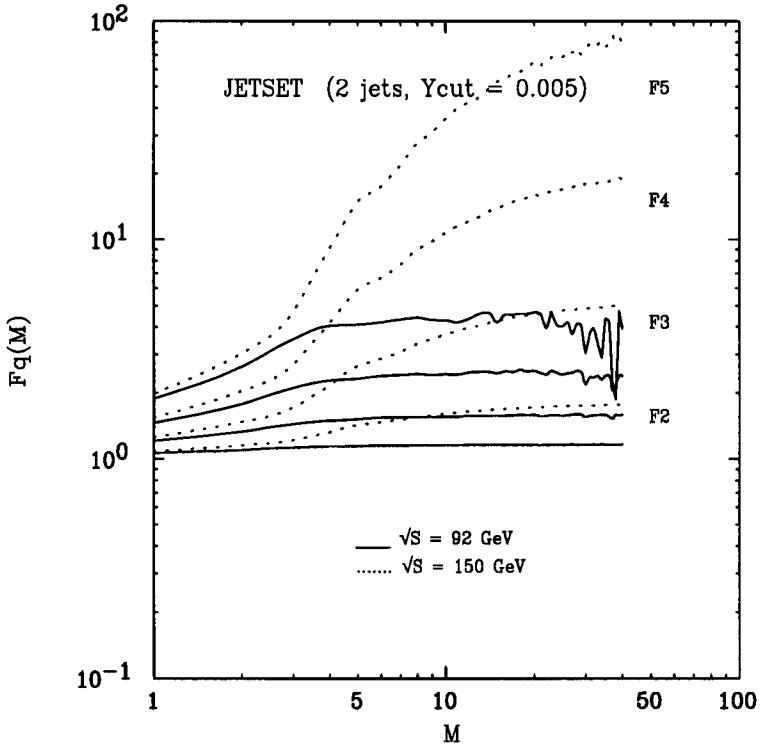

Figure 8.13: Energy dependence of $F_q(M)$ for 2 jets event.

that both cascading and hard-gluon radiation contribute to the increasing of $F_q(M)$ as a function of M.

8.2.4 Event Shape Dependence

Definition of event shape

Hadronic event shape variables are tools to study both the amount of gluon radiation and details of the jet structure [106]. Since the laboratory frame and the center of mass system of the annihilation are usually identical, events from $q\bar{q}$ final states without hard gluon radiation results in two collimated, back-to-back jets of hadrons. The emission of one hard gluon leads to planar 3-jet events, while the emission of two or more energetic gluons can cause non-planar multi-jet event structures.

A typical event shape observable is sphericity, S, which is defined using three

eigenvalues of the momentum tensor [106]:

$$s^{ij} = \frac{\sum_a p_a^i p_a^j}{\sum_a p_a^2}, \qquad i,j = 1,2,3, \tag{8.5}$$

where p_a^i is the i^{th} component of the momentum vector $\vec{p_a}$, and the sum is made over the particles. Let Q_1, Q_2, and Q_3 be the eigenvalues of the s^{ij}, satisfying the conditions $Q_1 \leq Q_2 \leq Q_3$ and $\sum_i Q_i = 1$. The sphericity and aplanarity are then given by

$$S = \frac{3}{2}(Q_1 + Q_2); \qquad A = \frac{3}{2}Q_1. \tag{8.6}$$

An ideal two jet event has $S = 0$ and $A = 0$, while spherical events are characterized by $S = 1$. Deviations from a planar shape are indicated by $A > 0$. Figure 8.14 shows the distributions of sphericity and aplanarity.

Results

We first selected the highly planar events ($0 \leq A < 0.01$), and then grouped them into two samples: one with collimated shape ($0 \leq S < 0.05$), which corresponds to the 2 jet event; and one with spherical shape ($0.05 \leq S \leq 1$), which corresponds to the 3 jet event. We found that $F_q(M)$ in the later sample grows faster as function of M, confirming the importance to the increasing of $F_q(M)$ from the hard-gluon radiation. The result is shown in Fig. 8.15. This study compliments the previous analysis.

8.3 Conclusion

We have investigated the intermittent behavior of particle fluctuations in rapidity phase space in hadronic Z^0 decays from e^+e^- annihilations with the method of scaled factorial moment. We observed that the logarithms of the moments grow as a function of the logarithms of the number M, and then flatten off at $M > 10$ ($\delta y \sim 0.4$). Both statistical and systematic effects were examined, and found to be small. Our results are compatible with the LEP experiments. The dependencies on event shape and jet topology have been studied, and we found that both parton cascade and hard-gluon radiations contribute to the growth of the moments. The observed features appear to be reproduced reasonably well by the QCD-based parton shower Monte Carlo model.

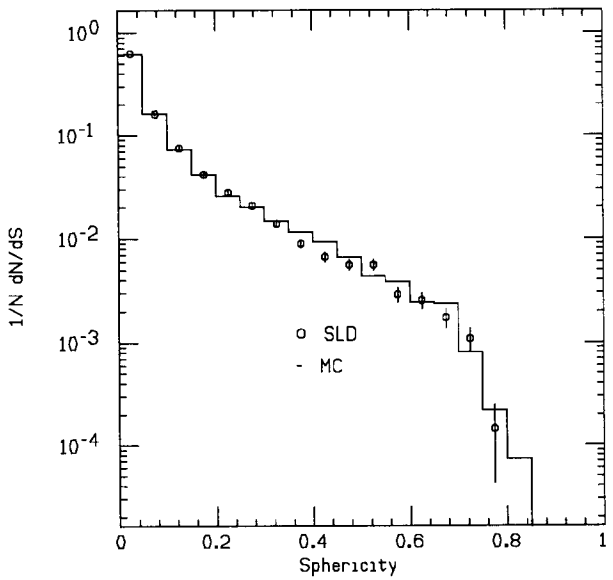

a. sphericity.

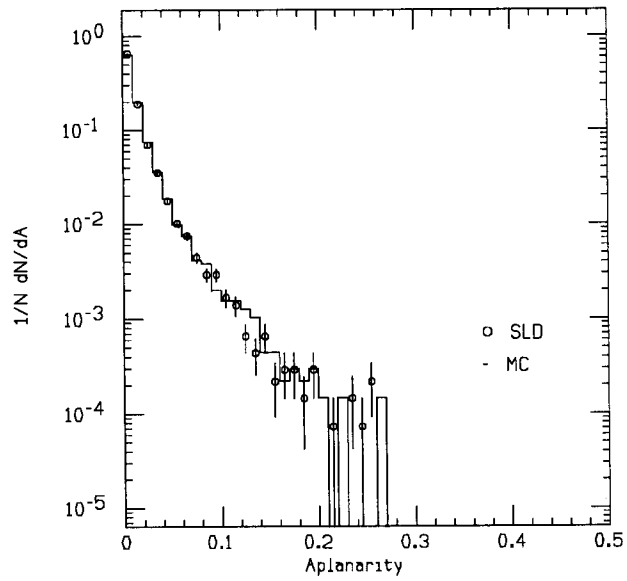

b. aplanarity.

Figure 8.14: Distributions of the event shape variables in comparison with the Monte Carlo.

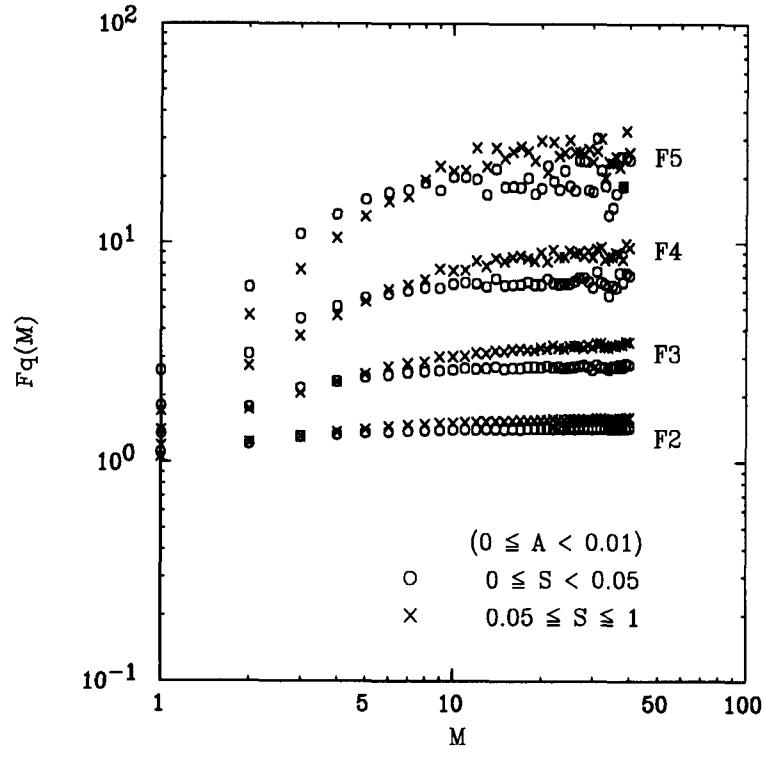

Figure 8.15: Comparison of two planar event samples: one with collimated shape ($0 \leq S < 0.05$), which corresponds to the 2 jets event; and one with spherical shape ($0.05 \leq S \leq 1$), which corresponds to the 3 jets event.

Table 8.1: The scaled factorial moments

M	F_2	F_3	F_4	F_5
1	1.20± 0.00	1.66± 0.01	2.61± 0.03	4.47± 0.08
2	1.33± 0.00	2.23± 0.00	4.41± 0.01	9.84± 0.09
3	1.41± 0.00	2.61± 0.01	5.83± 0.03	14.83± 0.18
4	1.46± 0.00	2.90± 0.01	7.16± 0.10	20.82± 0.65
5	1.50± 0.00	3.14± 0.02	8.43± 0.15	27.23± 1.10
6	1.53± 0.00	3.29± 0.01	9.09± 0.11	29.97± 0.86
7	1.55± 0.00	3.40± 0.02	9.75± 0.18	33.88± 1.26
8	1.56± 0.00	3.51± 0.01	10.37± 0.12	37.82± 1.11
9	1.57± 0.00	3.58± 0.02	10.75± 0.22	39.61± 1.75
10	1.58± 0.00	3.63± 0.02	11.13± 0.17	42.32± 1.57
11	1.59± 0.00	3.68± 0.02	11.25± 0.19	42.03± 1.88
12	1.59± 0.00	3.70± 0.02	11.46± 0.26	44.45± 2.61
13	1.60± 0.00	3.74± 0.01	11.62± 0.15	43.82± 1.59
14	1.60± 0.00	3.80± 0.03	12.16± 0.24	49.68± 1.68
15	1.60± 0.00	3.78± 0.03	11.83± 0.27	45.51± 2.08
16	1.61± 0.00	3.83± 0.02	12.33± 0.25	49.53± 2.97
17	1.61± 0.00	3.84± 0.02	12.39± 0.20	50.59± 2.57
18	1.61± 0.00	3.84± 0.04	12.32± 0.31	49.00± 2.62
19	1.61± 0.00	3.86± 0.04	12.45± 0.46	50.28± 5.32
20	1.62± 0.00	3.88± 0.04	12.57± 0.40	51.50± 3.84
21	1.62± 0.00	3.89± 0.02	12.68± 0.22	52.56± 2.40
22	1.62± 0.00	3.88± 0.03	12.45± 0.34	48.57± 4.27
23	1.62± 0.00	3.90± 0.03	12.68± 0.27	51.47± 3.62
24	1.62± 0.00	3.88± 0.04	12.53± 0.48	50.59± 7.13
25	1.62± 0.00	3.92± 0.03	12.77± 0.41	50.47± 4.38
26	1.62± 0.00	3.93± 0.02	12.95± 0.15	54.80± 1.85
27	1.62± 0.00	3.94± 0.03	13.02± 0.47	53.86± 6.15
28	1.62± 0.00	3.91± 0.04	12.64± 0.41	50.93± 4.86
29	1.62± 0.00	3.95± 0.04	12.91± 0.44	49.84± 5.56
30	1.62± 0.00	3.93± 0.04	12.83± 0.44	51.90± 5.24
31	1.63± 0.00	3.98± 0.03	13.54± 0.43	58.29± 5.95
32	1.63± 0.00	3.94± 0.04	12.93± 0.47	51.67± 6.03
33	1.63± 0.00	3.93± 0.04	12.86± 0.42	54.81± 4.34
34	1.62± 0.00	3.92± 0.05	12.84± 0.58	52.67± 5.96
35	1.63± 0.00	4.00± 0.01	13.45± 0.41	56.54± 7.85
36	1.62± 0.00	3.93± 0.03	12.90± 0.54	52.50± 6.68
37	1.63± 0.00	4.03± 0.03	13.93± 0.37	64.22± 6.07
38	1.63± 0.00	4.00± 0.03	13.15± 0.45	49.22± 5.88
39	1.63± 0.00	4.03± 0.03	13.63± 0.48	55.79± 6.48
40	1.63± 0.01	4.06± 0.05	14.32± 0.47	64.19± 7.29

Chapter 9

Summary

Quantum Chromodynamics (QCD), commonly accepted as the fundamental theory of the strong force, has successfully predicted and described many aspects of strong interaction phenomena. However, the experimental tests of QCD are much less precise than tests of Quantum Electrodynamics (QED), the accepted theory of electromagnetic interactions, mainly because perturbative calculations are difficult due to the large number of diagrams involved, and the mechanism of hadronization remains unsolved. It is therefore important to push the accuracy of QCD tests as far as possible, and to expand the tests to many aspects and processes.

The production of hadrons in e^+e^- annihilation, particularly at the Z^0 resonance, has proved to be ideal for clean tests of QCD due to the completely known initial state, large cross section and negligible background. The hadrons produced in such process form jets (tight bundles of hadrons), which preserve the energy and direction of the primary partons. Thus, the study of the final state particles can lead to insights of the dynamics of parton production, which is described by QCD. The SLAC Linear Collider (SLC) produces e^+e^- annihilation events at the Z^0 resonance which are recorded by the SLC Large Detector (SLD). A large number of analyses have been performed in the SLD experiment, based on the hadronic events collected in the years 1992-1995 . In this dissertation, we presented experimental studies on the following three aspects of the final state particles: charged particle multiplicity distribution, ratio H_q of cumulant to factorial moments, and charged particle fluctuations in the

rapidity phase space:

- Charged particle multiplicity distribution

  One particularly simple and fundamental observable which contains information about the dynamics of the hadronic production is the charged-particle multiplicity distribution, it has been studied extensively both experimentally and theoretically. The Poisson distribution (PD) has been found to deviate considerably from data, implying that the particles are not produced randomly and independently. Perturbative QCD can be applied to calculate the multiplicity distribution only at parton level due to the uncertain hadronization mechanism. We therefore first measured the charged-particle multiplicity distribution. The distribution was corrected for effects introduced by the detector, such as geometrical acceptance, tracking inefficiency, and additional tracks from photon conversions and particle interactions in the detector materials, as well as for initial-state photon radiation and the effect of the hadronic event selection. The shape of the measured multiplicity distribution was fit to two phenomenological parameterizations, the negative binomial distribution (NBD)and the log-normal distribution (LND). We found that the data is well-described by the log-normal distribution. The log-normal distribution is predicted by a recent model in which the particles result from a scale-invariant stochastic branching process. This appears to give a natural connection to state-of-the art models for multiparticle production involving QCD parton cascade and hadronization. The average multiplicity and the second binomial moment were found to be $< n >= 20.63 \pm 0.01 \pm 0.34$ and $R_2 = 1.0429 \pm 0.0003 \pm 0.0034$, which are in good agreement with the data measured at the same energy $\sqrt{s} = 91$ GeV at the LEP experiments. We have studied the energy dependence of the average multiplicity, and noticed that both leading-log and next-to-leading order perturbative QCD can describe the data. However, we found that next-to-leading order perturbative QCD clearly provides a better description of the data when a higher rank moment, the second binomial moment R_2 is studied. Apparently, a more sensitive quantity is needed in order to test the predictions of QCD in varieties of approximation.

- Ratio of cumulant to factorial moments

  The ratio H_q of cumulant to factorial moments of the charged-particle multiplicity distribution was proposed recently and is believed to offer a more sensitive test of QCD. We performed the first experimental analysis of this quantity. We found that H_q, as a function of the moment rank q, decreases sharply to a negative minimum at $q \sim 5$, followed by a sequence of quasi-oscillations. Various systematic uncertainties including global tracking efficiency, the tracking efficiency dependence on multiplicity and background were examined extensively. The observed qualitative features are found to be in good agreement within statistical and systematic errors with the predictions from higher-order perturbative QCD calculations, thus excluding the leading double-logarithm approximation which predicts H_q monotonically decreasing to zero as $H_q \sim q^{-2}$. Both phenomenological PD and NBD distributions were found to be clearly inconsistent with the data, while the log-normal distribution predicts features similar to those of the data. This perhaps indicates that an iterative scale-invariant production is a more realistic mechanism.

- Intermittency

  We also performed an analysis of the intermittent behavior of charged particle fluctuations in rapidity phase space using the method of scaled factorial moments. A power law dependence of the scaled factorial moments on the resolution (or the number M of the subdivisions) of rapidity phase space is expected theoretically if the particles are produced in a scale-invariant cascade mechanism. We observed that the logarithms of the moments grow as a function of the logarithm of the number M of the subdivisions of the rapidity in the interval $-2 < y < 2$, and then flatten off at $M > 10$ ($\delta y \sim 0.4$). Such a flattening at small resolutions was interpreted as a running of the QCD coupling constant α_s with Q^2, as expected in the theory. Both statistical and systematic effects were examined, and found to be small. Our results are compatible with the LEP experiments. We studied the dependencies of the intermittent behavior on event-shape and jet-topology, and found that both parton cascade and

hard-gluon radiation contribute to the growth of the moments.

The overall features of the data appear to be reproduced reasonably well by the QCD-based parton shower Monte Carlo model and qualitatively well described by higher order perturbative QCD calculations. The phenomenological LND distribution fits the data closely, perhaps indicating that an iterative scale-invariant branching is a more realistic mechanism of particle production. SLC performance continued to improve during the run, routinely achieving Z^0 production rates of about 40 per hour. With an increase of statistics, we should be able to study sensitive quantities such as the ratio of cumulant to factorial moment on identified quark and gluon jets, making new tests of QCD. A more quantitative comparison will be expected if the hadronization is taken into account in the future.

QCD is capable of making quantitative predictions of parton-level processes which can be calculated using perturbative theory. Much experimental effort has been directed at such tests. However, this such quantitative tests represent only a small fraction of the observable strong-interaction phenomena. It is widely assumed that QCD is ultimately responsible for all such phenomena, although it may be manifested in complex and subtle ways.

In this dissertation, we have attempted to extend the range of phenomena which can be compared with QCD. We have shown that these observables are certainly not inconsistent with QCD and have attempted to test distinctive qualitative predictions of QCD. Such is the case for the analysis of the H_q moments in particular.

Indeed, we find that QCD calculable processes at the parton level give rise to subtle effects in our particle production analyses which are observed in the data. These new results help to bolster our confidence in the notion that QCD is in fact ultimately responsible for the rest range of strong-interaction phenomena.

Appendix A

The SLD Collaboration

K. Abe,[29] I. Abt,[14] C.J. Ahn,[26] T. Akagi,[27] N.J. Allen,[4] W.W. Ash,[27]†
D. Aston,[27] K.G. Baird,[25] C. Baltay,[33] H.R. Band,[32] M.B. Barakat,[33]
G. Baranko,[10] O. Bardon,[16] T. Barklow,[27] A.O. Bazarko,[11] R. Ben-David,[33]
A.C. Benvenuti,[2] T. Bienz,[27] G.M. Bilei,[22] D. Bisello,[21] G. Blaylock,[7]
J.R. Bogart,[27] T. Bolton,[11] G.R. Bower,[27] J.E. Brau,[20] M. Breidenbach,[27]
W.M. Bugg,[28] D. Burke,[27] T.H. Burnett,[31] P.N. Burrows,[16] W. Busza,[16]
A. Calcaterra,[13] D.O. Caldwell,[6] D. Calloway,[27] B. Camanzi,[12]
M. Carpinelli,[23] R. Cassell,[27] R. Castaldi,[23][a] A. Castro,[21] M. Cavalli-Sforza,[7]
E. Church,[31] H.O. Cohn,[28] J.A. Coller,[3] V. Cook,[31] R. Cotton,[4]
R.F. Cowan,[16] D.G. Coyne,[7] A. D'Oliveira,[8] C.J.S. Damerell,[24] M. Daoudi,[27]
R. De Sangro,[13] P. De Simone,[13] R. Dell'Orso,[23] M. Dima,[9] P.Y.C. Du,[28]
R. Dubois,[27] B.I. Eisenstein,[14] R. Elia,[27] E. Etzion,[4] D. Falciai,[22]
M.J. Fero,[16] R. Frey,[20] K. Furuno,[20] T. Gillman,[24] G. Gladding,[14]
S. Gonzalez,[16] G.D. Hallewell,[27] E.L. Hart,[28] Y. Hasegawa,[29] S. Hedges,[4]
S.S. Hertzbach,[17] M.D. Hildreth,[27] J. Huber,[20] M.E. Huffer,[27] E.W. Hughes,[27]
H. Hwang,[20] Y. Iwasaki,[29] D.J. Jackson,[24] P. Jacques,[25] J. Jaros,[27]
A.S. Johnson,[3] J.R. Johnson,[32] R.A. Johnson,[8] T. Junk,[27] R. Kajikawa,[19]
M. Kalelkar,[25] H. J. Kang,[26] I. Karliner,[14] H. Kawahara,[27] H.W. Kendall,[16]
Y. Kim,[26] M.E. King,[27] R. King,[27] R.R. Kofler,[17] N.M. Krishna,[10]
R.S. Kroeger,[18] J.F. Labs,[27] M. Langston,[20] A. Lath,[16] J.A. Lauber,[10]

D.W.G. Leith,[27] M.X. Liu,[33] X. Liu,[7] M. Loreti,[21] A. Lu,[6] H.L. Lynch,[27] J. Ma,[31] G. Mancinelli,[22] S. Manly,[33] G. Mantovani,[22] T.W. Markiewicz,[27] T. Maruyama,[27] R. Massetti,[22] H. Masuda,[27] E. Mazzucato,[12] A.K. McKemey,[4] B.T. Meadows,[8] R. Messner,[27] P.M. Mockett,[31] K.C. Moffeit,[27] B. Mours,[27] G. Müller,[27] D. Muller,[27] T. Nagamine,[27] U. Nauenberg,[10] H. Neal,[27] M. Nussbaum,[8] Y. Ohnishi,[19] L.S. Osborne,[16] R.S. Panvini,[30] H. Park,[20] T.J. Pavel,[27] I. Peruzzi,[13][b] M. Piccolo,[13] L. Piemontese,[12] E. Pieroni,[23] K.T. Pitts,[20] R.J. Plano,[25] R. Prepost,[32] C.Y. Prescott,[27] G.D. Punkar,[27] J. Quigley,[16] B.N. Ratcliff,[27] T.W. Reeves,[30] J. Reidy,[18] P.E. Rensing,[27] L.S. Rochester,[27] J.E. Rothberg,[31] P.C. Rowson,[11] J.J. Russell,[27] O.H. Saxton,[27] S.F. Schaffner,[27] T. Schalk,[7] R.H. Schindler,[27] U. Schneekloth,[16] B.A. Schumm,[15] A. Seiden,[7] S. Sen,[33] V.V. Serbo,[32] M.H. Shaevitz,[11] J.T. Shank,[3] G. Shapiro,[15] S.L. Shapiro,[27] D.J. Sherden,[27] K.D. Shmakov,[28] C. Simopoulos,[27] N.B. Sinev,[20] S.R. Smith,[27] J.A. Snyder,[33] P. Stamer,[25] H. Steiner,[15] R. Steiner,[1] M.G. Strauss,[17] D. Su,[27] F. Suekane,[29] A. Sugiyama,[19] S. Suzuki,[19] M. Swartz,[27] A. Szumilo,[31] T. Takahashi,[27] F.E. Taylor,[16] E. Torrence,[16] J.D. Turk,[33] T. Usher,[27] J. Va'vra,[27] C. Vannini,[23] E. Vella,[27] J.P. Venuti,[30] R. Verdier,[16] P.G. Verdini,[23] S.R. Wagner,[27] A.P. Waite,[27] S.J. Watts,[4] A.W. Weidemann,[28] E.R. Weiss,[31] J.S. Whitaker,[3] S.L. White,[28] F.J. Wickens,[24] D.A. Williams,[7] D.C. Williams,[16] S.H. Williams,[27] S. Willocq,[33] R.J. Wilson,[9] W.J. Wisniewski,[5] M. Woods,[27] G.B. Word,[25] J. Wyss,[21] R.K. Yamamoto,[16] J.M. Yamartino,[16] X. Yang,[20] S.J. Yellin,[6] C.C. Young,[27] H. Yuta,[29] G. Zapalac,[32] R.W. Zdarko,[27] C. Zeitlin,[20] Z. Zhang,[16] and J. Zhou,[20]

[1] *Adelphi University, Garden City, New York 11530*

[2] *INFN Sezione di Bologna, I-40126 Bologna, Italy*

[3] *Boston University, Boston, Massachusetts 02215*

[4] *Brunel University, Uxbridge, Middlesex UB8 3PH, United Kingdom*

[5] *California Institute of Technology, Pasadena, California 91125*

[6] *University of California at Santa Barbara, Santa Barbara, California 93106*

[7] *University of California at Santa Cruz, Santa Cruz, California 95064*

[8] *University of Cincinnati, Cincinnati, Ohio 45221*

[9] *Colorado State University, Fort Collins, Colorado 80523*

[10] *University of Colorado, Boulder, Colorado 80309*

[11] *Columbia University, New York, New York 10027*

[12] *INFN Sezione di Ferrara and Università di Ferrara, I-44100 Ferrara, Italy*

[13] *INFN Lab. Nazionali di Frascati, I-00044 Frascati, Italy*

[14] *University of Illinois, Urbana, Illinois 61801*

[15] *Lawrence Berkeley Laboratory, University of California, Berkeley, California 94720*

[16] *Massachusetts Institute of Technology, Cambridge, Massachusetts 02139*

[17] *University of Massachusetts, Amherst, Massachusetts 01003*

[18] *University of Mississippi, University, Mississippi 38677*

[19] *Nagoya University, Chikusa-ku, Nagoya 464 Japan*

[20] *University of Oregon, Eugene, Oregon 97403*

[21] *INFN Sezione di Padova and Università di Padova, I-35100 Padova, Italy*

[22] *INFN Sezione di Perugia and Università di Perugia, I-06100 Perugia, Italy*

[23] *INFN Sezione di Pisa and Università di Pisa, I-56100 Pisa, Italy*

[25] *Rutgers University, Piscataway, New Jersey 08855*

[24] *Rutherford Appleton Laboratory, Chilton, Didcot, Oxon OX11 0QX United Kingdom*

[26] *Sogang University, Seoul, Korea*

[27] *Stanford Linear Accelerator Center, Stanford University, Stanford, California 94309*

[28] *University of Tennessee, Knoxville, Tennessee 37996*

[29] *Tohoku University, Sendai 980 Japan*

[30] *Vanderbilt University, Nashville, Tennessee 37235*

[31] *University of Washington, Seattle, Washington 98195*

[32] *University of Wisconsin, Madison, Wisconsin 53706*

[33] *Yale University, New Haven, Connecticut 06511*

† *Deceased*

[a] *Also at the Università di Genova*

[b] *Also at the Università di Perugia*

Bibliography

[1] CDF collaboration, Phys. Rev. Lett. 73, 225 (1994); D0 collaboration Phys. Rev. Lett. 72, 2138 (1994), Phys. Rev. Lett. 74, 2632 (1995).

[2] Particle Data Group, Phys. Rev. D54, 24 (1996).

[3] M. Gell-Mann, Acta Physica Austriaca Suppl. IX (1972) 733; H. Fritzsch, M. Gell-Mann and H. Leytwyler, Phys. Lett. B47 (1973) 365.

[4] D.J. Gross and F. Wilczek, Phys. Rev. Lett. 30 (1973) 1343; Phys. Rev. D8 (1973) 3633; H.D. Politzer, Phys. Rev. Lett 30 (1973) 1346.

[5] G. Altarelli, Annu. Rev. Nucl. Part. Sci. 39 (1989) 357.

[6] G. Hooft, Nucl. Phys. B61 (1973) 455.

[7] W. Caswell, Phys. Rev. Lett. 31 (1974) 244; D.R.T. Jones, Nucl. Phys. B75 (1974) 531.

[8] O.V. Tarasov, A.A. Vladimirov and A.Y. Zharkov, Phys. Lett. B93 (1980) 429.

[9] M. Aguilar-Benitez et al., Phys. Lett. B239 (1990) 1.

[10] M. Consoli and W. Hollik in: Z Physics at LEP 1, CERN Report 89-08, Vol. I. p.7; F.A.Berends in: Z Physics at LEP 1, CERN Report CERN-89-08, Vol. I, p.89.

[11] F. Abe et al., Phys. Rev. Lett. 68 (1992) 447.

[12] J. Ellis, M. K. Gaillard and G. G. Ross, Nucl. Phys. B111 (1976) 253.

[13] A. Ali, et al, Nucl. Phys. B167 (1980); R.K. Ellis, D.A. Ross and E.A. terrano, Nucl. Phys. B178 (1981)421. K. Fabricius et al, Z. Phys C11 (1982) 315.

[14] B.R.Webber, Annu. Rev. Nucl. Part. Sci. 36 (1986) 253.

[15] K.Konishi, A.Ukawa and G.Veneziano, Nucl. Phys. B157 (1979) 45; R.Odorico, Nucl. Phys. B172 (1980) 157; B.R. Webber, Nucl. Phys. B238 (1984) 492.

[16] G. Altarelli and G. Parisi, Nucl. Phys. B126 (1977) 298.

[17] A.H. Muller, Phys. Lett B104 (1981) 161; A. Bassetto et al., Nucl. Phys. B207 (1982) 189; Y.L. Dokshitzer, V.S.Fadin and V.A.Khoze, Phys. Lett. B 115 (1982) 242; V.A.Koze, Y.L.Dokshitzer and S.I. Troyan, Color Coherence in QCD jets, Lund preprint LU TP 90-12;

[18] R.D. Field and R.P. Feynman, Nucl. Phys. B 136 (1978) 1.

[19] T. Sjostrand, Int. J. Mod. Phys. A (1988) 751.

[20] B. Andersson et al., Phys Rep. 97 (1983) 31; X. Artru, Phys. Rep. 97 (1983) 147.

[21] J. Schwinger, Physics. Rev. 82 (1951) 664; B. Andersson et al., Z. Phys C6 (1980) 235.

[22] B. Andersson et al., Nucl. Phys. B197 (1982) 45.

[23] T. Sjostrand, Comput. Phys. Commun. 39 (1986) 347.

[24] G.C. Fox and S. Wolfram, Nucl. Phys. B213 (1983) 65.

[25] G. Marchesini and B.R. Webber, Nucl. Phys. B310 (1988) 461.

[26] M. Aguilar-Benitez et al., Phys. Lett. B239 (1990) 1.

[27] J.Kent et al., SLAC-PUB-4922, (1989).

[28] SLD Collaboration. The SLD design report. SLAC report 273, SLAC, 1984.

[29] G.D. Agnew et al., Design and Performance of the SLD Vertex Detector, SLAC-PUB-5906, 1992; G.D. Agnew et al., XXVI International Conference on High Enegy Physics. In T. Ferbel, editor, Dallas HEP, pages 1862-1866, Dallas, 1992.

[30] J.P.Venuti and G.B.Chadwick, IEEE Trans. On Nucl.Sci 36 (1989) 595.

[31] G.M.Haller et al., IEEE Trans. On Nucl. Sci. 38 (1991) 357.

[32] T. Junk, Ph.D. Thesis, SLAC-Report, 1995.

[33] S.C.Berridge, J.E. Brau et al., First Results from the SLD Silicon Calorimeter. IEEE Trans. on Nucl. Sci., 39(5):1242,1992.

[34] D. Axen et al., Nucl.. Inst. Meth. A238 (1993) 472; S. Gonzalez Martirena, Ph.D. thesis, SLAC-Report-439, 1994.

[35] K.T. Pitts, Ph.D. Thesis, SLAC-Report-446, 1994.

[36] K. Abe, et al., Nucl. Inst. Meth. A343 (1994) 74.

[37] A.C. Benvenuti et al., Nucl. Instr. Meth. A276 (1989) 94.

[38] T. Sjostrand and M. Bengtsson, Comp. Phys. Comm. 43, 367 (1987)

[39] R.Brun et al., GEANT3 User's Guide, CERN DD/EE/84-1 (1989).

[40] J.N. Yamartino, Ph.D. Thesis, SLAC-Report-426.

[41] D. Muller, *QCD Studies of Hadronic Decays of Z^0 Bosons by SLD*, presented at the QCD Moriond 93.

[42] P.N. Burrows, H. Park, K.T. Pitts, J.M. Yamartino, SLD Note 229, 1993.

[43] Jan A. Lauber, Ph.D Thesis, SLAC-Report-413 (1993).

[44] SLD Collaboration, Phys. Rev. D52 (1995) 4828.

[45] Multiparticle Dynamics, edited by A. Giovannini, W. kittel, Singapore: World Scientific 1990; G. Giacomelli: Int. J. Mod. Phys. A5 (1990) 223; Hadronic Multiparticle Production, edited y P. Carruthers, Singapore: World Scientific 1990.

[46] A. Giovannini and L. Van Hove, Z. Phys. C3 (1986) 391.

[47] T.I. Azimov, Y.L. Dokshitzer, V.A. Khoze and S.I. Troyan, Z. Phys C27 (1985) 65.

[48] T. Sjostrand and M. Bengtsson, Comp. Phys. Comm. 43, 367 (1987).

[49] MARK II, Phys. Rev. Lett. 62 (1990) 1334.

[50] DELPHI, Z. Phys. C50 (1991) 185.

[51] ALEPH, Phys. Lett. B273 (1991) 181.

[52] OPAL, Z. Phys. C53 (1992) 539.

[53] L3, Phys. Lett. B259 (1991) 199.

[54] H. Satz, in: Lecture Notes in Physics, vol. 56, p49, edited by J.G. Korner et al, Springer 1975.

[55] A.H. Muller, Phys. Lett. B104 (1981) 161; Nucl. Phys. B213 (1983) 85.

[56] A.H. Muller, Nucl. Phys. b213 (1985) 85; Yu.L. Dokshitzer and S.I. Troyan, LNPI-922, Leningrad, 1984.

[57] B.R. Webber, Phys. Lett. B143 (1984) 501.

[58] E.D. Malaza, B.R. Webber, Phys. Lett. B149 (1984) 501; Nucl. Phys. B267 (1986) 702.

[59] TASSO, Z. Phys. C45 (1989) 193.

[60] JADE, Z. Phys. C20 (1983) 187.

[61] For extensive review see, P. Carruthers, C.C Shih, Int. J. Mod. phys. A2 (1987) 1447.

[62] G.J. Alner, et al., Phys. Lett. B138 (1984) 304.

[63] S. Carius and G. Ingelman, Phys. Lett. B252 (1990) 647.

[64] A.Bassetto, M.Ciafaloni and G.Marchesini, Nucl. Phys. B163, 477 (1980).

[65] Yu.L.Dokshitzer, V.S.Fadin and V.A.Khoze, Z. Phys. C18, 37 (1983).

[66] Yu.L.Dokshitzer, V.A.Khoze, S.I.Troyan, in: *Perturbative* QCD, ed. A.H.Mueller, (World Scientific, Singapore) 1989.

[67] E.D.Malaza and B.R.Webber, Phys. Lett. B149, 501 (1984).

[68] Yu.L.Dokshitzer, Phys. Lett. B305, 295 (1993).

[69] M.Olsson and G.Gustafson, Nucl. Phys. B406, 293 (1993).

[70] I.M.Dremin, Phys. Lett. B313, 209 (1993).

[71] I.M.Dremin, Mod. Phys. Lett. A8, 2747 (1993).

[72] I.M. Dremin and R.C. Hwa, Phys. Rev. D49, 5805 (1994).

[73] I.M.Dremin and V.A.Nechitailo, JETP Lett. 58, 945 (1993).

[74] I.M.Dremin, B.B.Levtchenko and V.A.Nechitailo, Sov. J. Nucl. Phys. 57, 1091 (1994).

[75] T. Sjöstrand and M. Bengtsson, Comp. Phys. Comm. 43, 367 (1987).

[76] G. Marchesini *et al.*, Comp. Phys. Comm. 67, 465 (1992).

[77] G.Gianini *et al*, Phys. Lett. B336, 119 (1994).

[78] SLD Collab., K.Abe, et al., Phys. Rev. Lett. 72, 3145 (1994).

[79] R.Ugoccioni, A.Giovannini, S.Lupia. Phys. Lett. B342, 387 (1995).

[80] UA5 collaboration, Phys. Lett. 138B (1984) 304;

[81] JACEE collaboration, Phys. Rev. Lett. 50 (1983) 2062;

[82] NA22 collaboration, Phys. Lett. B222 (1989) 306;

[83] UA1 collaboration, CERN preprint CERN-EP/90-56.

[84] H. Navelet and R. Peschanski, Saclay preprint SPhT/85/102.

[85] A.Bialas and R. Peschanski, Nucl. Phys. B 273 (1986) 703.

[86] A.Bialas and R. Peschanski, Nucl. Phys. B 308 (1988) 857.

[87] R.C.Hwa, G. Pancheri and Y. Sriivastava, ed., Proc Conf. on Multiparticle Production, (World Scientific).

[88] F.Cooper, R.C. Hwa and I.Sarcevic, ed., Santa Fe Workshop on Intermittency in High Energy Collisions, Los Alamos, U.S.A, March 1990 (World Scientific).

[89] R.C.Hwa, W.Ochs and N. Schmitz, ed., Proc. Ringberg Workshop on Multiparticle Production Fluctuations and Fractal Structure, Rindberg, Germany, June 1991 (World Scientific).

[90] NA22 collaboration, Phys. Lett. B235 (1990) 373; Phys. Lett. B261 (1991) 165.

[91] UA1 collaboration, Nucl. Phys. B345 (1990) 1;

[92] F. W. Bopp, A. Capella, J. Ranft and J. Tran Thanh Van, Z. Physik C-Particles and Fields 51 (1991) 99.

[93] I.Derado et al (EMC), Z. Physik C-Particles and Fields 54 (1992) 357.

[94] L. Verluyten et al. (WA59 and E180), Phys. Lett. B260 (1991) 456.

[95] R. Holynski et al. (KLM), Phys. Rev. Lett. 62 (1989) 733 and Phys. Rev. C40 (1989) R2449.

[96] DELPHI collaboration, Phys. Lett. B247 (1990) 137; Nucl. Phys. B386 (1992) 471.

[97] OPAL collaboration, Phys. Lett. B262 (1991) 351.

[98] ALEPH collaboration, Z. Physik C-Particles and Fields 53 (1992) 21.

[99] L3 collaboration, Z.Physik C-Particles and Fields 55 (1992) 39.

[100] CELLO collaboration, Phys. Lett. B256 (1991) 97.

[101] E.A.De Wolf, I.M. Dremin and W. Kittel, HEN-362 (1993), Phys. Reports (1994).

[102] G. Gustafson and C. Sjogren, Phys. Lett. B248 (1990) 430.

[103] G. Ekspong, Proc. Santa Fe Workshop on Intermittency in High Energy Collisions (World Scientific).

[104] Yu. L. Dokshitzer, et al, Nuc. Phys B402 (1993) 139.

[105] S.Cantani et al., Phys. Lett. B269 (1991) 432; N. Brown and W.J.Stirling, Z.Phys. C53 (1992)629; S. Bethke, Z.Kunszt, D. Soper and W.J. Stirling, Nucl. Phys. B370 (1992) 320.

[106] J.D. Bjorken, S.J. Brodsky, Phys. Rev. D1 (1970) 1416.